ANALYSIS OF FATIGUE SURFACE CRACK USING THE PROBABILISTIC S-VERSION FINITE ELEMENT MODEL

MOHD AKRAMIN BIN MOHD ROMLAY

THESIS SUBMITTED IN FULFILMENT FOR THE DEGREE OF DOCTOR OF PHILOSOPHY

FACULTY OF ENGINEERING AND BUILT ENVIRONMENT
UNIVERSITI KEBANGSAAN MALAYSIA
BANGI

2016

ANALISIS RETAK PERMUKAAN LESU MENGGUNAKAN MODEL KEBARANGKALIAN UNSUR TERHINGGA VERSI-S

MOHD AKRAMIN BIN MOHD ROMLAY

TESIS YANG DIKEMUKAKAN UNTUK MEMPEROLEHI IJAZAH
DOKTOR FALSAFAH

FAKULTI KEJURUTERAAN DAN ALAM BINA
UNIVERSITI KEBANGSAAN MALAYSIA
BANGI

2016

DECLARATION

I hereby declare that the work in this thesis is my own except for quotations and summaries, which have been duly acknowledged.

29 June 2016

MOHD AKRAMIN BIN MOHD ROMLAY
P 60193

ACKNOWLEDGEMENTS

Alhamdulillah, first and foremost, I thanks Allah S.W.T. for endowing me with 'taufiq', patience and knowledge to complete this research work.

My deep gratitude and appreciation goes to my supervisors, Prof. Ir. Dr. Ahmad Kamal Ariffin Mohd Ihsan and Prof. Dr. Masanori Kikuchi for their extensive guidance, support and enthusiasm in all phases of this work.

I would like to thank Prof. Ir. Dr. Shahrum Abdullah and Prof. Ing. Dr. Nik Abdullah Nik Mohamed who advised me on the fatigue and mathematical model aspects.

My appreciation also dedicated to Prof. Dr. Michael Beer who permitted me to attach with his research laboratory at University of Liverpool. As well as for Dr. Edoardo Patelli, his guidance regarding COSSAN-X and reliability analysis is highly appreciated.

I also take this opportunity to express a deep sense of gratitude to the researchers of Kikulab, Tokyo University of Science (TUS); Institute of Risk and Uncertainty, University of Liverpool; and Computational and Experimental Mechanics Research Group (CEM), Universiti Kebangsaan Malaysia (UKM). Not forget to the technical staff of Universiti Kebangsaan Malaysia who supported this work in the aspect of experimental work.

Lastly, I thank my parents, wife, brothers, sisters and friends for their constant encouragement and support in completing this research work through various stages.

ABSTRACT

Fatigue failure is expected to contribute to injuries and financial losses in industries. The complex interaction between the load, time and environment is a major factor that leads to failure. In addition, the material selection, geometry, processing and residual stresses produce uncertainties and possible failure modes in the field of engineering. The conventional approach is to allow the safety factor approach to deal with the variations and circumstances as they occur within the engineering applications. The problems may persist in the computational analysis, where a complex model, such as a three-dimensional surface crack, may require many degrees of freedom during the analysis. The involvement of uncertainties in variables brings the analysis to a higher level of complexity due to the integration of non-linear functions during a probabilistic analysis. Probabilistic methods are applicable in industries such as the maintenance of aircraft structures, airframes, biomechanical systems, nuclear systems, pipelines and automotive systems. Therefore, a plausible analysis that caters for uncertainties and fatigue conditions is demanded. The main objective of this research work was to develop a model for uncertainties in fatigue analysis. The aim was to identify a probabilistic distribution of crack growth and stress intensity factors for surface crack problems. A sensitivity analysis of all the parameters was carried out to identify the most significant parameters affecting the results. The simulation time and the number of generated samples were presented as a measurement of the sampling efficiency and sampling convergence. A finite thickness plate with surface cracks subjected to random constant amplitude loads was considered for the fracture analysis using a newly developed Probabilistic S-version Finite Element Model (ProbS-FEM). The ProbS-FEM was an expansion of the standard finite element model (FEM). The FEM was updated with a refined mesh (*h*-version) and an increased polynomial order (*p*-version), and the combination of the *h*-*p* version was known as the S-version finite element model. A probabilistic analysis was then embedded in the S-version finite element model, and it was then called the ProbS-FEM. The ProbS-FEM was used to construct a local model at the vicinity of the crack area. The local model was constructed with a denser mesh to focus the calculation of the stress intensity factor (SIF) at the crack front. The SIF was calculated based on the virtual crack closure method. The possibility of the crack growing was based on the comparison between the calculated SIF and the threshold SIF. The fatigue crack growth was calculated based on Paris' law and Richard's criterion. In order to obtain an effective sampling strategy, the Monte Carlo and Latin hypercube sampling were employed in the ProbS-FEM. The specimens with a notch were prepared and subjected to fatigue loading for verification of the ProbS-FEM results. The ProbS-FEM was verified for the SIF calculation, the crack growth for mode I and the mixed mode, and the prediction of fatigue life. The major contribution of this research is to the development of a probabilistic analysis for the S-version finite element model. The formulation of uncertainties in the analysis was presented with the ability to model the distribution of the surface crack growth. The ProbS-FEM was shown to resolve the problem of uncertainties in fatigue analysis. The ProbS-FEM can be further extended for a mixed mode fracture subjected to variable amplitude loadings in an uncertain environment.

ANALISIS RETAK PERMUKAAN LESU MENGGUNAKAN MODEL KEBARANGKALIAN UNSUR TERHINGGA VERSI-S

ABSTRAK

Kegagalan lesu telah menyumbang kepada kecederaan dan kerugian dalam industri. Interaksi kompleks antara beban, masa dan persekitaran adalah faktor utama yang membawa kepada kegagalan. Di samping itu, pemilihan bahan, geometri, pemprosesan dan tegasan baki menghasilkan ketidakpastian dan mod kegagalan yang mungkin berlaku dalam bidang kejuruteraan. Pendekatan konvensional menggunakan kaedah faktor keselamatan bagi menangani perubahan dan sebarang kemungkinan yang berlaku semasa applikasi kejuruteraan. Masalah berterusan dalam analisis pengiraan, di mana model yang kompleks seperti permukaan retak tiga-dimensi memerlukan darjah kebebasan yang banyak. Penglibatan unsur ketidakpastian dalam pembolehubah membawa analisis ke tahap yang lebih rumit. Ia disebabkan oleh integrasi fungsi bukan linear semasa analisis kebarangkalian. Kaedah kebarangkalian boleh digunakan didalam industri penyelenggaraan struktur pesawat, sistem biomekanik, sistem senjata nuklear, saluran paip dan automotif. Oleh itu, analisis yang munasabah dengan mengambil kira keadaan ketidaktentuan dan kelesuan diperlukan. Objektif utama penyelidikan ini adalah untuk membangunkan satu model ketidaktentuan bagi analisis kelesuan. Tujuannya ialah untuk mengenal pasti taburan kebarangkalian pertumbuhan retak dan faktor keamatan tegasan. Analisis sensitiviti bagi semua pembolehubah dilakukan bagi mengenal pasti pembolehubah yang paling berpengaruh terhadap kegagalan. Masa simulasi dan jumlah sampel yang dihasilkan dibentangkan sebagai pengukuran kepada kecekapan dan penumpuan persampelan. Satu plat dengan ketebalan terbatas yang mempunyai retak permukaan dan bebanan rawak yang berterusan di analisis menggunakan kaedah kebarangkalian Model Unsur Terhingga Versi-S (ProbS-FEM). ProbS-FEM dikembangkan daripada model unsur terhingga (FEM) yang biasa. FEM telah dikemas kini dengan jaringan halus (versi-*h*) dan peningkatan kuasa polinomial (versi-*p*) dan hasil gabungan versi *h*-*p* dipanggil sebagai model unsur terhingga versi-S. Kemudian, analisis kebarangkalian disertakan di dalam model unsur terhingga versi-S dan diberi nama ProbS-FEM. ProbS-FEM menggunakan kaedah pembinaan model tempatan di sekitar kawasan retak. Model tempatan dibina dengan jejaring yang lebih padat untuk memberi tumpuan terhadap pengiraan faktor keamatan tekanan (SIF) pada bahagian retak hadapan. SIF dikira berdasarkan kaedah penutupan retak maya. Kebarangkalian retak untuk berkembang adalah berdasarkan kepada perbandingan di antara nilai SIF yang dikira dan nilai SIF ambang. Pertumbuhan retak lesu dikira berdasarkan model Paris dan kriteria Richard. Persampelan Monte Carlo dan Latin hiperkiub digunakan di dalam ProbS-FEM untuk mendapatkan srategi persampelan yang berkesan. Spesimen-spesimen dengan takuk disediakan dan diuji dengan bebanan lesu untuk tujuan pengesahan. Probs-FEM disahkan dengan pengiraan SIF; pertumbuhan retak untuk mod I dan mod campuran; dan ramalan hayat lesu. Sumbangan utama kajian ini ialah pembangunan analisis kebarangkalian untuk model unsur terhingga versi-S. Formula ketidaktentuan didalam analisis telah dibentangkan dengan keupayaan untuk memodelkan taburan pertumbuhan permukaan-retak. ProbS-FEM telah menunjukkan keupayaan untuk menyelesaikan masalah ketidaktentuan dalam analisis kelesuan. Ia boleh dikembangkan lagi untuk kes mod patah campuran dengan beban amplitud berubah-ubah dalam persekitaran yang tidak menentu.

CONTENTS

LIST OF TABLES

LIST OF FIGURES

LIST OF SYMBOLS

a	Crack depth
a_i	Initial crack depth
b, b_G^e, b_L^e	Body force, for global, local element
B, B^G, B^L	Deformation matrix, for global, local
c	Crack length
c_i	Initial crack length
C	Paris coefficient
da	Crack growth increment
$da_{a/c}$	Crack length or depth increment
da_{max}	Maximum crack growth increment
dN_l	Fatigue life cycle range
D	Material properties matrix
D_n	Maximum difference of two cumulative distribution functions
D_n^α	Standard difference values at various significance level α
E	Young's modulus
$E[\cdot]$	Mean operator
f	Nodal force
f_i	Joint reaction at node
F, F_G^e, F_L^e	Load vector at global, local element
F_X	Cumulative distribution function
$F_X(x_i)$	Theoretical cumulative distribution function
$g(X)$	Performance function

G, G_I, G_{II}, G_{III}	Energy release rate, for failure mode I, II, III
h	Width of specimen
i	Node number
k	Stiffness matrix
K	Stress intensity factor
K_{Ic}	Fracture toughness
K_{eq}	Equivalent stress intensity factor
$K_{GG,GL,LG,LL}$	Stiffness matrix at global, global-local, local-global, local
$\triangle K_{th}$	Threshold value
max	Maximum
n	Paris coefficient
N	Shape function
N_l	Fatigue life cycle
N_t	Total number of sample
N_f	Total number of failure sample
p	Portion number
P_f	Probability of failure
PR	Poisson ratio
r	Width of element parallel to the crack front
$\bar{r}$	Distance from the crack front
r_P	Pearson product moment correlation coefficient
R	Crack front radius
R^2	Coefficient of determination

S_1, S_2	Area before, after crack front
$S_n(x_i)$	Empirical cumulative distribution function
t	Vector of boundary tractions
Q	Shape factor
q_i	Random number
u, u^G, u^L, u^e	Displacement, for global, local, node
u_{iU}, u_{iL}	Displacement for upper, lower surface crack
$Var(\cdot)$	Variance operator
x_i	Random parameter
x, y, z	Physical nodal coordinate
$\overline{x}, \overline{y}, \overline{z}$	Estimation coordinate
X_i^G, Y_i^G, Z_i^G	Nodal coordinate for global mesh
X_i^L, Y_i^L, Z_i^L	Nodal coordinate for local mesh
ξ, η, ζ	Gaussian coordinate
ξ^G, η^G, ζ^G	Gaussian coordinate for global element
ξ^L, η^L, ζ^L	Gaussian coordinate for local element
$\overline{\xi}^G, \overline{\eta}^G, \overline{\zeta}^G$	Vector for trial value coordinate
$\overline{\xi}^G_{next}, \overline{\eta}^G_{next}, \overline{\zeta}^G_{next}$	Vector for next trial value coordinate
σ	Stress
σ_{33}	Cohesive stress
σ_X	Standard deviation
$\sigma_{\bar{X}}$	Sample standard deviation
$\varepsilon, \varepsilon^G, \varepsilon^L$	Strain, for global, local
$\Omega, \Omega^G, \Omega^L$	Domain, for global, local

$\Gamma, \Gamma^t, \Gamma^u, \Gamma^{GL}$	Boundary, of displacement, force, global region, overlay region
α	Significance level
τ	Shear stress
γ	Shear strain
ν	Poisson's ratio
ν_i	Crack opening displacement function
$\bigwedge$	Length of element perpendicular to the crack front
ϕ	Angle between the direction of r and normal direction of the crack front
θ	Angle
φ_o	Crack growth angle
μ	Shear modulus
μ_X	Mean
$\bar{\mu_X}$	Sample mean
Φ^{-1}	Inverse of cumulative distribution function

LIST OF ABBREVIATIONS

ASTM	American Society for Testing and Materials
CDF	Cumulative Distribution Function
Det. S-FEM	Deterministic S-version Finite Element Model
ECDF	Empirical Cumulative Distribution Function
EPFM	Elastic Plastic Fracture Mechanics
FEA	Finite Element Analysis
FEM	Finite Element Model
LEFM	Linear Elastic Fracture Mechanics
LHS	Latin Hypercube Sampling
MC	Monte Carlo
MCS	Monte Carlo Simulation
PDF	Probability Density Function
ProbS-FEM	Probabilistic S-version Finite Element Model
POF	Probability of Failure
SIF	Stress Intensity Factor
STD	Standard Deviation
S-FEM	S-version Finite Element Model
VCCM	Virtual Crack Closure Method

CHAPTER I

INTRODUCTION

1.1 CHAPTER OUTLINE

This chapter introduces the role of surface cracks in promoting fractures and failures in mechanical structures. The motivation of the study is firstly highlighted based on industrial failures. Then, the problem statement with regard to surface cracks is presented. The research objectives and research scope of the present study are provided, and this is followed by an outline of the thesis in the last section of this chapter.

1.2 INTRODUCTION TO PROBABILISTIC APPROACH IN CRACK ANALYSIS

Fracture failure often occurs from initial flaws or defects developed near a stress riser. The stress riser causes the development of surface or sub-surface flaws. This, combined with repeated loading, will result in the presence of surface cracks. The presence of surface cracks is unavoidable in real structures. For example, surface cracks exist in many forms in structural components such as at corners, bends, holes, grooves and notches. Under in-service and loading conditions, the surface cracks tend to grow at micro and macro scales before the cracks propagate until the structure completely fails. Therefore, a proper safety assessment is needed to produce an accurate evaluation of the effects produced by surface cracks (Brighenti & Carpinteri, 2013).

The size, shape, location and orientation of surface cracks in structural components are scattered (Brighenti & Carpinteri, 2013). Variations in those

parameters influence the stress intensity factor (SIF) of the surface cracks and the fatigue behaviour of the structural components. The variations in the parameters are not limited to the size, shape, location and orientation of the surface cracks alone, but are also contributed to by the material properties. The material properties, particularly the fatigue parameters, play a major role in contributing to variations in the SIF and fatigue behaviour. Thus, the randomness in some of the parameters exposes the analysis of the surface cracks to a certain degree of complexity. The prediction of brittle fractures for surface cracks is a unique challenge to researchers. The shape and boundary conditions of the structural components, the size, shape, location and orientation of the surface cracks, and the fatigue loading are taken into account in the analysis.

As the SIFs for surface cracks must be computed along the whole crack front, the three-dimensional fatigue propagation analysis of surface cracks is gaining attention from researchers. The assessment of a three-dimensional surface crack is performed during the whole process of fatigue crack growth. The crack growth relationships are applied to study the evolution of crack shapes in industrial failures. Examples of cases of industrial failures are considered to refine the study motivations.

A few typical structural components with the existence of surface cracks, such as cracked plates (Dong et al., 2015; Peng et al., 2015), cracked round bars (Carpinteri & Vantadori, 2009, 2009; Toribio et al., 2014, 2015), cracked pipes (Brighenti, 2001), cracked shells (Carpinteri et al., 2009; Liu et al., 2006) and cracks in notched structural components (Cendõn et al., 2015; Larrosa et al., 2015), lead to failure in industries such as in petrochemical, aircraft, aerospace, marine and other industries. Figure 1.1 shows a typical crack that occurred in a helicopter Longeron driven by fatigue loading (Newman et al., 2010). Initially, the fatigue crack was propagated due to the loading of the opening mode, but as the crack approached a certain length, a mixed mode loading occurred. Therefore, a safe and reliable maintenance operation was required.

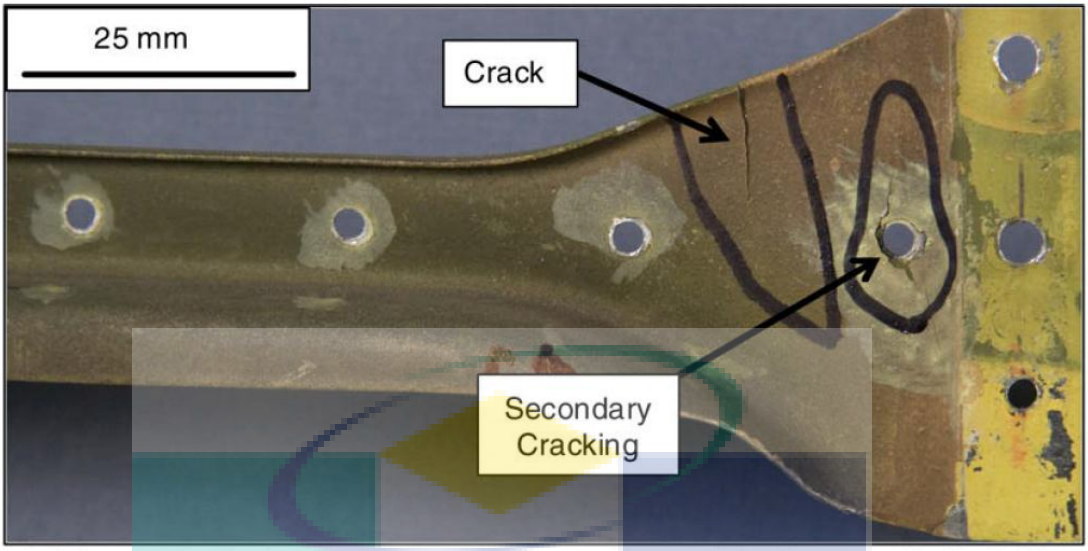

Figure 1.1 Typical helicopter Longeron crack

Source: Newman et al., 2010

The fracture of an aging aircraft wing skin due to fatigue is shown in Figure 1.2 (Emery et al., 2009). The need for a more reliable structure due to variations in the flaws and fatigue material properties is receiving increasing attention. The random nature of the material system results in undesirable and undervalued flaws and material properties. This random nature leads to uncertainties in the analysis. Therefore, current life estimation methods need to be improved to a better level, where the uncertainties element is taken into account. Figure 1.3 is a schematic diagram of oil storage tanks and the formation of cracks in a reactor shell. Cyclic stress occurred due to the frequent loading and unloading of the liquid and the uneven settling of the foundation under the tank (Kim et al., 2009). Thus, the fatigue evaluation of surface cracks in structural components using fracture mechanics is essential. Uncertainties in the crack size, shape, location and in the parameters of the crack growth model need to be considered.

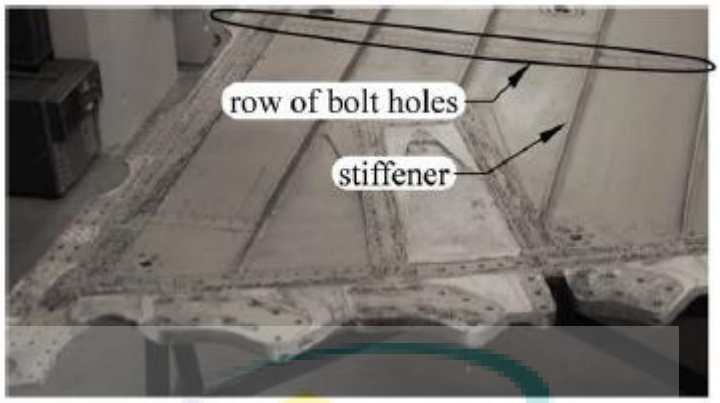

(a)

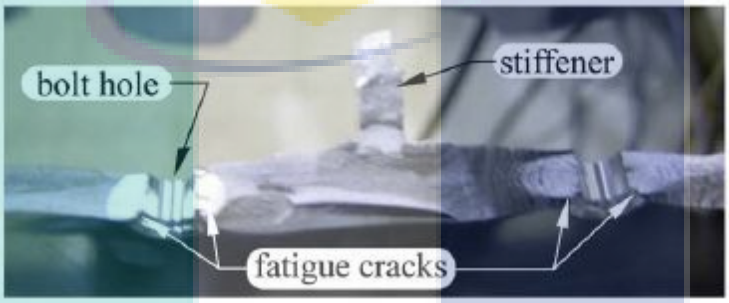

(b)

Figure 1.2 (a) A wing panel with a row of boltholes; (b) Fractured aircraft wing skin

Source: Emery et al., 2009

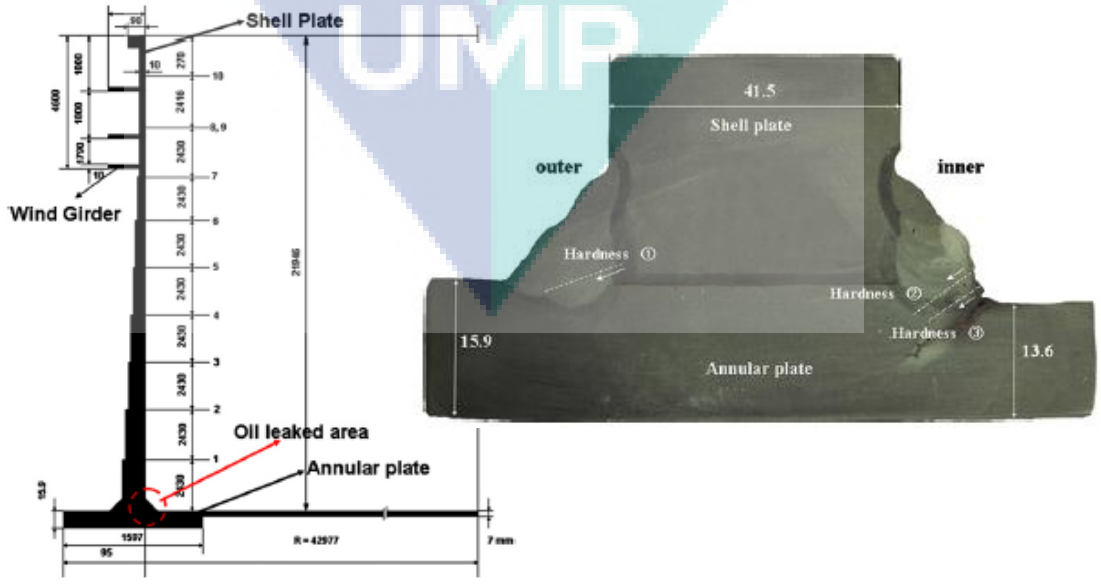

Figure 1.3 Schematic diagram of oil storage tank and crack formation

Source: Kim et al., 2009

Therefore, an analysis method that considers the uncertainties in the structural component in the application environment is needed. One such method is the probabilistic analysis method. The probabilistic approach enables uncertainties to be quantified in a distribution. The distribution describes the range of possible values of random parameters such as the crack size, location or fatigue crack growth model parameters. The results of the probabilistic assessment can be shown in the form of a distribution to indicate the impacts that can possibly occur. Thus, a probabilistic assessment can be a basis for decision making in maintenance priority and risk determination.

Figure 1.4 shows a comparison of the basic concepts of the probabilistic and deterministic approaches. The deterministic concept produces a single outcome from an input. The input is produced from a sample space of inputs. Unlike the deterministic approach, the probabilistic concept produces from a single up to *n* inputs. The outcomes are established from each input. At the end of the process, a distribution of outcomes is produced. Therefore, the probabilistic concept is capable of dealing with the presence of uncertainties by generating all the possible inputs.

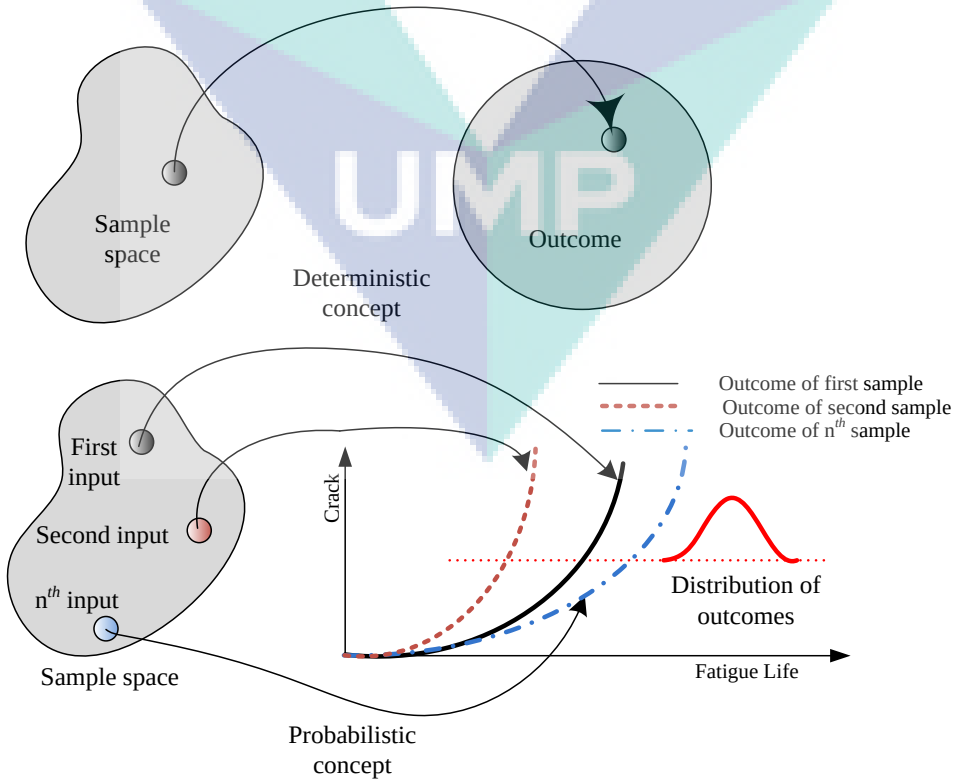

Figure 1.4 Basic concept of probabilistic approach

1.3 STUDY MOTIVATIONS

The need for accurate approaches to assess uncertainties in computer models, geometries, loads, material properties, manufacturing processes and environments is significantly increased due to the requirements of critical and complex designs. When the level of randomness is relatively small, a deterministic model is sufficient. However, when the level of uncertainties is high, a probabilistic approach is essential for the analysis and design.

Figure 1.5 shows the comparison between the deterministic and probabilistic approaches. The deterministic approach starts with a single parameter, while the probabilistic approach starts with random parameters. The random parameters produce a statistical response that is important for predicting the cause of failure. Then, a comprehensive description of the results can be produced via a robust system. The deterministic approach creates a deterministic response and produces a static description. The deterministic approach may lead to under or over-designing that could disrupt the safety of a system (Choi et al., 2007).

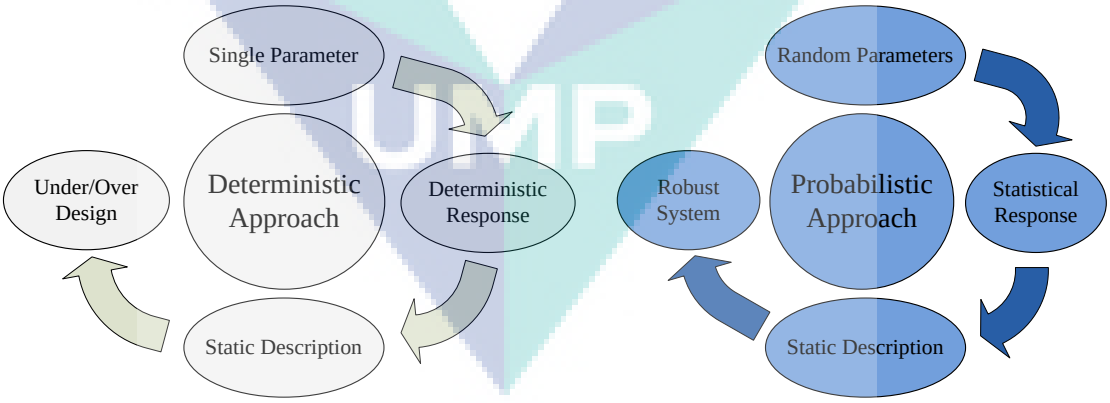

Figure 1.5 Comparison between deterministic and probabilistic approaches

Source: Choi et al., 2007

The safety of structural components is a major issue. The deterministic approach implements a safety factor to handle any uncertainties or circumstances that may occur in the design. The safety factor approach may lead to the under or over-

designing of the structural components. Under-designing may result in failure, whilst over-designing may arbitrarily increase the cost. Thus, it is feasible to use a numerical simulation with the probabilistic approach.

The numerical simulation for fatigue surface crack growth is determined by the input parameters, fatigue crack growth model and crack growth direction model that are implemented in the simulation code. The calculations for the crack length and depth, fatigue cycles and SIF of the surface cracks depend on the material constants and constant parameters in the fatigue models. The material constants and constant parameters in the fatigue crack growth model are treated as deterministic values in the deterministic analysis. In reality, the material constants and constant parameters in the fatigue crack growth models vary. Setting up random parameters as deterministic values in an analysis may ruin the results.

A numerical approach offers more advantages compared to an analytical approach, where advances in computer technology allow predictions that are more accurate. Due to the presence of uncertainties, the numerical simulation of surface cracks is more complex, and fewer investigations focus on three-dimensional models due to the complexity of the computations that are required. In order to model the problem in a timely and cost-effective way, it is necessary to enhance finite element models. Therefore, this thesis attempted to employ computations using a finite element model to present a new combination of probabilistic analysis and an advanced finite element model for surface cracks that promote brittle fracture.

1.4 PROBLEM STATEMENT

The mechanical behaviour of surface cracks in promoting failures is crucial in all modes of failures. Failures can occur in real applications such as aircraft structures, stiffened panels, airframes, biomechanical systems, nuclear systems, pipelines and the automotive industry. For example, the structural life of an aircraft fleet is defined by the fatigue design criteria. The fatigue design criteria use the safety factor approach to assume the initial defects in the structure. The objective of the fatigue design criteria is to detect initial cracks before they reach a critical crack size after the usage of an

aircraft by imposing inspections. The inspection intervals are derived by using safety factors and crack size assumptions. The US Air Force provides guidelines on crack size assumptions to calculate crack growth so as to determine inspection intervals (Iyyer et al., 2007). The safety factor approach and crack size assumptions are exposed to uncertainties in analysis.

However, the existence of uncertainties in analysis has received relatively little attention compared to the deterministic approach (Quaranta, 2011; Reh et al., 2006). Advancements in the computational and experimental mechanics make it possible to explore the role of uncertainties in promoting failure and the mechanics of elastic surface cracks.

The mechanics of the behaviour of surface cracks for all damage processes become complex, especially when a three-dimensional surface crack analysis and uncertain parameters are involved. The reported probabilistic three-dimensional surface crack results from this technique are scarce. One of the difficulties in considering probabilistic surface cracks is the complex geometry that requires many degrees of freedom in numerical modelling and leads to a prohibitively long computation time. The complex geometry also influences the surface crack growth.

The determination of random surface crack growth in fatigue is also a challenge since the finite element model needs to predict the growth and direction in any of the possible paths. A significant number of uncertainties affect the phenomenon of surface crack growth. Thus, the possible surface crack growth that is affected by the randomness of material parameters, crack location, crack size and crack orientation needs to be predicted. The random parameters may increase the probability of failure.

The probability of failure is calculated based on the integration of the probability density function, which involves a non-linear function. Therefore, a method that is able to solve the integration numerically is indispensable. Thus, reliance on the safety factor approach can be avoided.

The safety factor in the deterministic approach is expected to handle any uncertainties involved in the design. However, the implementation of a safety factor may result in under or over-designing of a structure. It might cause an early failure or increase the cost. The deterministic approach needs to be replaced with a better method that is able to predict fracture and failure. The following sections outline the research objectives and research scope of this thesis, based on the research problems.

1.5 RESEARCH OBJECTIVES

The prime objective of this thesis was to develop, test and provide a computational fracture mechanics model that emphasizes the quantification of uncertainties for surface cracks. Thus, the objectives were divided as follows.

(i) To establish a mathematical model for the distribution of surface crack growth that considers variations in the initial surface crack size and material properties.

(ii) To create an effective algorithmic solution for the S-version Finite Element Model that takes into consideration the randomness of variables.

(iii) To develop a probabilistic S-version Finite Element Model (S-FEM) for surface cracks which are caused by uncertainties in the material and the geometry.

(iv) To validate and enhance the SIF, surface crack growth and fatigue life prediction on the developed finite element model for surface cracks.

1.6 RESEARCH SCOPE

The fracture and failure studies that were promoted by the Probabilistic S-version Finite Element Model (ProbS-FEM) focused on the probabilistic analysis of the problem of surface cracks. A few limitations were imposed on the study in order to present the specific scope of the investigation. The limitations were as follows:

(i) The current study was divided into numerical simulations and experimental work on the problem of surface cracks.

(ii) Finite element modelling was developed to simulate the metallic materials that predict failure by brittle fracture. The fracture mechanics parameters were based on a three-dimensional finite element analysis (FEA) and linear elastic fracture mechanics (LEFM). Thus, the current study was limited to investigating the problem of elastic surface cracks.

(iii) The uncertain parameters were limited to the material properties and the geometry, particularly with regard to the size, location and orientation of the surface cracks. The distribution of the uncertain parameters was gained from a literature review and experimental approach.

(iv) The estimation of failure method was based on the SIF value. The critical SIF is the limit between the safe and the failure region. Thus, the comparison between the calculated SIF and the critical SIF was used to determine the failure. Then, the SIF was used to calculate the fatigue crack growth. The calculation of the fatigue crack growth was limited to Paris' law.

(v) The probabilistic analysis was limited to the Monte Carlo simulation (MCS) technique. The enhancement of the effectiveness of the sampling process was based on the Latin Hypercube Sampling (LHS).

1.7 THESIS OUTLINE

This thesis is divided into five chapters. Chapter 1 presents the introduction, study motivations, problem statement, research objectives and research scope.

Chapter 2 starts with a brief introduction to brittle fracture and failure that are influenced by surface cracks. Then, the computational fracture mechanics is presented in the next section. The involvement of uncertainties in numerical methods is

discussed in a separate section. Chapter 2 ends with the findings from the literature review.

In Chapter 3, the finite element formulation of the S-FEM and ProbS-FEM are discussed. The explanation pertaining to the extraction of the probabilistic information is highlighted, as it is the focus of this research. The experimental setup for the purpose of verification is also presented in Chapter 3.

The results and discussion of the ProbS-FEM analysis are presented in Chapter 4. Chapter 5 lists the main achievements and conclusions of the current work and discusses recommendations for future works.

Lastly, a set of references and appendices, that include the finite element formulation and the developed codes, are attached with this thesis.

CHAPTER II

LITERATURE REVIEW

2.1 CHAPTER OUTLINE

This chapter presents a review of previous works on surface crack problems that cause brittle fracture and failure. In addition, a review of the mechanics of computational fracture and the quantification of uncertainties in FEM is presented in this chapter. The objective of this chapter was to identify the research gap from previous works on surface cracks in an attempt to solve the problem using the FEM and probabilistic concepts.

2.2 BRITTLE FRACTURE AND FAILURE DUE TO SURFACE CRACKS

This section addresses the role of surface cracks by an introduction to fracture mechanics, the brittle failure mechanism and the formulation of fracture parameters in LEFM. The occurrence of surface cracks that may lead to fracture and failure is common in structural components. A brief review of fracture mechanics, LEFM, fatigue design criteria, fatigue crack growth model and the direction of crack growth with respect to surface cracks are presented in turn.

2.2.1 Fracture Mechanics

Fracture mechanics is defined as the science that describes the behaviour of bodies containing cracks (Taylor 2007). The works of Griffith (1920), Westergaard (1939) and Irwin (1958) have greatly contributed to the development of the fracture mechanics theory. Details of the history and development of fracture mechanics is available in the studies by Anderson (2005) and Gdoutos (2005). Figure 2.1 shows the

percentage fraction of the research trends in various types of cracks problem. The problem of surface cracks has become the focus of researchers due to the frequent occurrence of failures in industries (Brighenti & Carpinteri, 2013) such as in pipelines (Śnieżek et al., 2016), marine (Pang et al., 2016, offshore (Pang et al., 2016), aeronautics (Shi et al., 2014) and aircraft (Newman Jr & Ramakrishnan, 2016) industries.

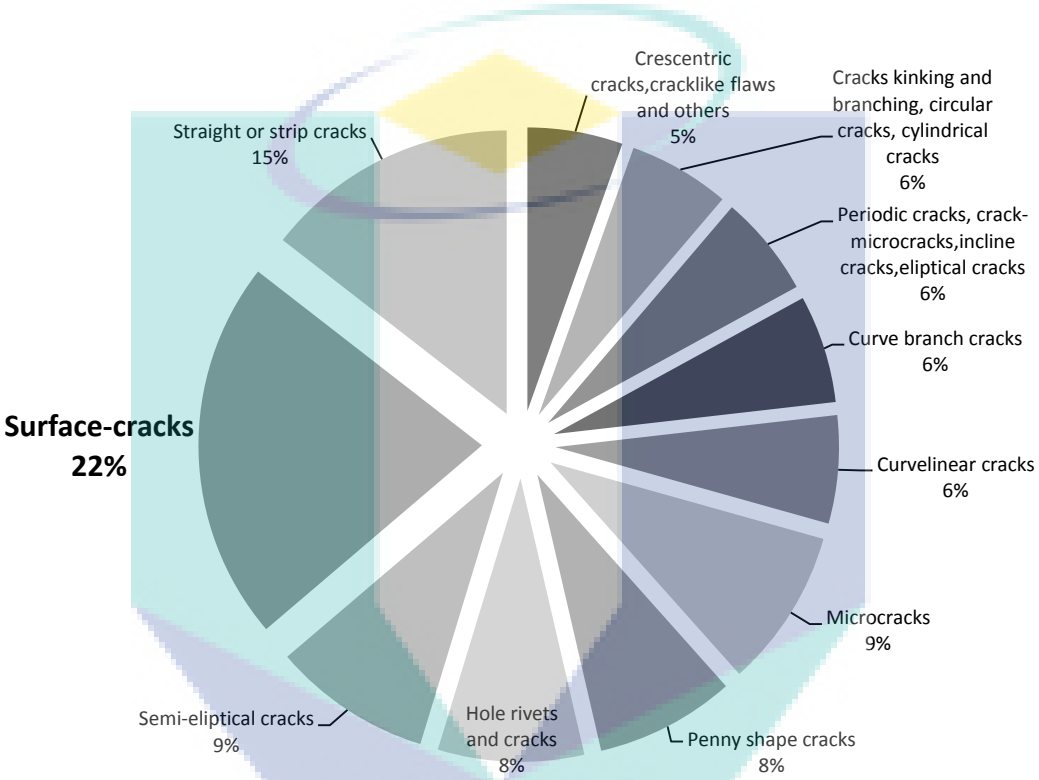

Figure 2.1 Fractions of surface crack studies

Source: Daud, 2012

Failure mechanisms promoted by cracks can be addressed by failures at atomic levels in different failure modes. The study of the fracture process depends on the scale level at which it is considered (Gdoutos, 2005). Figure 2.2 shows the significance of the size range in the crack propagation process. The fracture phenomenon is usually studied within the atomic (10^{-10} m), microscopic (10^{-6} m) or continuum (10^{-6} – 10^{2} m) scale levels. The continuum scale level is less expensive computationally than atomic modelling and hybrid atomic-continuum mechanics modelling. The possibility of simulating large-scale structures and reducing the degree of freedom in problems are other advantages of using the continuum scale level. Since

the aim of this study was to solve large-scale structural problems, the continuum scale level was adequate.

Continuum mechanics deals with the analysis of materials under external loadings that can be viewed as continuous or homogenous media. The concept of a continuum mechanics model has produced the theories of LEFM and Elastic Plastic Fracture Mechanics (EPFM) (Anderson, 2005; Gdoutos, 2005).

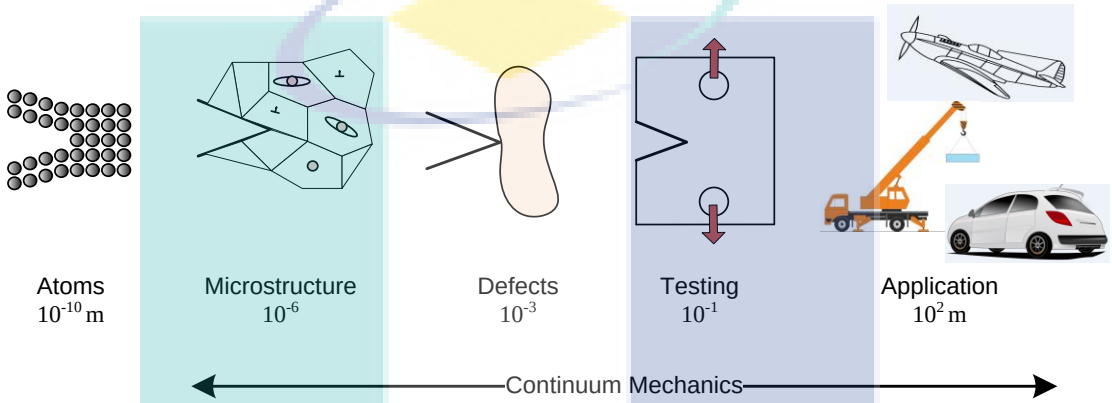

Figure 2.2 Fracture mechanisms at different scales

2.2.2 Linear Elastic Fracture Mechanics

Whether a fracture occurs in a ductile or brittle manner, or a fatigue crack grows under cyclic loading, the local plasticity at the crack tip controls both the fracture and the crack growth (Stephens et al., 2001). The plastic zone size at the crack tip is calculated by using the stress field equations with the SIF and yield strength as functions of the determination. The SIF is a fundamental parameter of the LEFM. Several researchers, such as Irwin (1957), Dugdale (1960), Paul & Tarafder (2013) and Paul (2016) have attempted to determine the size of the plastic zone. The LEFM is applicable when the plastic zone radius at the crack tip is relatively small compared to the dimensions of the specimen (Stephens et al., 2001). In addition, the LEFM is capable of determining the crack growth in materials under the basic assumption that the material conditions are mainly linear elastic during the fatigue process.

Figure 2.3 shows three types of crack deformations or modes that could be extended by surface cracks. Mode *I* is the opening mode and most cracks tend to propagate in this mode, particularly in the fatigue mode. This is because cracks tend to grow on the plane of maximum tensile stress. Fatigue loading produces different plastic zone sizes. The plastic zone size for fatigue is one-fourth that of the monotonic plastic zone size (Dowling, 1999) as the local stress near the crack tip is reduced to a value that is less than that observed for the monotonic plastic zone size. The unloading process produces a smaller sized plastic zone. The LEFM can often be applied to the fatigue crack growth process, even for materials that exhibit significant plasticity (Berer & Pinter, 2013; Dowling, 1999; Leander et al., 2013; Rhymer et al., 2008; Stephens et al., 2001). The introduction to the LEFM will lead to the computation of the SIF, which is the first step in the analysis of cracked bodies (Nejati et al., 2015). Then, by design, the cracked bodies are prevented from an early retirement through fatigue design criteria.

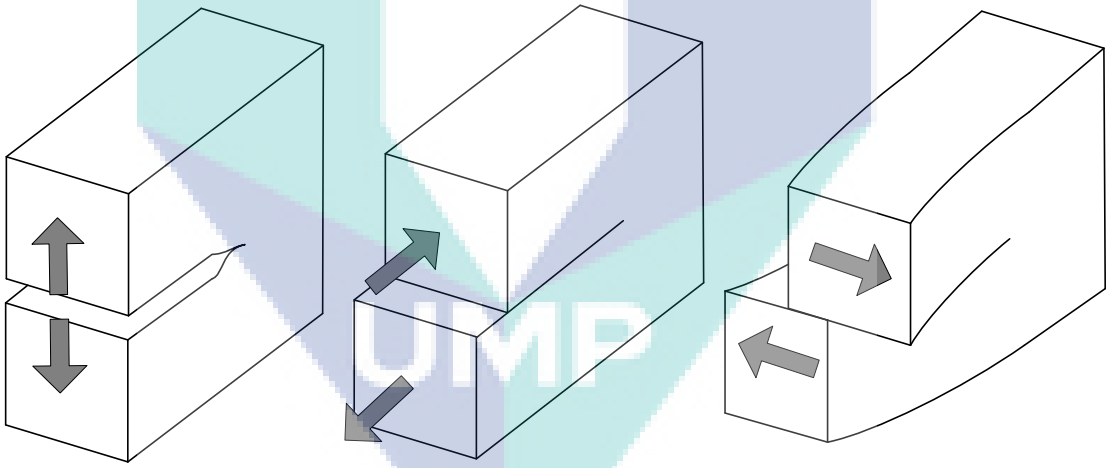

Figure 2.3 Failure modes *I*, *II* and *III*

2.2.3 Fatigue Design Criteria

The fatigue design criteria are essential for the determination of the structural life. The objectives of the fatigue design criteria are to ensure the safety and maximize the usage of a structure. There are three methods for the fatigue design criteria: the safe-life, fail-safe and damage-tolerant approaches (Iyyer et al., 2007).

The safe-life method is defined by the crack initiation time, which is calculated based on static and fatigue material properties. However, the structure is retired before the formation of fatigue cracks by the use of the safety factor approach (Feng et al., 2014; Iyyer et al., 2007). The advantages of the safe-life method are the enhanced safety and decreased inspection costs (Forth et al., 2002). A few disadvantages of the safe-life approach might occur, such as premature retirement, when high safety factors are used. In addition, defects from the manufacturing process are not considered by the safety factors.

The fail-safe method considers the defects from the manufacturing process and during the service life. The structure is designed to allow multiple load paths so that after the failure, structural integrity is not impaired significantly (Iyyer et al., 2007). Thus, ample time is allocated for scheduled inspections and repairs. A maintenance program for inspection is part of the fail-safe method. The inspection intervals are decided based on the time interval for crack growth. The inspection intervals are calculated after a crack is detected on the structure. The inspections should be scheduled before the critical crack sizes are reached (Zhang et al., 2009). Thus, the calculation of the inspection intervals is made by using the appropriate safety factors.

The damage-tolerant method carries out inspections to detect cracks before they reach a critical size. Safety factors on the crack growth life are determined to establish the inspection intervals. The inspections are conducted before the detectable cracks propagate to critical crack sizes. The US Air Force provides guidelines on crack size assumptions for the calculation of crack growth life (Iyyer et al., 2007). The structure is designed to have a higher residual strength than the operational limit loads when a crack occurs (Iyyer et al., 2007; Ming-Zhou et al., 2016).

The three methods of fatigue design criteria are to monitor the fatigue life of a cracked structure. The structure is designed to consider the existence of cracks before and during the service life. Any one of the above methods relies on the safety factor approach for the calculation of fatigue crack growth due to the uncertain length of the initial crack, which is crucial for the fatigue crack growth model.

2.2.4 Fatigue Crack Growth Model

Figure 2.4 shows a typical fatigue rate curve. Commonly, the curve is separated into three major regions, namely region I, II and III. Region I indicates a threshold value, $\triangle K_{th}$, below which the fatigue cracks are considered as non-propagating. This region is influenced by the microstructure, mean stress, frequency and environment (Beden et al., 2009; Stephens et al., 2001). Region II shows a linear relationship between log da/dN and log $\wedge K$. The formula

$$da/dN = C(\triangle K)^n \tag{2.1}$$

was first introduced by Paul Paris in the early 1960s. Region II, or the Paris region, is typically controlled by the environment. The microstructure has less influence on the behaviour of fatigue crack growth in region II (Stephens et al., 2001). The use of LEFM concepts is acceptable and the data follow a linear relationship between log da/dN and log $\wedge K$ (Beden et al., 2009). In region III, the fatigue crack growth rates are very high and are controlled by the fracture toughness, K_{IC}.

Paris' law offers a basic description of fatigue crack growth. This law was used in this research work due to its simplicity and the involvement of fewer parameters. In addition, the limitation with regard to the number of parameters provides the advantage of focusing on other uncertain parameters, such as the geometry and crack size. From the Paris model, the fatigue crack growth model was extended to more specific phenomenological factors such as in the Wheeler (Khan et al., 2010; Mehrzadi & Taheri, 2013), Willenborg (Wang et al., 2016), Elber (Johan Singh et al., 2007), Gallagher and Hughes (Barker et al., 2013), Barsom (Iranpour et al., 2008) and McEvily (Wang et al., 2008) models. Each model can only account for one or several phenomenological factors. Although many models have been developed, none of them enjoys universal acceptance (Beden, 2010). Thus, only the Paris model was developed in this research for the sake of universal acceptance. Then, the direction of the crack growth was modelled after the calculation of the fatigue crack growth.

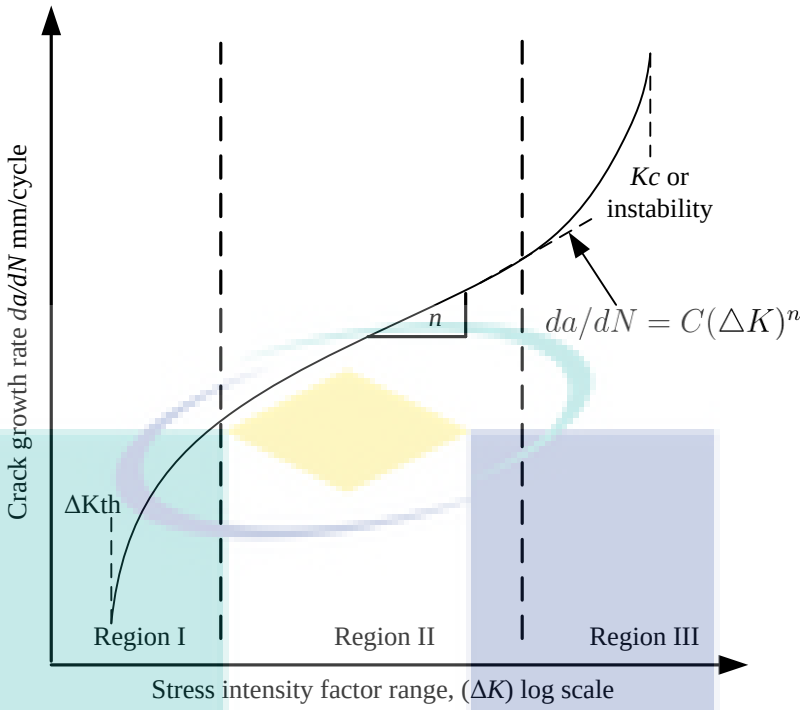

Figure 2.4 Typical fatigue crack growth rate curve

2.2.5 Crack Growth Direction

The prediction of a three-dimensional crack growth direction in a linear-elastic region is based on the stress intensity factors, K_I, K_{II}, and K_{III}. Only a few fracture criteria exist for three-dimensional mixed mode problems. The well-known Sih criterion is based on the strain energy density (Sih, 1990). The crack growth angle, φ_o is derived by minimizing the strain energy density factor. The formulation of φ_o is dependent on mode *I* and mode *II* of the SIF and Poisson's ratio. A further explanation can be found in Sih (1990).

The Pook criterion for a three-dimensional crack growth was developed based on K_I and K_{II}.

$$K_I \sin\varphi_o = K_{II}(3\cos\varphi_o - 1) \tag{2.2}$$

The Pook criterion is further discussed in Pook (1982, 2000). The criterion of Schollmann et al. is based on the assumption that crack growth develops

perpendicularly to the direction of the special maximum principal stress, σ_1'. The σ_1' is defined as follows

$$\sigma_1' = \frac{\sigma_\varphi + \sigma_z}{2} + \frac{1}{2}\sqrt{(\sigma_\varphi - \sigma_z)^2 + 4_{\varphi z}^2} \tag{2.3}$$

Since the Schollmann et al. criterion assumes that the crack growth direction is perpendicular to σ_1', the partial differential with respect to φ_o is as follows

$$\begin{aligned} &-6K_I \tan\left(\frac{\varphi_o}{2}\right) - K_{II}\left(6 - 12\tan^2\left(\frac{\varphi_o}{2}\right)\right) \\ &+\left\{\left[4K_I - 12K_{II}\tan\left(\frac{\varphi_o}{2}\right)\right]\right. \\ &\times\left[-6K_I \tan\left(\frac{\varphi_o}{2}\right) - K_{II}\left(6 - 12\tan^2\left(\frac{\varphi_o}{2}\right)\right)\right] \\ &-32K_{III}^2 \tan\left(\frac{\varphi_o}{2}\right)\left(1 + \tan^2\left(\frac{\varphi_o}{2}\right)\right)^2 \\ &\left.\times\left[4K_I - 12K_{II}\tan\left(\frac{\varphi_o}{2}\right)\right]^2 + 64K_{III}^2\left(1 + \tan^2\left(\frac{\varphi_o}{2}\right)\right)^2\right\}^{-1/2} = 0 \end{aligned} \tag{2.4}$$

A further explanation can be obtained by referring to Schöllman et al. (2002). A simpler function that is helpful for practical applications was developed by Richard et al. (2005) as follows:

$$\varphi_o = \mp\left[A\frac{|K_{II}|}{K_I + |K_{II}| + |K_{III}|} + B\left(\frac{|K_{II}|}{K_I + |K_{II}| + |K_{III}|}\right)^2\right] \tag{2.5}$$

where $A = 140°$, $B = -70°$, $\varphi_o < 0°$ for $K_{II} > 0$ and $\varphi_o > 0°$ for $K_{III} < 0$ and $K_I > 0$. Based on the crack growth criteria presented above, Schöllman et al. and Richard's criteria are suitable for three-dimensional mixed mode problems (Richard et al., 2005). However, only one criterion could be implemented in the numerical calculation. Thus, Richard's criterion was used for the model of crack growth direction in the numerical calculation due to its simplicity.

2.3 NUMERICAL METHOD IN FRACTURE MECHANICS

Diverse numerical methods have been applied to solve problems in solid mechanics such as the meshless (Cai et al., 2016), boundary integral equation (Wang & Sun 2005), finite difference (Kimoto & Ichikawa 2015) and finite element methods. The finite element method (FEM) is one method that has been focused on by the vast majority of researchers (Pavlou, 2015). This is due to the advantages of the FEM, where it is able to handle complex geometries, a variety of engineering problems, complex restraints and complex loadings (Elishakoff & Ren, 1999). Also, researchers use FEM to simulate surface crack problems in various engineering applications (Kikuchi et al., 2014). In the following subsections, the FEM for surface cracks and the S-version of the FEM are reviewed.

2.3.1 Finite Element Models for Surface Cracks

Figure 2.5 shows the varieties of FEM models that are currently applicable for various engineering problems. Among these examples, it can be noticed that the S-FEM can be applied for numerous engineering issues, especially in relation to engineering structures and materials. However, it must be accepted that in reality each software model is an expert in a specific field and scope of a problem. For instance, the S-FEM is suitable for the simulation of surface crack problems due to its effectiveness in controlling the meshing process.

The growth of surface cracks has received a great deal of attention from researchers. One noticeable finding is with regard to crack shape development, which was first studied by Newman & Raju (1981). One of the assumptions made was that an initial semi-elliptical surface crack maintains its shape until fracture occurs with increased cracking based on Paris' law (Brighenti & Carpinteri, 2013; Carpinteri, 1993; Carpinteri et al., 2013; Hou, 2011). Numerous studies have investigated the evolution of crack shapes through the alternative current field measurement technique for various aspect ratios, and the SIF of corner cracks and round bars (Brighenti & Carpinteri, 2013; Carpinteri et al., 2013).

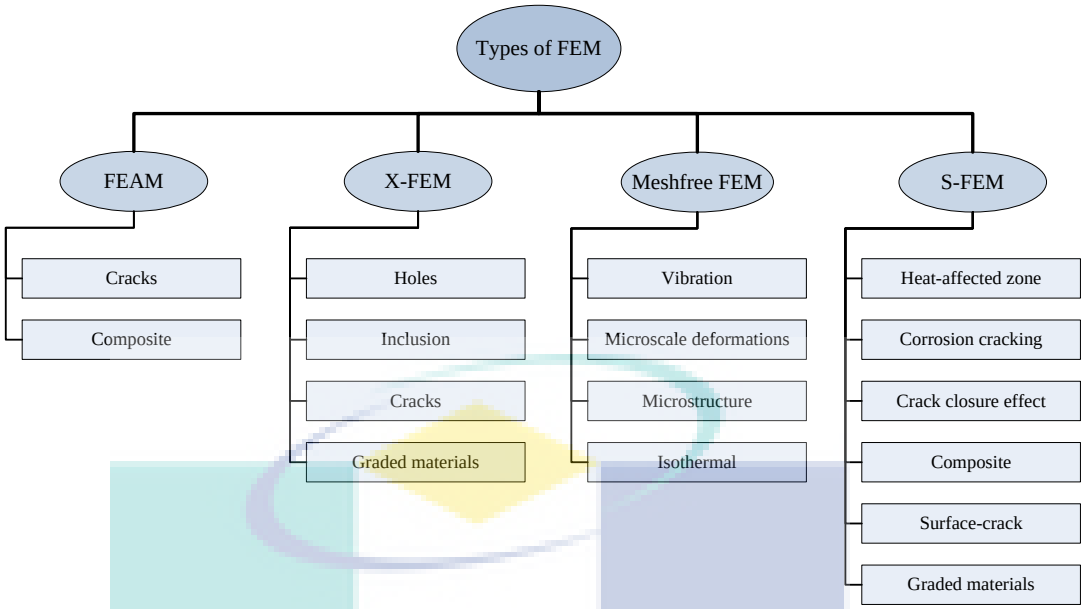

Figure 2.5 Varieties of FEMs in fracture mechanics field

The rate of growth of crack shapes has a tendency to be slow at the free surface. Hence, the use of a semi-elliptical crack shape during a simulation process allows it to evolve in a way that is close to reality. The evolution of crack shapes was found to be independent of the semi-elliptical shape, and researchers gradually began to discover why. Investigations started at the free and deepest surfaces of the cracks due to variations in the crack shapes (Hou, 2011). The discovery of the plasticity-induced crack closure phenomenon subsequently opened a new chapter in the development of crack shapes.

Many researchers studied the effects of crack closure behaviour since it is capable of decelerating the crack growth rate at the free surface (Aguilarespinosa et al., 2013; De Matos & Nowell, 2009; Hou 2011; Kim et al., 2013; Savaidis et al., 2010; Song & Shieh, 2004). The plasticity-induced crack closure phenomenon has been used to explain fatigue crack phenomena, such as the mean stress effect, crack growth retardation, and anomalous growth behaviour (Brighenti & Carpinteri, 2013; Carpinteri, 1993; Carpinteri et al., 2013; Hou, 2011).

Due to this phenomenon, the numerical simulation of surface cracks is complex, and fewer investigations have focused on three-dimensional models due to the complexity of the required computations. In order to model the problem in a

timely and cost-effective way, many types of FEMs have been introduced. The finite element alternating method (FEAM) (Thomas et al., 2000; Tian et al., 2014) and the X-FEM (Tran & Geniaut, 2012; Zhuang et al., 2014) were developed to simulate crack growth problems. Both methods utilize singular functions to capture the stress field at the crack tip. This requires the rebuilding of the finite element model. In the proposed approach, a less demanding analysis was targeted in order to increase its applicability to large-scale problems. From this perspective, the S-version Finite Element Model (S-FEM), which does not involve rebuilding the finite element model, was selected as a basis.

2.3.2 S-version Finite Element Model

An extended version of the FEM was needed since the problem involved complex geometries, fatigue loads, cracked structures and modelling of uncertainties. The conventional FEM was limited by the assumptions that arose with regard to the modelling of the entire problem and the environment. Therefore, it was prone to error and produced inaccurate results. The S-version FEM was introduced by Fish (1992) to enhance the capability of the FEM.

The S-FEM was developed from adaptive *h*- and *p*-methods of the meshing technique. However, the efficiency of these methods still needed to be improved by subdividing the finite element mesh using the *h*-method and increasing the degree of the polynomial using the *p*-method. Therefore, (Fish 1992) introduced *hp* procedures to integrate the improvement of both the polynomial order and the mesh refinement. The S-FEM has been used for various applications such as heat-affected zone materials (Kikuchi et al., 2012; Kikuchi, Wada, Shimizu et al., 2010), corrosion cracking (Kikuchi, Wada, Shmizu et al., 2011), the crack closure effect (Kikuchi, Wada, Maitireyimu et al., 2010), composite materials (Angioni et al., 2012) and surface cracks (Kikuchi, Wada & Suga, 2011).

Surface cracks are frequently found in aeronautical panels, riveted aeronautical reinforcements and pressure vessels due to their random loadings, uncertainty of the material, and unexpected environment. The crack growth data show a significant

amount of scatter (Choi et al., 2007; Stephens et al., 2001), especially when the structure has been subjected to fatigue loading (Duquesnay & Underhill, 2010; Underhill & Duquesnay, 2008, 2009). Scatter in crack nucleation (Kim et al., 2011; Liu & Mahadevan, 2009; Walz & Riesch-Oppermann, 2006) and crack growth rates (Grell & Laz, 2010; Hariharan et al., 2011; Iyyer et al., 2007; Kapoor et al., 2011) have also been reported. These uncertainties produce a distribution of outputs from a distribution of input parameters (Grell & Laz, 2010).

The S-version FEM is appropriate for solving three-dimensional fatigue surface crack problems. In addition, it is feasible to add the uncertainties quantification feature in the S-version FEM. So far, the embedded probabilistic analysis in the S-version FEM has rarely been published. The quantification of uncertainties in the S-version FEM is introduced and discussed in the following section.

2.4 UNCERTAINTIES QUANTIFICATION IN FEM

The initial defect originates from a notch due to a stress concentration. Since the structure is exposed to a fatigue load, the defect is extended to create a surface crack. The size of the initial surface crack is a random process in nature (Sain & Chandra Kishen, 2008). It is due to the uncertainty in the material homogeneity, initial flaws and the applied load (Wang, 1999). The conventional method does not account for the uncertainty in the fatigue crack growth analysis (Möller et al., 2003). In most practical cases, a safety factor approach is implemented to cater for all the uncertainties in the analysis. In addition, due to insufficient experimental data, it is assumed that the initial crack size is a deterministic value. Therefore, a method is needed that is capable of quantifying the uncertainties in the FEM. This section starts with a survey of the probabilistic analysis in FEM. This is then followed by explanations on the MCS, LHS, and upper and lower bounds.

2.4.1 Probabilistic Analysis in FEM

The availability of various probabilistic analysis software in FEM is presented in Table 2.1. The Proban software provides an integrated FEM and probabilistic analysis for analysing structural components. The enhancement of the FEM is restricted to the available analysis in the Proban software (Tvedt, 2006).

The NESSUS and COSSAN software are probabilistic software packages that offer a merging process with the FEM commercial software. However, the dependence on commercial FEA software arbitrarily leads to an increase in the cost. Furthermore, the NESSUS and COSSAN software also involve a number of costs.

The ANSYS Probabilistic Design System offers synchronization with the ANSYS commercial software. However, the dependence of the ANSYS Probabilistic Design System on ANSYS creates a software that can hardly couple with other finite element packages. The handling of random geometry parameters may also be cumbersome in certain cases in the ANSYS Probabilistic Design System (Reh et al., 2006). Thus, a probabilistic analysis with an advanced FEM is needed. The priority of the selection is the freedom to improve the source codes of FEM and the probabilistic analysis.

Based on the review of the probabilistic analysis in FEM, the MCS was selected as the probabilistic analysis in this research work. This was because the domain of possible responses can be estimated by modern MCS procedures (Schuëller & Pradlwarter, 2006). Even though various probabilistic techniques have been implemented in commercial software, still the results from the MCS are taken as a benchmark. Thus, the MCS, with an effective sampling strategy by the LHS, has been selected and presented in the following subsections.

2.4.2 Monte Carlo Simulation

The MCS is the most general probabilistic approach and one that is quite powerful for assessing parameter randomness (Cetin et al., 2013; Narayanan et al., 2016; Sanches

et al., 2015). Figure 2.6 shows the research trend in the Monte Carlo (MC) method that covers the scientific study of material failure (Leira et al., 2016; Rodríguez et al., 2015; Wang et al.m 2014) and industrial case studies (Cai et al., 2015; Kim et al., 2016). The trend shows that the main focus was more on the sampling techniques (Estecahandy et al., 2015; Rajabi et al., 2015; Shields et al., 2015), a new diagram for presenting the results (Kaczor et al., 2016) and the applications (Kaczor et al., 2016; Leira et al., 2016). The combination of MCS and S-FEM is a new trend within the scope of this research.

Table 2.1 Review of probabilistic analysis in FEM

Software	Model and approaches used	Reference
Proban	• FORM, SORM, adaptive response surface, nested reliability analysis, MCS, stratified simulation, directional simulation, design point simulation, axis orthogonal simulation and LHS	Tvedt (2006)
NESSUS	• Interfaced with ABAQUS, ANSYS, DYNA3D, LS-DYNA, NASA_GRC_FEM, MADYMO, MSC.NASTRAN, PRONTO, and USER_DEFINED. • Monte Carlo simulation, first-order reliability method, advanced mean value method and adaptive importance sampling	Thacker et al. (2006)
ANSYS Probabilistic Design System	• Using ANSYS solver for FEM • MCS with LHS	Reh (2006)
COSSAN	• FEA solved by interfaced FEM or standalone toolbox. • MCS, LHS.	Schuëller & Pradlwarter (2006)

The Monte Carlo sampling (MCS) method has received interest as a powerful tool for solving important physical problems and producing reliable outcomes. The MCS results have become the benchmark for any new development in probabilistic analysis codes (Helton & Davis, 2003; Janssen, 2013). The advantage of the Monte Carlo approach is in the characterisation and quantification of uncertainty. However,

the major issues to be solved are the time taken and the huge number of samples produced by the MCS. Therefore, an MCS in combination with the LHS is required.

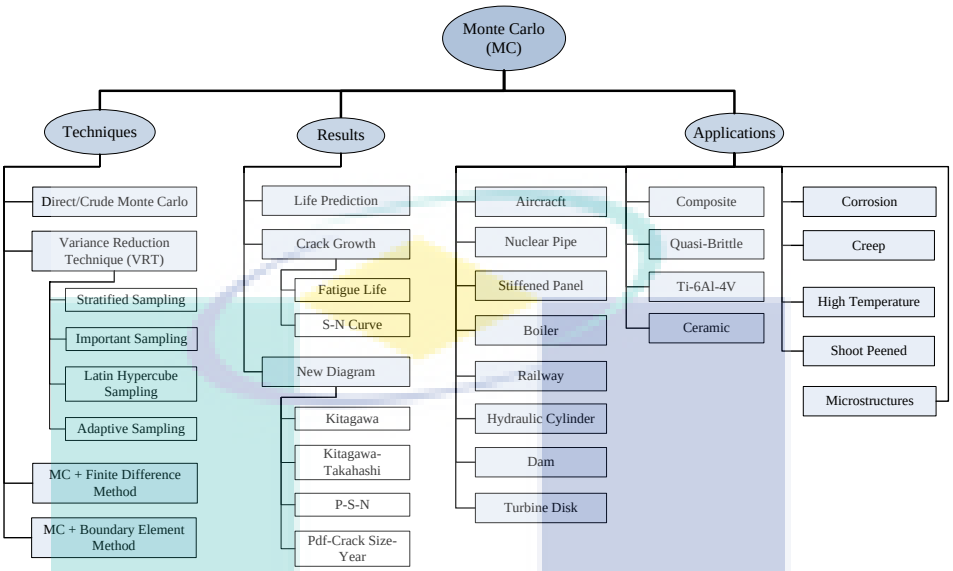

Figure 2.6 Research trend in MC

2.4.3 Latin Hypercube Sampling

The LHS provides a dense stratification over the range of each uncertain parameter. As a result, the LHS generates a small sample size. Each sample is generated with a structured form and randomized process (Sallberry et al., 2007). Unlike the MCS, the sample avoids generation in a same range of values, hence, making the LHS very effective. The effectiveness of the LHS and MCS in the characterisation of uncertainty has been adopted in the S-FEM in order to model a real application in the engineering field. The S-FEM is a basis for the adoption of probabilistic analysis in a structural analysis.

A significant number of powerful sampling techniques are available (Beer & Liebscher, 2008). Hence, this study employed the LHS as a numerically efficient simulation technique for the improvement of numerical feasibility. The LHS is efficient at estimating the mean values and standard deviations in a structural analysis, and is even more efficient than the standard Monte Carlo (Olsson et al. 2003) method.

In addition, the LHS is capable of preparing the bounds that are to be used for analysing the distribution of the results.

2.4.4 Bounds

Sets of random values are required to simulate variables in the MCS. Each generated variable produces a corresponding result until a distribution of the results is obtained for the set of random input variables. Then, all the results are averaged to obtain a mean value, and upper and lower bounds. The lowest result is represented as the lower bound and the highest result is represented as the upper bound. The bounds are produced from a certain relation of mean, standard deviation and number of samples of the uncertain variables. Based on the mean, and upper and lower bounds, a 95% confidence level in the bounds can be calculated.

In order to take account of the uncertainty of the variables, the bounds may be determined for the variables concerned (Möller et al., 2003). The upper and lower bounds offer a variability quantification that extracts from the width of the bounds. In addition, the upper and lower bounds produce statistical information that is essential for a characteristic study of the random variables. In addition, the upper and lower bounds are capable of reducing the computational burden for the development of a reliable system (Ramirez-Marquez & Levitin, 2008). The fatigue strength and characteristic life of a complex structure with multiple similar structural details can be calculated at a certain level of bounds (Huang et al., 2012).

The fatigue strength and life can be calculated at a 95% confidence level in the bounds due to their convenience and simplicity for applications in fatigue analysis. For instance, aircraft structural designs have used a 95% confidence level (Huang et al., 2012). Therefore, the 95% confidence level of the upper and lower bounds were computed in this thesis to indicate the randomness of the distribution and the range of the results.

The overall review pertaining to the analysis of surface cracks using FEM and the probabilistic approach has been presented. This chapter ends with the conclusion or the findings from the literature review.

2.5 SUMMARY

Despite the consistent enhancements achieved in the simulation of fatigue crack growth and life, the merging with probabilistic methods remains poorly established, particularly for multiple surface cracks with potentially complex mesh refinements and rebuilding issues.

The application of unrealistic safety factors and a deterministic initial crack size may lead to an unreliable residual life, resulting in uneconomical maintenance intervals (Wang 1999). Therefore, a probabilistic approach with different sampling strategies is demanded in the analysis of fatigue crack growth.

There is an insufficient number of software available for the simulation of fatigue in surface cracks due to the geometrical complexities involved. The S-FEM technique is able to implement different components or structure, notch and crack configurations. The mesh generator is accurate and less time-consuming.

The most widely used sampling strategy in FEM is the MC sampling due to the ability of the MCS to bridge the gap between deterministic and probabilistic concepts (Schuëller & Pradlwarter, 2006). Figure 2.7 shows the present research work in bridging the gap between both concepts, together with the implementation of the LHS. The combination of all the methodologies produced the Probabilistic S-version Finite Element Model (ProbS-FEM). Chapter 3 presents the methodology for the ProbS-FEM.

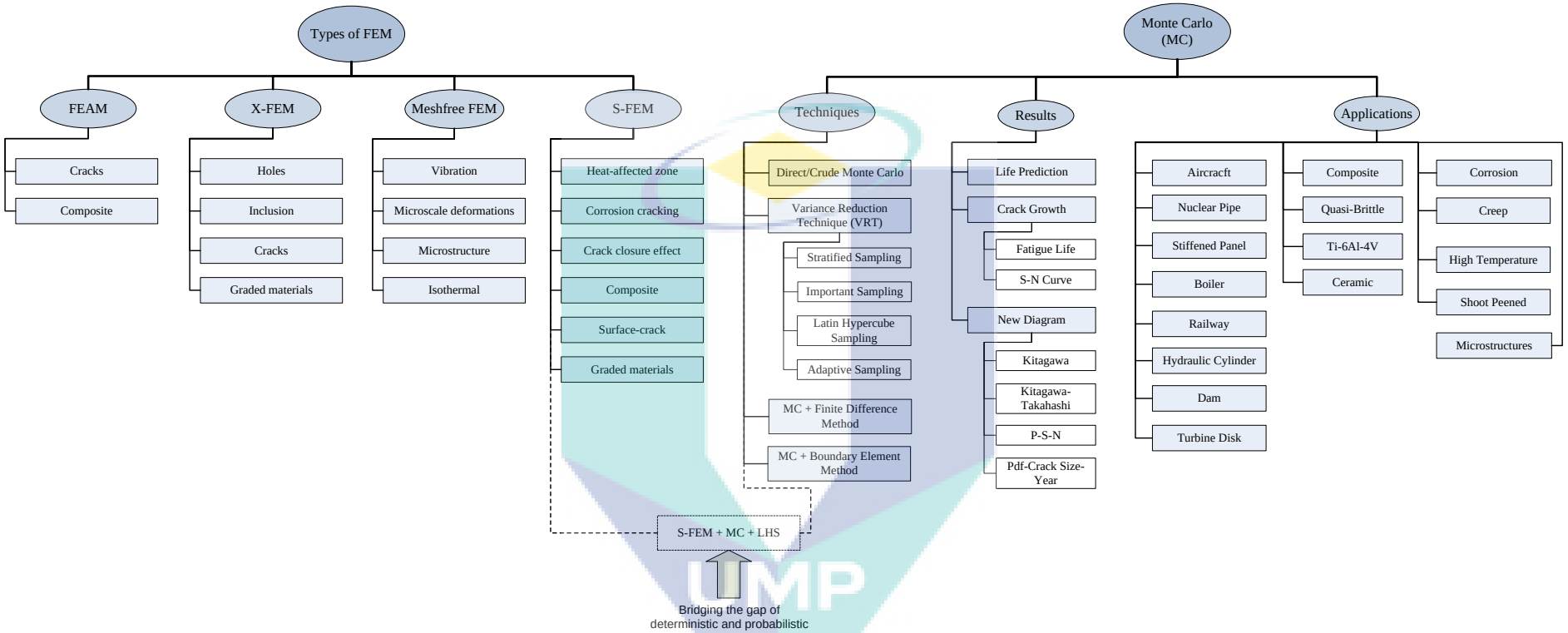

Figure 2.7 Research gap between deterministic and probabilistic approach that has been bridged by the current research work

CHAPTER III

PROBABILISTIC S-VERSION FINITE ELEMENT METHOD

3.1 CHAPTER OUTLINE

This chapter presents the formulation of a three-dimensional stress and surface crack growth analysis using the ProbS-FEM. The explanation starts with an overview of the methods, followed by the general finite element formulation. Then, the calculation of the stiffness matrix at the overlaid area between the global and local area is presented. After the completion of the matrix formulation, the surface crack growth procedure and fatigue crack growth model are described. Then, the embedded probabilistic analysis in the finite element model is discussed. The enhancement of the sampling method is elaborated under the section on the LHS. Finally, yet most importantly, the experimental setup is presented at the end of this chapter.

3.2 INTRODUCTION TO THE ProbS-FEM

The ProbS-FEM methodology was divided into three major parts, as shown in Figure 3.1. The main procedures were the probabilistic, deterministic and experimental works. The deterministic part means that the calculation was independent of random data. The deterministic analysis was computed from the setting up of the input data, the mesh generation for the local and global regions, the finite element formulation and the calculation of the surface crack growth.

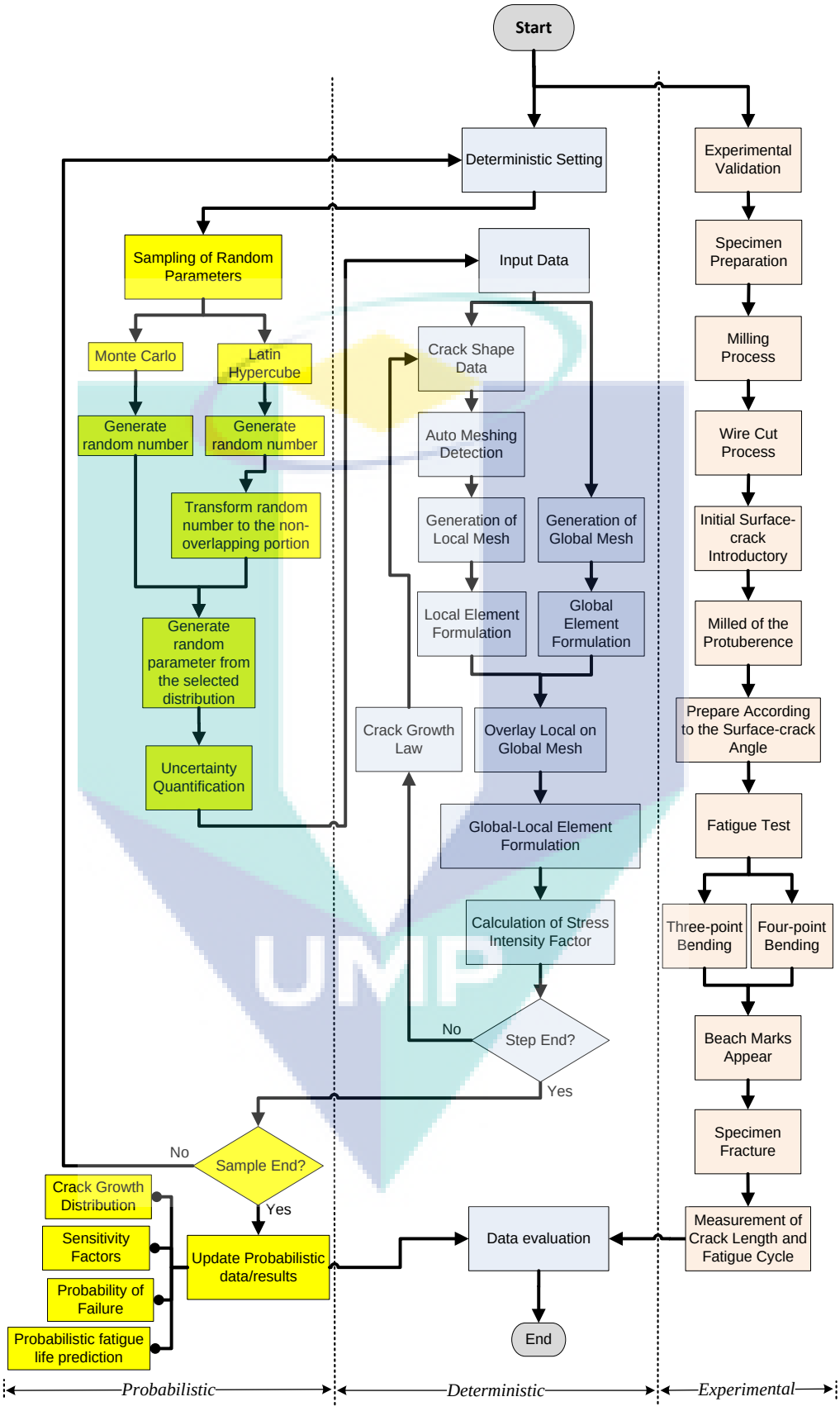

Figure 3.1 Overall diagram of the methods

Meanwhile, the probabilistic part started with the sampling of the random parameters and the supply to the deterministic analysis. Since the deterministic part was independent of random data, the exact random parameters that were generated were used for supplying the parameters to the deterministic part. As the calculation was computed for the deterministic part, the probabilistic information was extracted at the end of the analysis. The evaluation of the results was validated by the experimental results for clarification purposes. In order to get a basic idea of the ProbS-FEM, the explanation of the deterministic part begins with the general finite element formulation as below.

3.3 FINITE ELEMENT FORMULATION

This section discusses the formulation of a three-dimensional stress analysis problem. The stress-strain relations are given by

$$\{\sigma\} = [D]\{\varepsilon\} \tag{3.1}$$

where $[D]$ is the material property matrix. The strain-displacement relations can be expressed as

$$\{\varepsilon\} = [B]\{u\} \tag{3.2}$$

where $[B]$ is the deformation matrix. Considering the foregoing developments, Eq. (3.1) can be expressed as

$$\{\sigma\} = [D][B]\{u\} \tag{3.3}$$

where $\{u\}$ is the displacement obtained from the relation between the stiffness and loading matrices. The force is expressed as

$$\{F\} = [k]\{u\} \tag{3.4}$$

where the stiffness matrix $[k]$ is calculated as

$$[k] = \int_{\Omega} [B]^T [D][B] d\Omega \tag{3.5}$$

Further details of the derivation of the ProbS-FEM formulation is discussed in the following section. The formulation was focused within the context of the ProbS-FEM concept.

3.4 MATHEMATICAL FORMULATION OF THE ProbS-FEM

This section presents the mathematical formulation of the ProbS-FEM, which is an integration of the S-version Finite Element Method and the probabilistic approach. The primary focus of this section is the combined development of the program. It is the main contribution of this thesis. The combined program is known as the ProbS-FEM. Therefore, a detailed explanation is essential. This section is divided into three subsections. The first explains the development of the stiffness matrix at the overlaid region. This is followed by the implementation of surface crack growth in the ProbS-FEM. The fatigue crack growth is discussed in the third subsection.

3.4.1 Stiffness Matrix at Overlaid Region

Figure 3.2 shows the concept of the ProbS-FEM implementation in the analysis of surface cracks. A coarser mesh was generated at the global area, Ω^G while a denser mesh was used for the local area, Ω^L. The local area covered the vicinity of the crack front area. During the implementation of the global mesh, the crack tip area was temporarily neglected to allow the generation of a mesh for the whole domain. Subsequently, the mesh around the crack front area was taken into account during the implementation of the local mesh. Then, the local mesh was overlaid on the global mesh. Γ represents the boundary of each region. Let Γ^u be the boundary of the constrained displacement and Γ^t be the boundary of the force that was applied at the global region. The overlaid boundary was represented by Γ^{GL}.

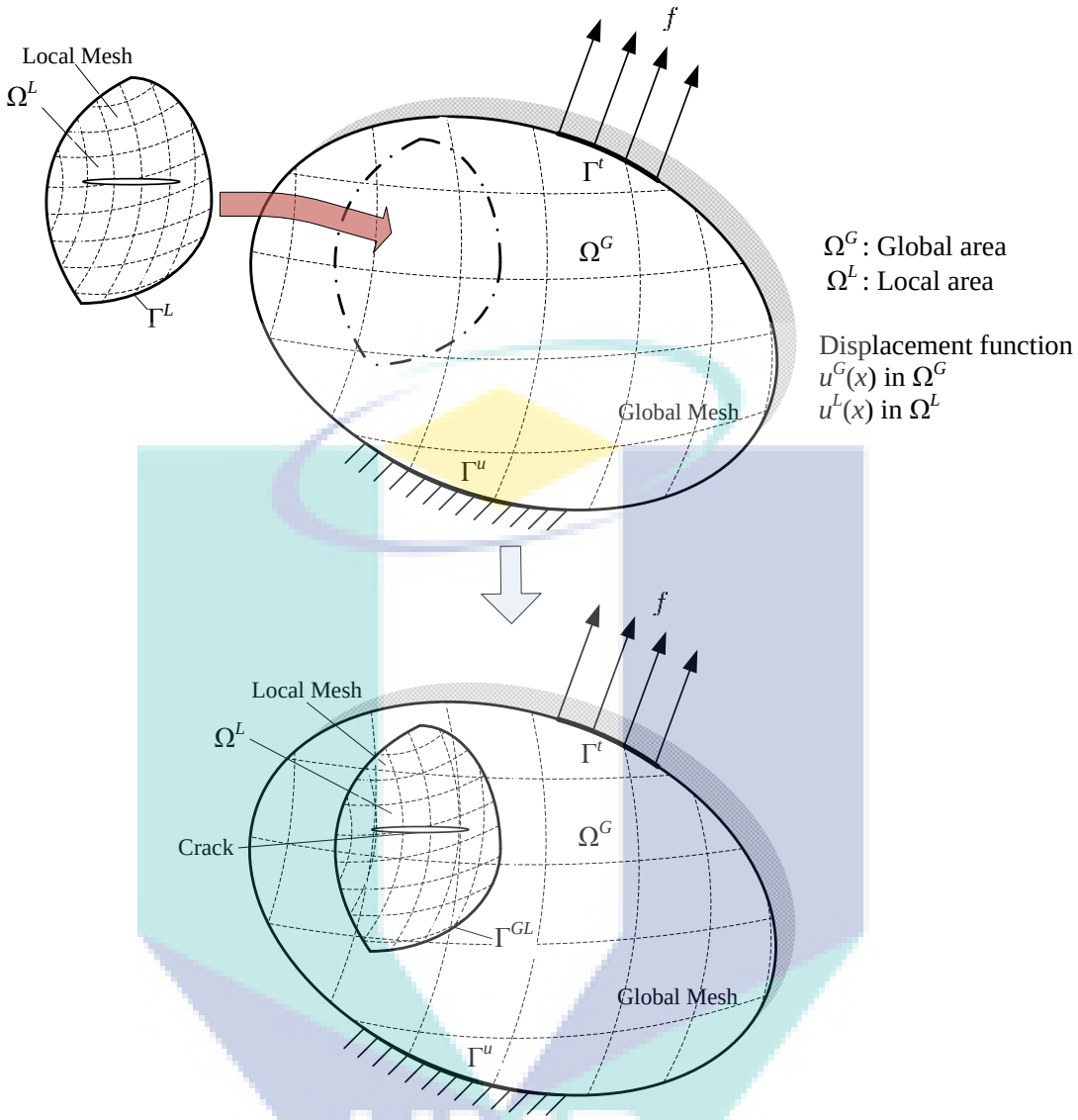

Figure 3.2 Concept of the S-FEM

It was crucial to decide on the size of the local mesh area since the growth of the crack was affected by the calculation of the displacement function. The displacement in the overlaid area was calculated from the global and local meshes, as shown below

$$u(x) = \begin{cases} u^G(x) & x \in \Omega^G - \Omega^L \\ u^G(x) + u^L(x) & x \in \Omega^L \end{cases} \tag{3.6}$$

A virtual displacement is all the possible displacements that a node might move in. The virtual displacement for the local and overlaid area is given by

$$\delta u(x) = \begin{cases} \delta u^G(x) & x \in \Omega^G - \Omega^L \\ \delta u^G(x) + \delta u^L(x) & x \in \Omega^L \end{cases} \tag{3.7}$$

The principle of virtual work states that the work done by forces in any virtual displacement of the body is equal to zero. Therefore, the equation is expressed by

$$\begin{aligned} &\int_\Omega (\sigma_x \delta\varepsilon_x + \sigma_y \delta\varepsilon_y + \sigma_z \delta\varepsilon_z + \tau_{xy}\delta\gamma_{xy} + \tau_{yz}\delta\gamma_{yz} + \tau_{zx}\delta\gamma_{zx}) d\Omega \\ &- \int_\Omega (b_x \delta u + b_y \delta v + b_z \delta w) d\Omega - \int_{\Gamma^t} (f_x \delta u + f_y \delta v + f_z \delta w) d\Gamma = 0 \end{aligned} \tag{3.8}$$

where σ and $\delta\varepsilon$ are the stress and virtual strain vector, respectively. Moreover, Ω is the domain of interest, b is the body force per unit volume, t is the vector of the boundary tractions, Γ^t is the part of the boundary on which the displacements are prescribed, and f is the nodal force. These components can be represented in matrix form as follows:

$$\begin{gathered} \{\sigma\} = \begin{Bmatrix} \sigma_x \\ \sigma_y \\ \sigma_z \\ \tau_{xy} \\ \tau_{yz} \\ \tau_{zx} \end{Bmatrix} \quad \{\varepsilon\} = \begin{Bmatrix} \delta\varepsilon_x \\ \delta\varepsilon_y \\ \delta\varepsilon_z \\ \delta\gamma_{xy} \\ \delta\gamma_{yz} \\ \delta\gamma_{zx} \end{Bmatrix} \quad \{f\} = \begin{Bmatrix} f_x \\ f_y \\ f_z \end{Bmatrix} \\ \{b\} = \begin{Bmatrix} b_x \\ b_y \\ b_z \end{Bmatrix} \quad \{u\} = \begin{Bmatrix} u \\ v \\ w \end{Bmatrix} \end{gathered} \tag{3.9}$$

Considering Eq. (3.9) in Eq. (3.8) yields a simpler equation of virtual work, which is shown as

$$\int_\Omega \{\delta\varepsilon\}^T \{\sigma\} d\Omega - \int_\Omega \{\delta u\}^T \{b\} d\Omega - \int_{\Gamma^t} \{\delta u\}^T \{f\} d\Gamma = 0 \tag{3.10}$$

Since the stress-strain relationship is expressed as $\{\sigma\} = [D]\{\varepsilon\}$, Eq. (3.10) can be expressed as

$$\int_{\Omega} \{\delta\varepsilon\}^T [D]\{\varepsilon\} d\Omega - \int_{\Omega} \{\delta u\}^T \{b\} d\Omega - \int_{\Gamma^t} \{\delta u\}^T \{f\} d\Gamma = 0 \tag{3.11}$$

The material property matrix $[D]$ can be referred to in Eq. (0.1) in Appendix A. Since there are global and local regions, the strain in Eq. (3.11) for each region is expressed as follows

$$\varepsilon(x) = \begin{cases} \varepsilon^G(x) & x \in \Omega^G - \Omega^L \\ \varepsilon^G(x) + \varepsilon^L(x) & x \in \Omega^L \end{cases} \tag{3.12}$$

Therefore, Eq. (3.11) can be written as

$$\begin{aligned} &\int_{\Omega^{G-L}} \{\delta\varepsilon^G\}^T [D]\{\varepsilon^G\} d\Omega - \int_{\Omega^{G-L}} \{\delta u^G\}^T \{b\} d\Omega - \int_{\Gamma^{G-L}} \{\delta u^G\}^T \{f\} d\Gamma \\ &\quad + \int_{\Omega^L} \left(\{\delta\varepsilon^G\}^T + \{\delta\varepsilon^L\}^T\right) [D] \left(\{\varepsilon^G\} + \{\varepsilon^L\}\right) d\Omega \\ &- \int_{\Omega^L} \left(\{\delta u^G\}^T + \{\delta u^L\}^T\right) \{b\} d\Omega - \int_{\Gamma^L} \left(\{\delta u^G\}^T + \{\delta u^L\}^T\right) \{f\} d\Gamma = 0 \end{aligned} \tag{3.13}$$

The first three terms are for the global minus the local region, and the remaining terms are only for the local region. The displacement component for the physical quantity at any point within the element is formulated by

$$\{u^G\} = [N]\{u^{eG}\} \qquad \{u^L\} = [N]\{u^{eL}\} \tag{3.14}$$

where the e character represents the element subscript, and $\{u^{eG}\}$ and $\{u^{eL}\}$ are the displacements of the element node for the global and local regions, respectively. The displacement of each node in an element is represented by u, v and w for the components of the x-, y- and z-axes, respectively. Since there are 20 nodes in a hexahedron element, as shown in Figure 3.3, the displacement matrix of each node is given by

$$\{u^e\} = \{u_1 \quad v_1 \quad w_1 \quad u_2 \quad v_2 \quad w_2 \quad ..... \quad u_{20} \quad v_{20} \quad w_{20}\}^T \tag{3.15}$$

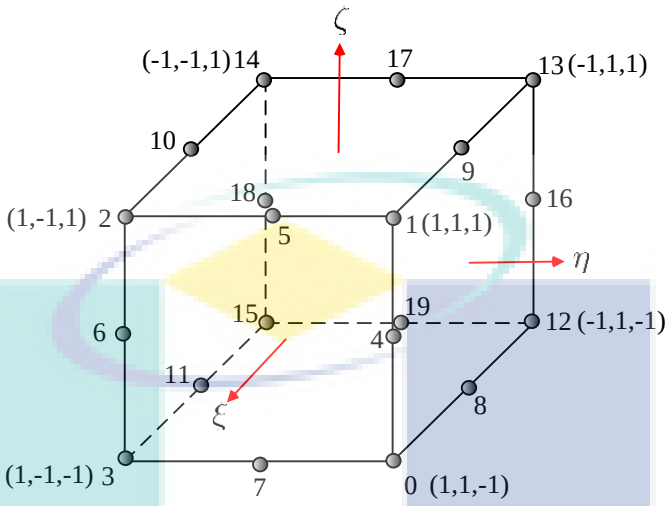

Figure 3.3 Hexahedron element with 20 nodes

Different geometries produce different shapes of an element. Then, a different function is computed to represent the shape of that element. In this research work, a three-dimensional hexahedron element was used, since it is sensible with respect to the corner angle. The shape functions were used to formulate finite element equations for various types of physical problems. These were derived to satisfy certain required conditions at the nodes. The $[N]$ in Eq. (3.14) is the shape function matrix, and the detailed derivation can be referred to in Eq. (0.2) in Appendix A.

Meanwhile, the strain in Eq. (3.13) can be expressed by the following equation

$$\{\varepsilon^G\} = [B^G]\{u^{eG}\} \qquad \{\varepsilon^L\} = [B^L]\{u^{eL}\} \tag{3.16}$$

where $[B^G]$ and $[B^L]$ are the matrices of the displacement strain for the global and local regions, respectively. Details of the $[B]$ matrix and the expanded development of Eq. (3.16) can be referred to in Eq. (0.3) in Appendix A.

Recalling Eq. (3.13), the equation can be split up into separate terms. The first term is

$$\int_{\Omega^{G-L}} \{\delta\varepsilon^G\}^T [D] \{\varepsilon^G\} d\Omega = \int_{\Omega^{G-L}} \{\delta u^{eG}\}^T [B^G]^T [D] [B^G] \{u^{eG}\} d\Omega \tag{3.17}$$

The second term is

$$\int_{\Omega^{G-L}} \{\delta u^G\}^T \{b\} d\Omega = \int_{\Omega^{G-L}} \{\delta u^{eG}\}^T [N]^T \{b\} d\Omega \tag{3.18}$$

The third term is

$$\int_{\Gamma^{G-L}} \{\delta u^G\}^T \{f\} d\Gamma = \int_{\Gamma^{G-L}} \{\delta u^{eG}\}^T [N]^T \{f^e\} d\Gamma \tag{3.19}$$

The fourth term is

$$\begin{aligned} &\int_{\Omega^L} \left(\{\delta\varepsilon^G\}^T + \{\delta\varepsilon^L\}^T\right) [D] \left(\{\varepsilon^G\} + \{\varepsilon^L\}\right) d\Omega \\ &= \int_{\Omega^L} \{\delta u^{eG}\}^T [B^G]^T [D] [B^G] \{u^{eG}\} d\Omega \\ &+ \int_{\Omega^L} \{\delta u^{eG}\}^T [B^G]^T [D] [B^L] \{u^{eL}\} d\Omega \\ &+ \int_{\Omega^L} \{\delta u^{eL}\}^T [B^L]^T [D] [B^G] \{u^{eG}\} d\Omega \\ &+ \int_{\Omega^L} \{\delta u^{eL}\}^T [B^L]^T [D] [B^L] \{u^{eL}\} d\Omega \end{aligned} \tag{3.20}$$

The fifth term is

$$\begin{aligned} \int_{\Omega^L} \left(\{\delta u^G\}^T + \{\delta u^L\}^T\right) \{b\} d\Omega &= \int_{\Omega^L} \{\delta u^{eG}\}^T [N]^T \{b\} d\Omega \\ &+ \int_{\Omega^L} \{\delta u^{eL}\}^T [N]^T \{b\} d\Omega \end{aligned} \tag{3.21}$$

The sixth term is

$$\int_{\Gamma^L}\left(\{\delta u^G\}^T+\{\delta u^L\}^T\right)\{f\}d\Gamma=\int_{\Gamma^L}\{\delta u^{eG}\}^T[N]^T\{f^e\}d\Gamma+\int_{\Gamma^L}\{\delta u^{eL}\}^T[N]^T\{f^e\}d\Gamma \tag{3.22}$$

Since $\{\delta u^{eG}\}$ and $\{u^{eG}\}$ are constants, Eq. (3.13) can be expressed as

$$\begin{aligned}
&\{\delta u^{eG}\}^T\{u^{eG}\}\int_{\Omega^{G-L}}[B^G]^T[D][B^G]d\Omega\\
&+\{\delta u^{eG}\}^T\{u^{eG}\}\int_{\Omega^L}[B^G]^T[D][B^G]d\Omega\\
&+\{\delta u^{eG}\}^T\{u^{eL}\}\int_{\Omega^L}[B^G]^T[D][B^L]d\Omega\\
&+\{\delta u^{eL}\}^T\{u^{eG}\}\int_{\Omega^L}[B^L]^T[D][B^G]d\Omega\\
&+\{\delta u^{eL}\}^T\{u^{eL}\}\int_{\Omega^L}[B^L]^T[D][B^L]d\Omega\\
=\{\delta u^{eG}\}^T&\int_{\Omega^{G-L}}[N]^T\{b\}d\Omega+\{\delta u^{eG}\}^T\int_{\Omega^L}[N]^T\{b\}d\Omega\\
&+\{\delta u^{eL}\}^T\int_{\Omega^L}[N]^T\{b\}d\Omega\\
+\{\delta u^{eG}\}^T&\int_{\Gamma^{G-L}}[N]^T\{f^e\}d\Gamma+\{\delta u^{eG}\}^T\int_{\Gamma^L}[N]^T\{f^e\}d\Gamma\\
&+\{\delta u^{eL}\}^T\int_{\Gamma^L}[N]^T\{f^e\}d\Gamma
\end{aligned} \tag{3.23}$$

Since $\int_{x^{G-L}}f(x)dx+\int_{x^L}f(x)dx=\int_{x^G}f(x)dx$, the element stiffness and force matrices are identified as

$$\begin{aligned}
[K_{GG}]&=\int_{\Omega^G}\left[B^G\right]^T[D]\left[B^G\right]d\Omega\\
[K_{GL}]&=\int_{\Omega^L}\left[B^G\right]^T[D]\left[B^L\right]d\Omega\\
[K_{LG}]&=\int_{\Omega^L}\left[B^L\right]^T[D]\left[B^G\right]d\Omega
\end{aligned} \tag{3.24}$$

$$[K_{LL}] = \int_{\Omega^L} \left[B^L\right]^T [D] \left[B^L\right] d\Omega$$

$$\begin{Bmatrix} F_G^e \\ F_L^e \end{Bmatrix} = \begin{Bmatrix} \int_{\Omega^G} [N]^T \{f^e\} d\Omega \\ \int_{\Omega^L} [N]^T \{f^e\} d\Omega \end{Bmatrix}$$

$$\begin{Bmatrix} b_G^e \\ b_L^e \end{Bmatrix} = \begin{Bmatrix} \int_{\Omega^G} [N]^T \{b\} d\Omega \\ \int_{\Omega^L} [N]^T \{b\} d\Omega \end{Bmatrix}$$

Eq. (3.23) can be written as

$$\begin{aligned} &[K_{GG}]\{u^{eG}\} + [K_{GL}]\{u^{eL}\} + [K_{LG}]\{u^{eG}\} + [K_{LL}]\{u^{eL}\} \\ &= \{F_G^e\} + \{b_G^e\} + \{F_L^e\} + \{b_L^e\} \end{aligned} \tag{3.25}$$

A three-dimensional ProbS-FEM having e number of elements is formulated by

$$\begin{aligned} &\sum^{e} ([K_{GG}]\{u^{eG}\} + [K_{GL}]\{u^{eL}\} + [K_{LG}]\{u^{eG}\} + [K_{LL}]\{u^{eL}\}) \\ &= \sum^{e} (\{F_G^e\} + \{b_G^e\} + \{F_L^e\} + \{b_L^e\}) \end{aligned} \tag{3.26}$$

The matrix form of the finite element formulation is expressed as

$$\begin{bmatrix} K_{GG} & K_{GL} \\ K_{LG} & K_{LL} \end{bmatrix} \begin{Bmatrix} u^G \\ u^L \end{Bmatrix} = \begin{Bmatrix} F_G \\ F_L \end{Bmatrix} \tag{3.27}$$

where $\{F_G\}$ and $\{F_L\}$ are the nodal forces at THE global and local regions, respectively, and the matrices $[K_{GL}]$ and $[K_{LG}]$ represent the stiffness matrices of the merging area. The complicated part in the ProbS-FEM was the construction of the stiffness matrix of the overlaid region between the local and global matrices, $[K_{GL}]$ and $[K_{LG}]$. The relationships between $[K_{GL}]$ and $[K_{LG}]$ are shown below.

$$[K_{GL}] = \int_{\Omega^L} \left[B^G\right]^T [D] \left[B^L\right] d\Omega = [K_{LG}]^T \tag{3.28}$$

$$[K_{GL}] = \int_{\Omega^L} \sum_{p=1}^{n} \sum_{q=1}^{n^n} N_i(\xi^G, \eta^G, \zeta^G) D_{ijk} N_i(\xi^L, \eta^L, \zeta^L) d\Omega \tag{3.29}$$

The $[B^G]$ matrix is the strain displacement matrix in the global region. During the overlaying process between the local and global regions, the integration of the Gauss point was considered. The Gauss point is an integration point within an element at which the integrals are evaluated numerically. Since the local element overlapped with the global element, it was necessary to consider the relationship between the Gauss point in the local and global elements. Each local and global element has its own coordinates system. Figure 3.4 shows the overlaying concept between the local and global regions in two dimensions for clarity. In the implementation of the ProbS-FEM, a three-dimensional element was computed.

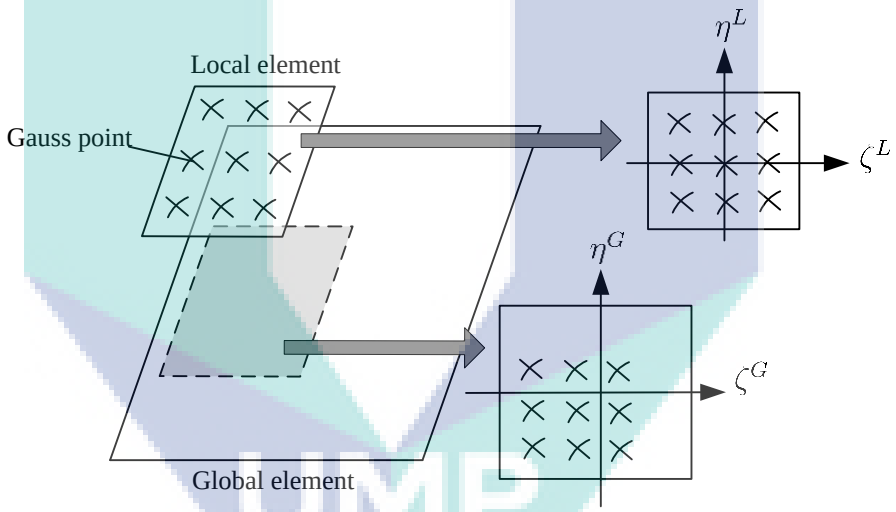

Figure 3.4 Merged element between local and global regions

Both the global and local elements have their own local coordinates, where (ξ^L, η^L, ζ^L) represents the Gaussian point coordinates for the local element, and (ξ^G, η^G, ζ^G) represents the Gaussian point coordinates for the global element. The construction of the $[B^G]$ matrix in Eq. (3.28) requires the (ξ^G, η^G, ζ^G) coordinate. The (ξ^G, η^G, ζ^G) coordinate was calculated from the transformation of the (ξ^L, η^L, ζ^L) coordinate. This transformation was computed using the Newton-Raphson method of iterative calculation.

In order to determine the Gaussian point in the global element,(ξ^G, η^G, ζ^G), the physical nodal coordinate of the local element (x, y, z) was calculated by

$$x = \sum_{i=1}^{n^L} N_i(\xi^L, \eta^L, \zeta^L) X_i^L$$
$$y = \sum_{i=1}^{n^L} N_i(\xi^L, \eta^L, \zeta^L) Y_i^L \tag{3.30}$$
$$z = \sum_{i=1}^{n^L} N_i(\xi^L, \eta^L, \zeta^L) Z_i^L$$

(ξ^L, η^L, ζ^L) are the local coordinates of the Gaussian point in the local element, which is known after the generation of local mesh, while (X_i^L, Y_i^L, Z_i^L) are the nodal coordinates of the local mesh supplied by the mesh generator. N_i is the shape function, as shown in Eq. (0.2) in Appendix A. The physical nodal coordinates (x, y, z) of the local element were determined from Eq. (3.30). The relationship between the physical nodal coordinates, (x, y, z) and the Gaussian point in the global element, (ξ^G, η^G, ζ^G) is shown as

$$x = \sum_{i=1}^{n^G} N_i(\xi^G, \eta^G, \zeta^G) X_i^G$$
$$y = \sum_{i=1}^{n^G} N_i(\xi^G, \eta^G, \zeta^G) Y_i^G \tag{3.31}$$
$$z = \sum_{i=1}^{n^G} N_i(\xi^G, \eta^G, \zeta^G) Z_i^G$$

(X_i^G, Y_i^G, Z_i^G) are the nodal coordinates of the global mesh supplied by the mesh generator. In order to calculate the Gaussian point in the global element, (ξ^G, η^G, ζ^G), in Eq. (3.31), the Newton-Raphson method was computed. Trial values of the vectors of the local coordinates $(\overline{\xi}^G, \overline{\eta}^G, \overline{\zeta}^G)$ were set as $\overline{\xi}^G = 0$, $\overline{\eta}^G = 0$, $\overline{\zeta}^G = 0$ since $-1 < \overline{\xi}^G < 1$, $-1 < \overline{\eta}^G < 1$, $-1 < \overline{\zeta}^G < 1$. The range of the transformation from the

global to the local mesh was from -1 to 1. The product of the trial values of $\overline{\xi}^G = 0$, $\overline{\eta}^G = 0$, $\overline{\zeta}^G = 0$ was represented as $(\overline{x}, \overline{y}, \overline{z})$. The difference between (x, y, z) calculated from Eq. (3.30) and the estimated coordinates $(\overline{x}, \overline{y}, \overline{z})$ from the Newton-Raphson method was determined as

$$\begin{aligned} \triangle x &= x - \bar{x} \\ \triangle y &= y - \bar{y} \\ \triangle z &= z - \bar{z} \end{aligned} \tag{3.32}$$

The Newton-Raphson method continued the iteration for calculating $(\overline{\xi}^G, \overline{\eta}^G, \overline{\zeta}^G)$ until $(\triangle x, \triangle y, \triangle z) = (0, 0, 0)$. The value of $(\overline{\xi}^G, \overline{\eta}^G, \overline{\zeta}^G)$ was updated and used for the next iteration of the Newton-Raphson method by using the relationship of

$$\begin{aligned} \triangle x &= \frac{\delta \bar{x}}{\delta \bar{\xi}^G} \triangle \xi^G + \frac{\delta \bar{x}}{\delta \bar{\eta}^G} \triangle \eta^G + \frac{\delta \bar{x}}{\delta \bar{\zeta}^G} \triangle \zeta^G \\ \triangle y &= \frac{\delta \bar{y}}{\delta \bar{\xi}^G} \triangle \xi^G + \frac{\delta \bar{y}}{\delta \bar{\eta}^G} \triangle \eta^G + \frac{\delta \bar{y}}{\delta \bar{\zeta}^G} \triangle \zeta^G \\ \triangle z &= \frac{\delta \bar{z}}{\delta \bar{\xi}^G} \triangle \xi^G + \frac{\delta \bar{z}}{\delta \bar{\eta}^G} \triangle \eta^G + \frac{\delta \bar{z}}{\delta \bar{\zeta}^G} \triangle \zeta^G \end{aligned} \tag{3.33}$$

Eq. (3.33) can be expanded as

$$\begin{aligned} \triangle x = &\sum_{i=1}^{n^G} \left(\frac{\partial N_i(\bar{\xi}^G, \bar{\eta}^G, \bar{\zeta}^G)}{\partial \bar{\xi}^G} X_i \right) \triangle \bar{\xi}^G + \sum_{i=1}^{n^G} \left(\frac{\partial N_i(\bar{\xi}^G, \bar{\eta}^G, \bar{\zeta}^G)}{\partial \bar{\eta}^G} X_i \right) \triangle \bar{\eta}^G \\ &+ \sum_{i=1}^{n^G} \left(\frac{\partial N_i(\bar{\xi}^G, \bar{\eta}^G, \bar{\zeta}^G)}{\partial \bar{\zeta}^G} X_i \right) \triangle \bar{\zeta}^G \\ \triangle y = &\sum_{i=1}^{n^G} \left(\frac{\partial N_i(\bar{\xi}^G, \bar{\eta}^G, \bar{\zeta}^G)}{\partial \bar{\xi}^G} Y_i \right) \triangle \bar{\xi}^G + \sum_{i=1}^{n^G} \left(\frac{\partial N_i(\bar{\xi}^G, \bar{\eta}^G, \bar{\zeta}^G)}{\partial \bar{\eta}^G} Y_i \right) \triangle \bar{\eta}^G \\ &+ \sum_{i=1}^{n^G} \left(\frac{\partial N_i(\bar{\xi}^G, \bar{\eta}^G, \bar{\zeta}^G)}{\partial \bar{\zeta}^G} Y_i \right) \triangle \bar{\zeta}^G \\ \triangle z = &\sum_{i=1}^{n^G} \left(\frac{\partial N_i(\bar{\xi}^G, \bar{\eta}^G, \bar{\zeta}^G)}{\partial \bar{\xi}^G} Z_i \right) \triangle \bar{\xi}^G + \sum_{i=1}^{n^G} \left(\frac{\partial N_i(\bar{\xi}^G, \bar{\eta}^G, \bar{\zeta}^G)}{\partial \bar{\eta}^G} Z_i \right) \triangle \bar{\eta}^G \end{aligned} \tag{3.34}$$

$$+\sum_{i=1}^{n^G}\left(\frac{\partial N_i(\bar{\xi}^G,\bar{\eta}^G,\bar{\zeta}^G)}{\partial\bar{\zeta}^G}Z_i\right)\triangle\bar{\zeta}^G$$

In matrix form, the relationship can be simplified as

$$\begin{Bmatrix}\Delta x\\ \Delta y\\ \Delta z\end{Bmatrix}=[Q]\begin{Bmatrix}\Delta\bar{\xi}^G\\ \Delta\bar{\eta}^G\\ \Delta\bar{\zeta}^G\end{Bmatrix} \tag{3.35}$$

where $[Q]$ is equal to

$$\begin{bmatrix}\sum_{i=1}^{n^G}\frac{\partial N_i(\bar{\xi}^G,\bar{\eta}^G,\bar{\zeta}^G)}{\partial\bar{\xi}^G}X_i & \sum_{i=1}^{n^G}\frac{\partial N_i(\bar{\xi}^G,\bar{\eta}^G,\bar{\zeta}^G)}{\partial\bar{\eta}^G}X_i & \sum_{i=1}^{n^G}\frac{\partial N_i(\bar{\xi}^G,\bar{\eta}^G,\bar{\zeta}^G)}{\partial\bar{\zeta}^G}X_i\\ \sum_{i=1}^{n^G}\frac{\partial N_i(\bar{\xi}^G,\bar{\eta}^G,\bar{\zeta}^G)}{\partial\bar{\xi}^G}Y_i & \sum_{i=1}^{n^G}\frac{\partial N_i(\bar{\xi}^G,\bar{\eta}^G,\bar{\zeta}^G)}{\partial\bar{\eta}^G}Y_i & \sum_{i=1}^{n^G}\frac{\partial N_i(\bar{\xi}^G,\bar{\eta}^G,\bar{\zeta}^G)}{\partial\bar{\zeta}^G}Y_i\\ \sum_{i=1}^{n^G}\frac{\partial N_i(\bar{\xi}^G,\bar{\eta}^G,\bar{\zeta}^G)}{\partial\bar{\xi}^G}Z_i & \sum_{i=1}^{n^G}\frac{\partial N_i(\bar{\xi}^G,\bar{\eta}^G,\bar{\zeta}^G)}{\partial\bar{\eta}^G}Z_i & \sum_{i=1}^{n^G}\frac{\partial N_i(\bar{\xi}^G,\bar{\eta}^G,\bar{\zeta}^G)}{\partial\bar{\zeta}^G}Z_i\end{bmatrix} \tag{3.36}$$

Therefore, $(\triangle\bar{\xi}^G,\triangle\bar{\eta}^G,\triangle\bar{\zeta}^G)$ was updated as

$$\begin{Bmatrix}\Delta\bar{\xi}^G\\ \Delta\bar{\eta}^G\\ \Delta\bar{\zeta}^G\end{Bmatrix}=[Q]^{-1}\begin{Bmatrix}\Delta x\\ \Delta y\\ \Delta z\end{Bmatrix} \tag{3.37}$$

The value for the next trial, $(\bar{\xi}^G_{next},\bar{\eta}^G_{next},\bar{\zeta}^G_{next})$, was updated by

$$\begin{aligned}\bar{\xi}^G_{next}&=\bar{\xi}^G+\Delta\bar{\xi}^G\\ \bar{\eta}^G_{next}&=\bar{\eta}^G+\Delta\bar{\eta}^G\\ \bar{\zeta}^G_{next}&=\bar{\zeta}^G+\Delta\bar{\zeta}^G\end{aligned} \tag{3.38}$$

The iteration for seeking the value of (ξ^G,η^G,ζ^G) was updated until the value of $(\triangle\bar{\xi}^G,\triangle\bar{\eta}^G,\triangle\bar{\zeta}^G)$ became small enough. The iteration of the Newton-Raphson

method ended with a certain degree of convergence. The convergence was calculated based on the tolerance, (Tol) as

$$\sqrt{(\Delta\bar{\xi}^G)^2 + (\Delta\bar{\eta}^G)^2 + (\Delta\bar{\zeta}^G)^2} \leq Tol \tag{3.39}$$

Based on these procedures, the local coordinates in the global element, (ξ^G, η^G, ζ^G), could be estimated. The estimated value of (ξ^G, η^G, ζ^G) from the local coordinates in the local element,(ξ^L, η^L, ζ^L), was useful at the overlaid mesh region due to the calculation of the stiffness matrix at the overlaid mesh.

Once the value of the local coordinates in the global element,(ξ^G, η^G, ζ^G), was in hand, the $[B^G]$ matrix could be determined. The determination of the $[B^G]$ matrix enabled the overlaid stiffness matrices, $[K_{GL}]$ and$[K_{LG}]$, to be computed, as shown in Eq. (3.28). On completing the calculation for the overlaid stiffness matrix, the determination of the crack growth was considered as below.

3.4.2 Crack Growth

The calculation of the overlaid stiffness matrix and the displacement of each node were explained in Section 3.4.1. The focus of this subsection is on explaining the growth at the crack front in the ProbS-FEM. The stress intensity factor (SIF), $K$and the energy release rate were used as parameters to evaluate the crack growth in linear elastic fracture mechanics. A criterion was used to determine the direction of the crack growth.

The energy release rate was determined via the Virtual Crack Closure method (VCCM) (Okada et al., 2005). The VCCM technique was then extended to synchronise with the ProbS-FEM program. The VCCM considered the opening displacement near to the crack front, as shown in Figure 3.5. The joint reactions at five nodes at the back of the crack front were shown by f_i, where $i = \{1, 2, 3, 4, 5\}$. The opening displacement at the five nodes at the front edge of the crack front was shown by u_i, where $i = \{1, 2, 3, 4, 5\}$.

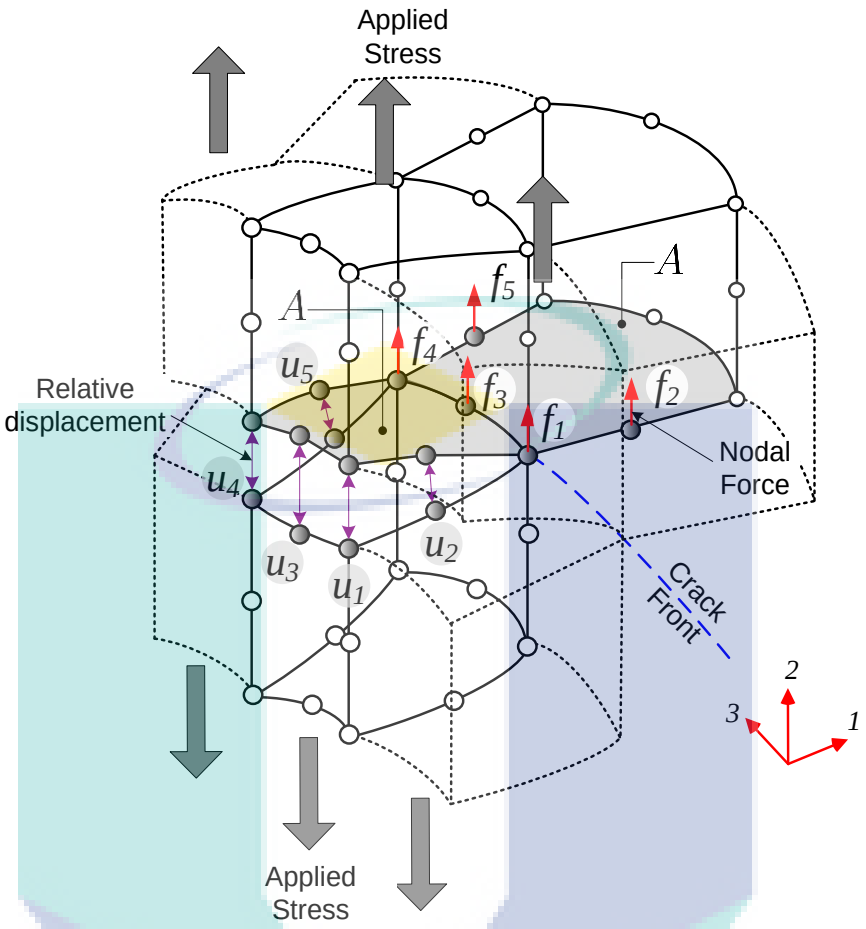

Figure 3.5 VCCM for local mesh at crack front

The displacement of the upper surface crack is represented by u_{iU} and the displacement of the lower surface crack is represented by u_{iL} Therefore, the opening displacement, u_i is expressed as

$$u_i = u_{iU} - u_{iL} \tag{3.40}$$

If the local and global meshes were overlaid in the analysis, the displacement was calculated based on a summation of the local and global displacements for the upper and lower surface cracks. Thus, the displacements for the upper and lower surface cracks were calculated as

$$u_{iU} = u_{iU}^{G} + u_{iU}^{L} \tag{3.41}$$

$$u_{iL} = u_{iL}^{G} + u_{iL}^{L}$$

However, the opening displacement in the global region is always zero due to the overlay technique in the ProbS-FEM. The opening displacement occurred in the local mesh only. Therefore,

$$u_{iU}^{G} = u_{iL}^{G} \tag{3.42}$$

Combining Eq. (3.41) and (3.42) in Eq. (3.40) yielded

$$u_i = (u_{iU}^{G} + u_{iU}^{L}) - (u_{iL}^{G} + u_{iL}^{L}) = u_{iU}^{L} - u_{iL}^{L} \tag{3.43}$$

As can be seen in Eq. (3.43), the total opening displacement, u_i at the node was represented by the local region only. Then, the calculated opening displacement was used for the calculation of the energy release rate.

The energy release rate, G for the non-symmetrical finite element face arrangement at the crack front was introduced by Okada et al. (2005). When the failure mode component, I was considered, Okada et al. proposed that the energy spent, ΔG_I be calculated during the opening of the crack for the area, S_1 as

$$\Delta G_I = \frac{1}{2}\int_{S_1} \sigma_{33}(r)\nu_3(\triangle - r)dS \tag{3.44}$$

The area of S_1 is shown in Figure 3.6. The failure modes I, II and III are shown in Figure 2.3. $\triangle$ and r are the length and width of the element perpendicular and parallel to the crack front, respectively as shown in Figure 3.6. σ_{33} is the cohesive stress in the plane of the crack ahead of the crack front with the first subscript 3 representing the face that is in the vertical direction of the crack and the second subscript 3 representing the axes of x_1, x_2 and x_3, as shown in Figure 3.6. ν_i is the crack opening displacement function with i direction. The cohesive stress and the displacement function at the crack face are given by

$$\sigma_{33}(\bar{r}) = \frac{K_I}{\sqrt{2\pi\bar{r}}}, \qquad \nu_3(\bar{r}) = 4\sqrt{\frac{2\bar{r}}{\pi}}\frac{K_I}{E'} \tag{3.45}$$

Further details regarding the stress and displacement at the crack face can be referred to in Broek (1986), where $E' = E$ for the plane stress, and $E' = E/(1-\nu^2)$ for the plane strain; E and ν are the Young's modulus and Poisson's ratio of the material, respectively; $\bar{r}$ is the distance from the crack front; and ϕ is the angle created between the direction of r and the normal direction of the crack front, as shown in Figure 3.6. Substituting the stress and displacement into Eq. (3.44) gives

$$\Delta G_I = \int_{\theta_1}^{\theta_2}\int_{0}^{\Delta} \frac{K_I}{\sqrt{2\pi r cos\phi}} 2\sqrt{\frac{2(\Delta - r)cos\phi}{\pi}}\frac{K_I}{E'}(R+r)drd\theta \tag{3.46}$$

Thus, Eq. (3.46) can be expressed in terms of the SIFs of the areas of S_1 and S_2, as shown in Figure 3.6, by

$$G_I = \frac{K_I^2}{E'} = \frac{1}{2\left[S_1 - \frac{1}{4}(S_1 - S_2)\right]}\sum_{i=1}^{5} u_i^3 f_i^3 \tag{3.47}$$

Further details of the derivation can be referred to in Okada et al. (2005).

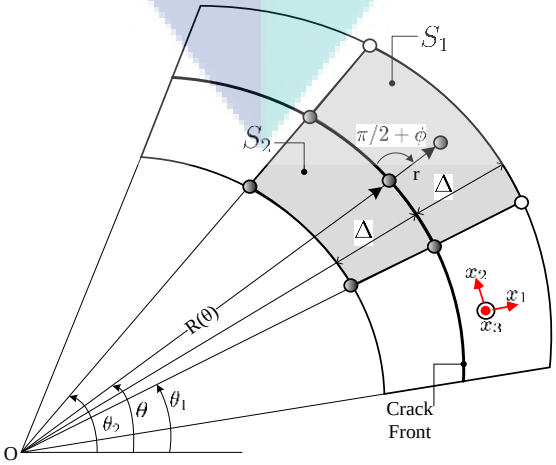

Figure 3.6 Element arrangement at the crack front

The energy release rate for the remaining failure modes are expressed by

$$G_{II} = \frac{K_{II}^2}{E'} = \frac{1}{2\left[S_1 - \frac{1}{4}(S_1 - S_2)\right]} \sum_{i=1}^{5} u_i^1 f_i^1 \tag{3.48}$$

$$G_{III} = \frac{K_{III}^2}{2\mu} = \frac{1}{2\left[S_1 - \frac{1}{4}(S_1 - S_2)\right]} \sum_{i=1}^{5} u_i^2 f_i^2 \tag{3.49}$$

The superscripts at *u* and *f* are the coordinate axes in Figure 3.5, where μ is the shear modulus. Each component of the energy release rate is represented by a subscript at *G*, whereby the sum of G_I, G_{II} and G_{III} produces G_{Total}. The energy release rate can be converted to the SIF, as shown in Equations (3.47), (3.48) and (3.49). The SIF is essential to determine the crack growth rate. The model for fatigue crack growth is explained in the following subsection.

3.4.3 Fatigue Crack Growth Model

Paris' law was implemented to compute the crack growth rate in the ProbS-FEM. Since this research is a pioneer work for the embedded probabilistic approach in the S-FEM, thus an established model such as Paris' law was used for this case. The results of the ProbS-FEM were verified against those by previous researchers who used Paris' law. Therefore, the ProbS-FEM maintained the usage of the same law for the sake of similarity. In addition, Paris' law is simpler and requires fewer parameters. Thus, more effort could be focused on the development of a probabilistic analysis. The result of the SIF calculation was computed as a parameter in the fatigue model. Therefore, the simplest model was selected to reduce and control the uncertainty in the parameters of the fatigue model.

Paris' law is described by the equation

$$\frac{da}{dN_l} = C(\Delta K_{eq})^n \quad or \quad \frac{dc}{dN_l} = C(\Delta K_{eq})^n \tag{3.50}$$

where a, c and N_l are the crack depth, crack length and number of cycles, respectively, while the C and n coefficients are the material constants. The fatigue cycle range is expressed by

$$dN_l = \frac{da_a}{C(\Delta K_{eq})^n} \quad or \quad dN_l = \frac{da_c}{C(\Delta K_{eq})^n} \tag{3.51}$$

The value of ΔK_{eq} is the parameter associated with the fatigue crack growth rate under mixed mode conditions. The equivalent SIF of ΔK_{eq} was used in this study based on Richard's criterion (Richard et al., 2005) . ΔK_{eq} is expressed by

$$\Delta K_{eq} = \frac{\Delta K_I}{2} + \frac{1}{2}\sqrt{\Delta K_I^2 + 4\left(1.155\Delta K_{II}\right)^2 + 4\left(\Delta K_{III}\right)^2} \tag{3.52}$$

Furthermore, the crack growth angle, φ_o was calculated according to the criteria proposed by Richard et al. (2005).

$$\varphi_o = \mp\left[140^o \frac{|\,K_{II}\,|}{K_I + |\,K_{II}\,| + |\,K_{III}\,|} - 70^o\left(\frac{|\,K_{II}\,|}{K_I + |\,K_{II}\,| + |\,K_{III}\,|}\right)^2\right] \tag{3.53}$$

where $\varphi_o < 0^o$ for $K_{II} > 0$ and $\varphi_o > 0^o$ for $K_{II} < 0$ and $K_I \geq 0$. The crack growth angle, φ_o is shown in Figure 3.7. The calculation of the number of cycles and the explanation on the crack direction marked the end of the deterministic analysis. The deterministic analysis was merged with the probabilistic analysis. The implementation of the probabilistic analysis is explained in the next section.

3.5 PROBABILISTIC S-VERSION FINITE ELEMENT MODEL

The ProbS-FEM that was developed in this study consisted of an uncertainty analysis of the complex mathematical models of risk or failure. If each of the random parameters is characterised by a probability density function (PDF), then a joint PDF, $f_X(X)$ is produced. Therefore, the probability of failure (POF), P_f is given by

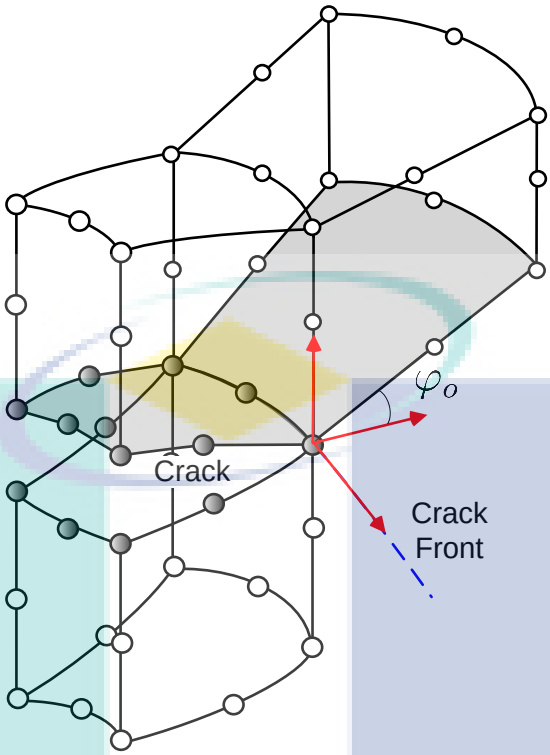

Figure 3.7 Crack growth direction

$$P_f = \int_{g(X)<0} f_X(X)dX \tag{3.54}$$

where X is the vector that represents the independent random parameter, and $g(X)$ is the performance function. If $g(X) < 0$, it indicates failure. Since the evaluation of Eq. (3.54) is difficult as $g(X)$ and $f_x(X)$ are non-linear and multidimensional (Chowdhury et al., 2014), therefore, the Monte Carlo simulation (MCS) was used in the ProbS-FEM to avoid the integration in Eq. (3.54).

The MCS is used to provide a distribution on final outputs. The method can account for parameter uncertainty in a rational way. The Monte Carlo method was used to account for parameter uncertainty in the ProbS-FEM. The technique for accounting for parameter uncertainty consists of the following steps:

(i) Sampling of random parameters

(ii) Generating data from the selected distribution

(iii) Using the generated data as a parameter in the model to produce the output

(iv) Extracting the probabilistic information

These steps will be presented in turn.

3.5.1 Sampling of Random Parameters

Modern computer programs have the capability of generating uniformly distributed random numbers from zero until one. By utilising this capability, a random number is generated from different numbers of seed values. A seed value is the starting point from which to grow a formula. Different seed values are generated for different sets of random numbers.

In the initial step of the sampling process, a random number was picked. Different random numbers were generated for different parameters. It was a continuous process as the new sample was generated. The generation of loops was continued until the end of the sample. Once the random number had been picked, the inverse transformation technique was used for generating a random parameter from the selected distribution. The generation of random parameters is explained in Section 3.5.2.

3.5.2 Generating Data from the Selected Distribution

The type of distribution for each parameter was determined based on the experimental result or the citation from the paper of a previous researcher (Liu & Mahadevan, 2009). The next task was to equate the generated random number, q_i with the selected cumulative distribution function (CDF), $F_X(x_i)$ of the random parameter, x_i. The equation for this is shown as

$$q_i = F_X(x_i) = \Phi\left(\frac{x_i - \mu_X}{\sigma_X}\right) \tag{3.55}$$

where μ_X and σ_X are the mean and standard deviation of the random parameter, respectively. Thus, the random parameter yields

$$x_i = \mu_X + \sigma_X \Phi^{-1}(q_i) \tag{3.56}$$

where Φ^{-1} is the inverse of the selected CDF of each random parameter. Figure 3.8 shows the transformation of the random number to a random parameter. The random parameters that were generated were computed to enable the ProbS-FEM to produce outputs. The generation of outputs is explained in the following subsection.

3.5.3 Producing the Outputs

The generated random parameters were fed into the finite element model and the associated results were calculated. Once the new sample had been computed, a new sampling process began again. The entire finite element calculation process was repeated by using newly generated data. After all the samples had been generated, the probabilistic information was extracted. Since each sample produced its own output, the outputs were compiled for the extraction of the probabilistic information. The extraction process is explained below.

3.5.4 Extracting the Probabilistic Information

The sampling process produced a huge dataset from which the probabilistic information was extracted. The available information was with regard to the probability of failure, the upper and lower bounds, the determination of the probability distribution and the regression analysis. The information is discussed in the following subsections.

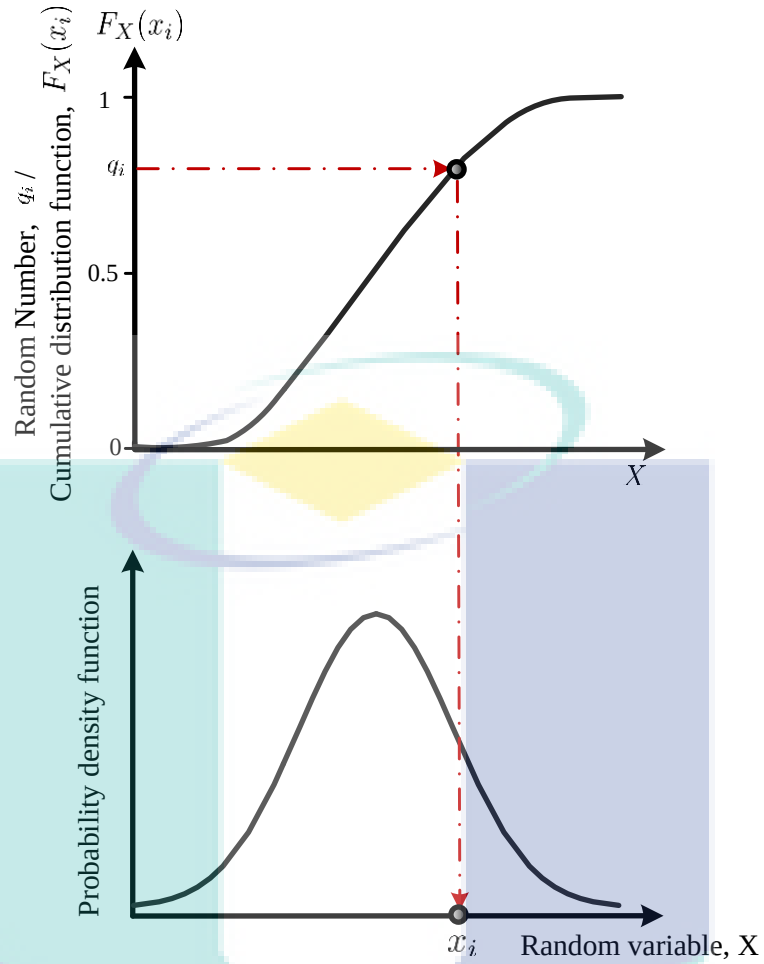

Figure 3.8 Mapping for data generation

a. Probability of Failure (POF)

The probabilistic information was extracted from an evaluation of the performance function, $g(X)$, which is given by

$$g(X) = K_{Ic} - \triangle K_{eq}(X) \tag{3.57}$$

where K_{Ic} is the fracture toughness and $\triangle K_{eq}$ is the equivalent of the SIF. The vector X represents all the random parameters such as the initial crack size, material properties and load. Since the equivalent of the SIF was a function of the vector X, the crack growth rate was computed probabilistically. Based on Eq. (3.51), the mean of the cycle can be expressed as

$$E[dN_l] = \frac{E[da_{max}]}{E[C](E[\Delta K_{eq_{max}}])^n} \tag{3.58}$$

where $E[\cdot]$ is the mean operator. Since ΔK_{eqmax} is the dependent parameter, the predetermined value of ΔK_{eqmax} was used in this case. The predetermined ΔK_{eqmax} was computed through S-FEM iteration via Eq. (3.52) with regard to the randomness of the Young's modulus, yield strength, initial crack length and depth. The uncertainties in the predetermined $\Delta K_{eq_{max}}$ implicitly influenced the fatigue life calculation. Once the distribution of ΔK_{eqmax} was computed, the mean of the cycle could be solved.

The maximum increment in the crack growth was used to calculate the remaining crack length at the nodes on the crack front. The maximum increment in the crack growth was located at the node that computed the maximum equivalent SIF. Then, dN_l was calculated using Eq. (3.51), and was then used to compute the remaining crack length or depth at the nodes. After calculating the crack lengths of the remaining nodes, a new crack front was constructed. The construction of the new crack front is shown in Figure 3.9. The construction of the crack length at each node showed that every crack length was exposed to uncertainty because of the dependence on the random parameter, da_{max}.

Thus, the randomness in the crack shape was due to the randomness of the independent and dependent parameters in Eq. (3.58). The process continued with the looping generation of the random variable for the next sample until the final sample was completed. Then, the statistical results were obtained from the compilation of all the samples. From the statistical results, the distribution of the crack shape, crack length or depth versus cycles, and the SIF were constructed.

Besides the quantification of the POF, the compilation of the failure and non-failure samples was used for this purpose. Let N_t be the total number of samples and N_f the total number of samples when $g(X) < 0$. Thus, the POF was estimated by

$$P_f = \frac{N_f}{N_t} \tag{3.59}$$

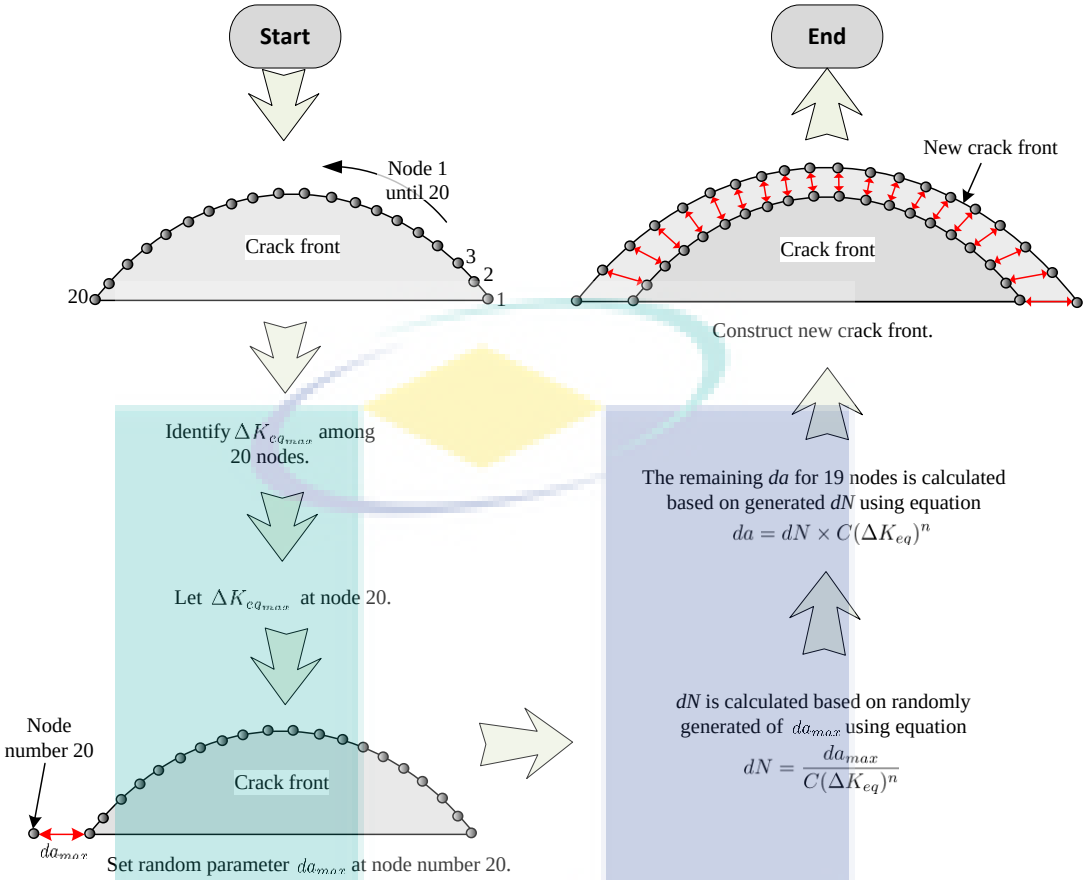

Figure 3.9 Construction of new crack front

b. Bounds

The upper bound, lower bound and the 95% confidence bound can be generated in the ProbS-FEM. After all the results had been computed by the ProbS-FEM, the mean of the results was calculated. The maximum result was denoted as the upper bound and the minimum result was assigned as the lower bound. In addition, the confidence bounds of the probabilistic information were constructed from the ProbS-FEM results. Occasionally, the confidence bound is also known as the confidence level. The confidence bound of the result was calculated based on the mean of the ProbS-FEM. The percentage depends on the desired confidence bound. A 95% confidence bound is a plausible figure to rely on. It was reasonable that 95% of the results were within a certain range of distribution. The fatigue strength and life can be calculated at a 95% confidence bound due to its convenience and simplicity for application in fatigue analysis. For instance, aircraft structural designs use a 95% confidence level (Huang et

al., 2012). The wider the confidence bound, the more certain it will be that all the results will be within that range. For example, if the mean of the samples is 100 and the standard deviation of the samples is 15 out of 100 samples, therefore, the corresponding 95% bound would be $+2.9$. The 95% bound was calculated using the equation below:

$$Bounds_{95\%} = \bar{\mu_X} \pm \frac{1.96\bar{\sigma_X}}{\sqrt{N_t}} \tag{3.60}$$

where $\bar{\mu_X}$ is the mean of the samples, $\bar{\sigma_X}$ is the standard deviation of the samples and $N_t$is the total number of samples. In this case, there was a 95% certainty that the true mean of the population fell within the range of 97.1 to 102.9.

c. Determination of Probability Distribution

Further probabilistic information available from the ProbS-FEM analysis is the crack growth distribution. The type of probability distribution is determined via a statistical test. Through this statistical test, a judgement needs to be made as to whether the relationship between the random variable (such as crack growth) and its CDF is close to linear.

In order to establish the underlying distribution, two commonly used statistical tests for this purpose are the chi-square and the Kolmogorov-Smirnov (K-S) test. The K-S test was used in this research because of its advantage over the chi-square test in that, with the former, the data does not have to be divided into intervals. In this way, the error associated with the number of intervals can be avoided.

The K-S test compares the observed cumulative frequency and the CDF of an assumed theoretical distribution. After arranging the data or random variables in increasing order, the maximum difference between the two cumulative distribution functions of the ordered data can be estimated as

$$D_n = max \mid F_X(x_i) - S_n(x_i) \mid \tag{3.61}$$

where $F_X(x_i)$ is the theoretical CDF of the assumed distribution at the *i*th observation of the ordered data, x_i, and $S_n(x_i)$ is the corresponding stepwise CDF or Empirical Cumulative Distribution Function (ECDF) of the observed ordered data. The ECDF is like an ideal CDF line for the assumed distribution. The ECDF, $S_n(x_i)$ can be estimated as

$$S_n(x_i) = \left\{ \begin{array}{ll} 0, & x < x_1 \\ \frac{m}{n}, & x_m \leq x \leq x_{m+1} \\ 1, & x \geq x_n \end{array} \right\} \tag{3.62}$$

An example, taken from Akramin (2008), is shown in Figure 3.10. The CDF of D_n can be related to the significance level, α as

$$P(D_n \leq D_n^{\alpha} = 1 - \alpha) \tag{3.63}$$

and the D_n^{α} values at various significance levels, α can be obtained from a standard mathematical table, as shown in Haldar & Mahadevan (2000). Then, according to the K-S test, if the maximum difference, D_n is less than or equal to the tabulated value, D_n^{α}, the assumed distribution is acceptable at the significance level, α. A further explanation regarding the K-S test can be referred to in the study by Mora-López & Mora (2015).

d. Regression Analysis

Regression analysis is a statistical tool that measures the relationships between variables. The analysis produces regression coefficients and determines how well the regression line explains the variations of the dependent variable. The coefficient of determination, R^2 represents the ratio or percentage of the data that is closest to the regression line. Further details regarding this analysis can be referred to in Freedman (2009).

The POF, bounds, determination of the distribution, and regression analysis can be extracted from the ProbS-FEM results. The calculation of the POF and the bounds of the probabilistic information required a huge number of samples for the sake of convergence. Therefore, an enhancement of the sampling strategy was required in the ProbS-FEM to reduce the analysis time. Various techniques have been implemented in engineering applications, and one of these techniques is the LHS. The following section explains the LHS technique.

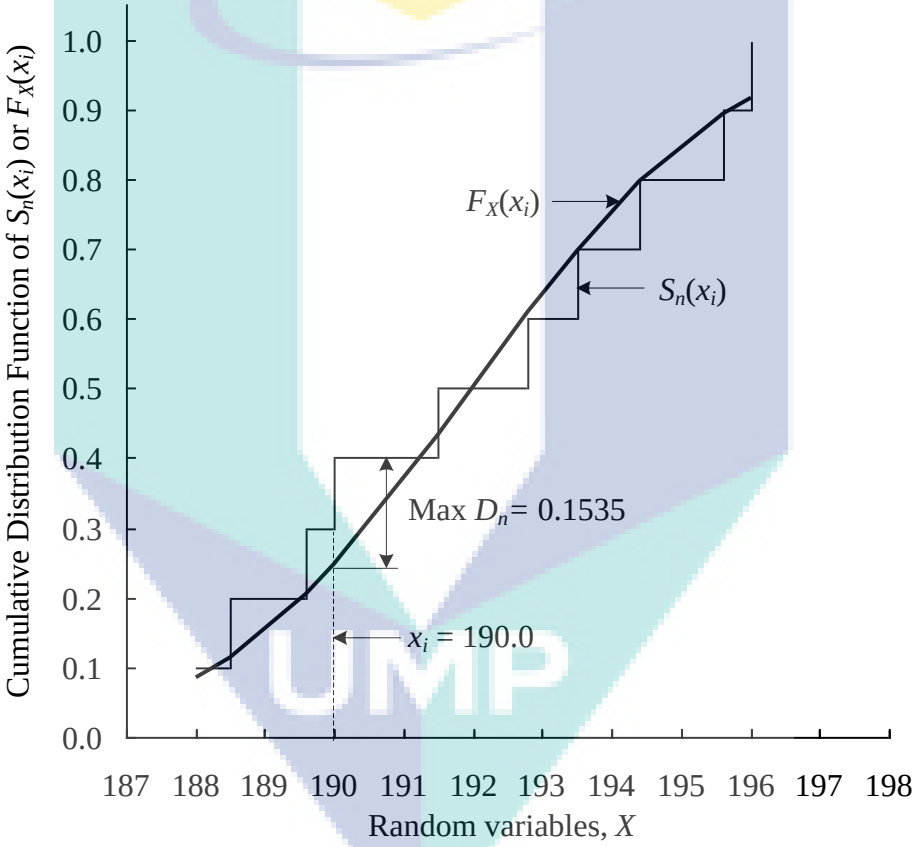

Figure 3.10 An example of the K-S test for ten random variables

Source: Akramin (2008)

3.6 LATIN HYPERCUBE SAMPLING

The sampling of random parameters for the MCS was explained in Section 3.5.1. The MCS randomly generates a number according to a certain distribution. The procedure is repeated for the next sample. It is impossible for the MCS to generate the same

number if the random number has four or five decimal places. However, the MCS might generate a random number that is nearly the same as previous samples due to the lack of memory of past random numbers. As a result, the MCS might generate denser random numbers within a certain range and not in other ranges, as shown in Figure 3.11(a). A large number of samples are required to produce rare extreme random numbers. A major issue in the generation of more samples is the time constraint since the whole analysis needs to be repeated. Therefore, a good sampling strategy was required to overcome this problem.

The sampling strategy was improved using the LHS. The LHS provides a constrained sampling strategy instead of random sampling according to the MCS. The LHS strategy was used to limit the possible samples by ensuring that all parts of the distribution were represented in the sample. In the LHS, the regions 0 and 1 were uniformly divided into N_t non-overlapping portions. For instance, Figure 3.11(b) shows a range of random numbers divided into seven portions. Then, one random number per portion was generated. This means that N_t random numbers were generated for each random variable. Normally, the value of N_t is equated to the number of simulation cycles. This is because the number of simulation cycles determines the number of trials. N_t times the number of simulation cycles gives N_t times of trials. Since the simulation was generated for N_t times of trials, then the distribution was divided into N_t non-overlapping portions. Therefore, N_t random numbers were generated for N_t non-overlapping portions. In other words, one random number per portion was computed.

The generated values within the range [0,1] were linearly transformed to the random numbers in the non-overlapping portions using following equation

$$q_p = \frac{q}{N_t} + \frac{(p-1)}{N_t} \tag{3.64}$$

where p is the pth portion from 1,2,3,….N_t; q is a random number within the range [0,1]; and q_p is a random number in the pth portion. Based on Eq. (3.64), only one generated value was randomly selected for each portion. The lower and upper bounds

of the pth portion prevented any out of bounds selection. The lower and upper bounds were calculated as

$$\frac{(p-1)}{N_t} < q_p < \frac{p}{N_t} \tag{3.65}$$

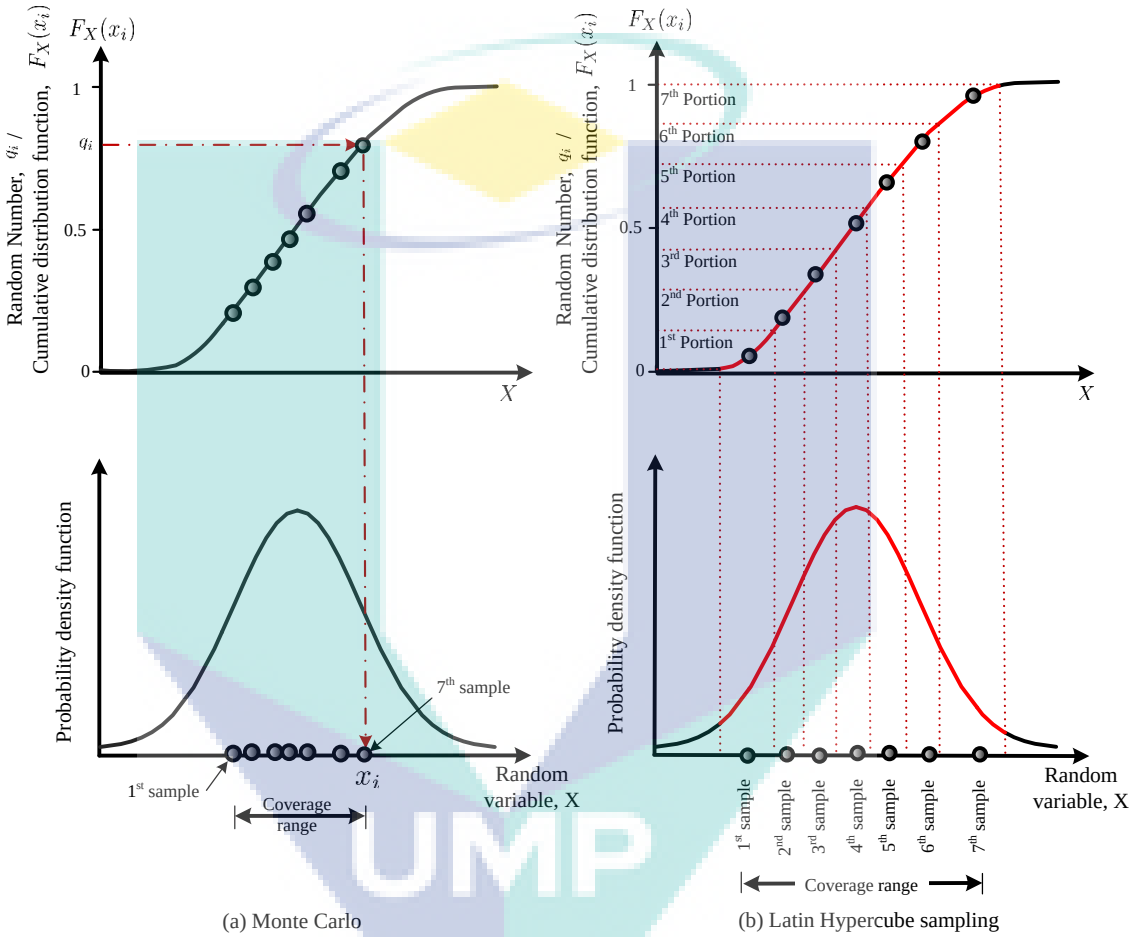

Figure 3.11 Coverage of range of distribution for MCS and LHS

The generation was continued until the end of the number of simulation cycles. All the random numbers were distributed into each portion. A denser generation at a certain portion was avoided. The LHS strategy covered all parts of the distribution with a minimum number of samples. By covering all parts of the distribution, the efficiency of the simulation was increased.

After the random parameters had been generated from the selected distribution, the simulation was continued with the analysing and producing outputs. The same process was implemented in the MCS, as explained in Sections 3.5.2 to 3.5.4. Figure 3.12 shows the flow for the MCS and LHS processes. After all the ProbS-FEM analyses had been carried out with the LHS, the few outcomes were verified by the experimental results. The experimental setup is presented as below.

3.7 EXPERIMENTAL SETUP

Experimental works were carried out on certain specimens due to the feasibility of the apparatus and the significance of the verification. Three- and four-point bending specimens were prepared for this research work. This was a non-standard experiment as the objective of conducting the experiment was to obtain the crack growth for surface cracks in a bending load. The closest standard experiment is the ASTM E740-03 (2008) for surface crack tension specimens. Based on the ASTM E740-03 (2008), the surface crack test is suitable for direct application to designs only when the service conditions are exactly parallel to the test conditions. Since the test conditions were in tension mode, the ASTM E740-03 was not applicable for the bending condition. Therefore, a non-standard experiment was conducted, and this is explained in the following subsection, which consists of the specimen preparation and the experimental procedure.

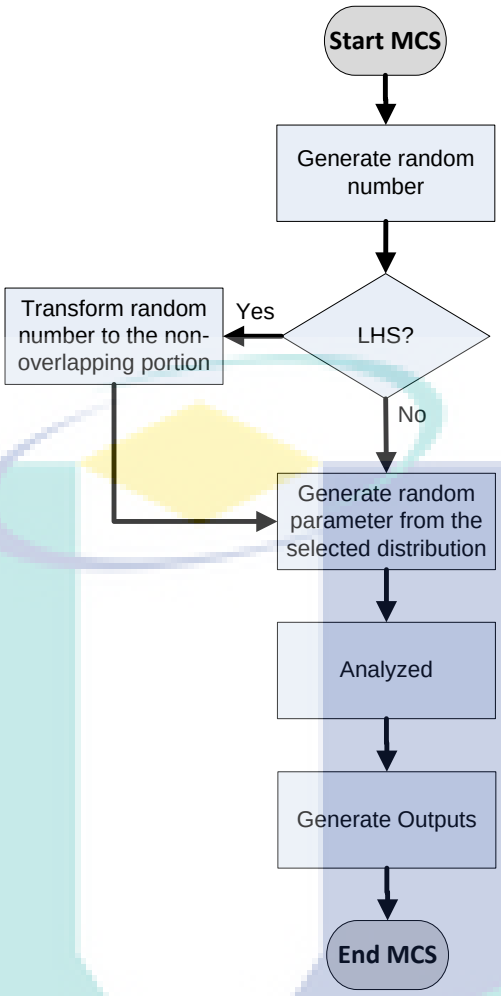

Figure 3.12 Flow of the MCS and LHS processes

3.7.1 Specimen Preparation

The material used in the experiment was Aluminium 7075-T6. The reason for choosing Aluminium 7075-T6 was that the material is used for applications that are exposed to fatigue such an aging aircraft (Sankaran et al., 2001). The chemical composition of the material includes Zn (5.6 wt%), Mg (2.5 wt%), Cu (1.6 wt%) and Cr (0.3 wt%) (Ohdama, 2012). The specimens were prepared in a long traverse (LT) direction.

A flat work piece with a protuberance was prepared, as shown in Figure 3.13. The size of the work piece varied as the crack angle was varied from 0° to 45°. An electric wire-cutting machine was used to introduce a notch with a diameter of 0.2 mm. The notch was located at the centre of the protuberance. The work piece was then

polished to a mirror finish at the vicinity of the crack length. In order to introduce an initial surface crack, a cyclic load was applied to the work piece, as shown in Figure 3.14.

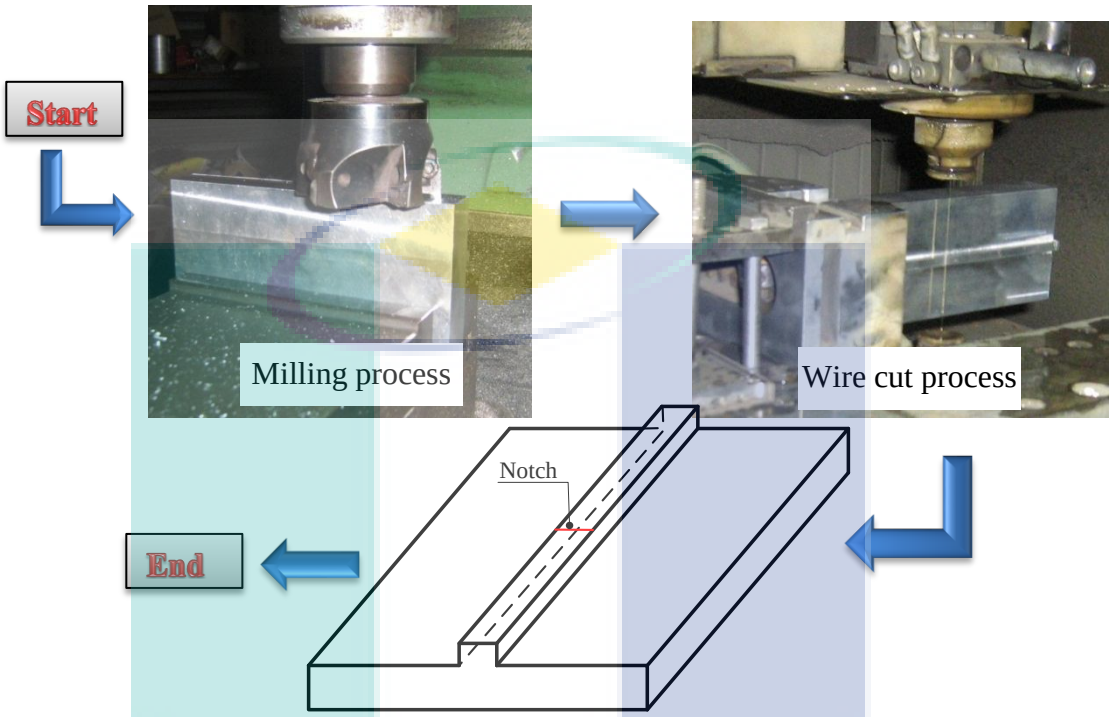

Figure 3.13 Preparation of work piece with protuberance

A four-point bending setup was prepared for the work piece with the protuberance at the bottom. The schematic figure of the four-point bending setup is shown in Figure 3.15. The four-point bending test was used as a larger area of the work piece was exposed to potential defects and flaws. The introduction of the initial surface crack was conducted with a 100-kN capacity MTS servo-hydraulic machine operating in a load control mode. The stress ratio was set to 0.1 with a frequency of 20 Hertz. The stress ratio of 0.1 is frequently used when testing components and to gain the maximum crack opening displacement during the fatigue loading. The maximum and minimum loads were 45 kN and 4.5 kN, respectively. The maximum load was computed based on the fatigue endurance limit of the Aluminium 7075-T6 material (Liu & Mahadevan, 2009). Thus, 45 kN was the usable maximum load for the work piece. The upper test rig applied the load, while the lower test rig remained static. Once the load was released, the work piece was subjected to the bending load.

The notch at the bottom was forced to grow the crack. As the loading and unloading processes were repeated, the surface crack was established, as shown in Figure 3.16.

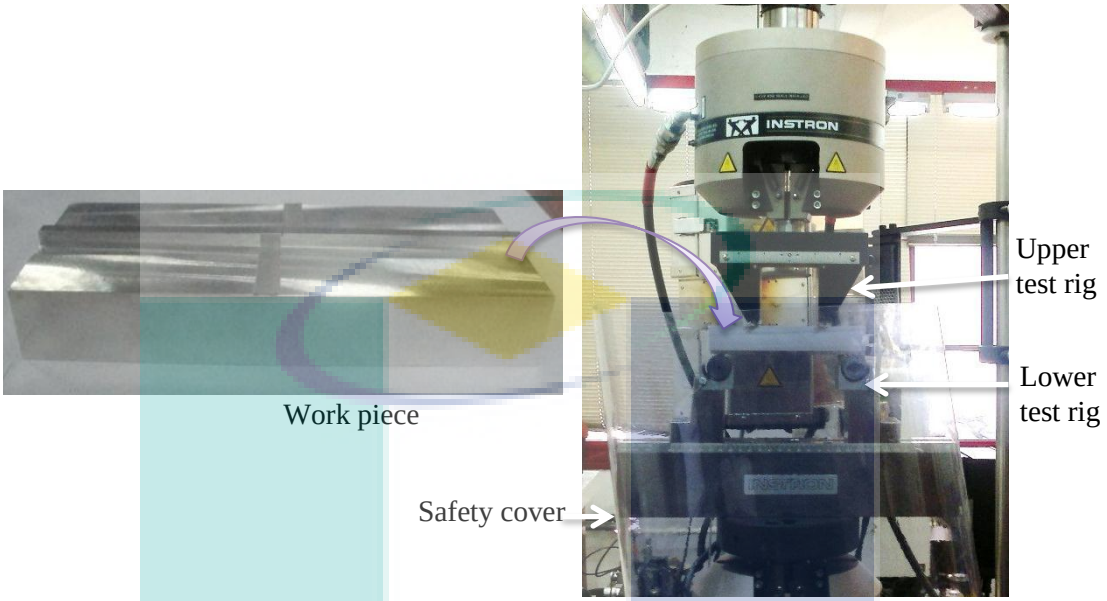

Figure 3.14 Introduction to the initial surface crack

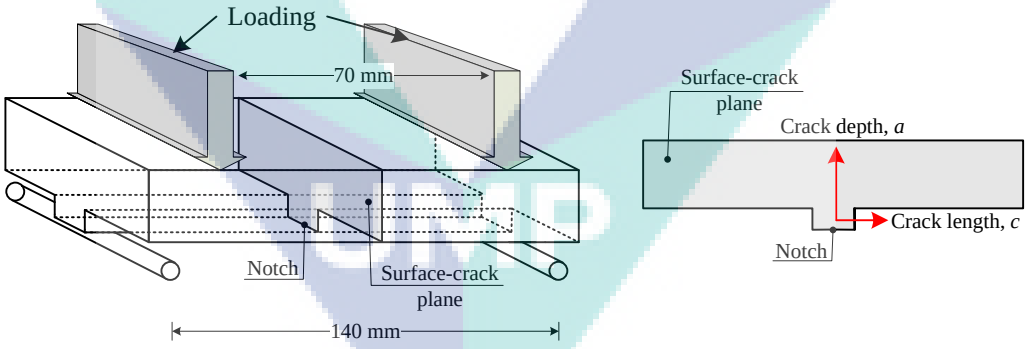

Figure 3.15 Schematic figure of initial surface crack setup

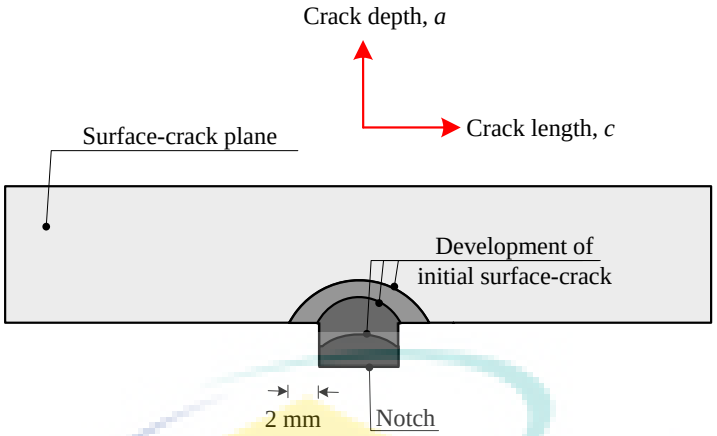

Figure 3.16 Initial surface crack growth

In order to create the initial surface crack, the cyclic load was stopped when the crack length grew to 2 mm from the protuberance. Then, the protuberance was milled off and the deeper surface crack remained in the work piece. The process is shown in Figure 3.17. The remaining surface crack was treated as an initial crack in the specimen later on.

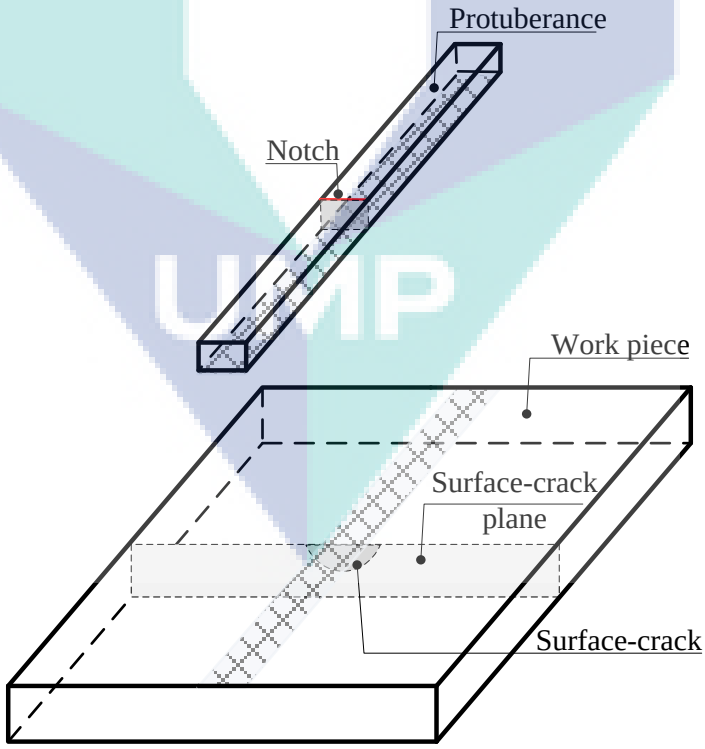

Figure 3.17 Surface crack remained in the work piece and the protuberance milled off

Then, a 160×65×25 mm specimen was prepared from the work piece. In order to prepare a slanted surface crack specimen, it was necessary to cut the work piece at a certain angle using a band saw machine, as shown in Figure 3.18. The crack angle, α was varied from 0° until 45°, as shown in Figure 3.19. The size of the work piece became larger as the crack angle was increased to 45° in order to prepare the specimen to have the same dimensions of 160×65×25 mm.

The vicinity of the crack length at the specimen was polished to a mirror finish. The specimen was then ready for the fatigue test. The experimental procedure for the fatigue test is explained in the next subsection.

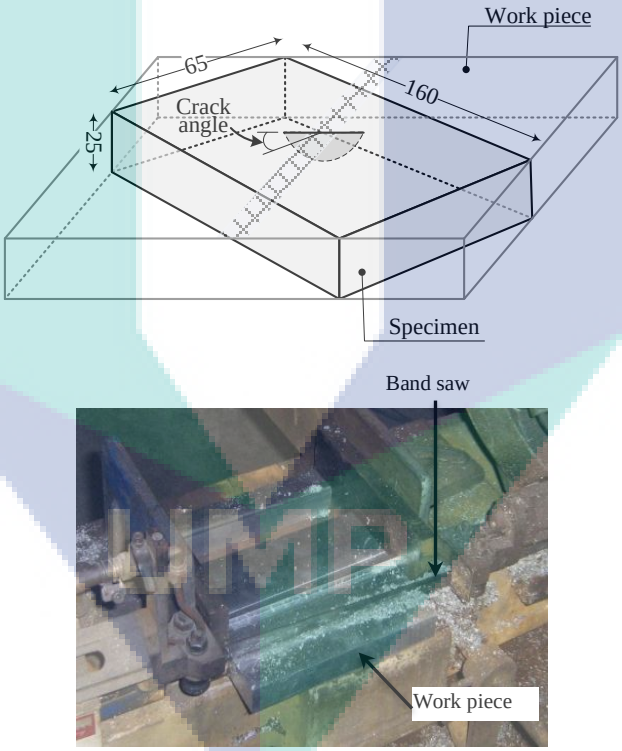

Figure 3.18 Specimen prepared from a work piece using a band saw machine

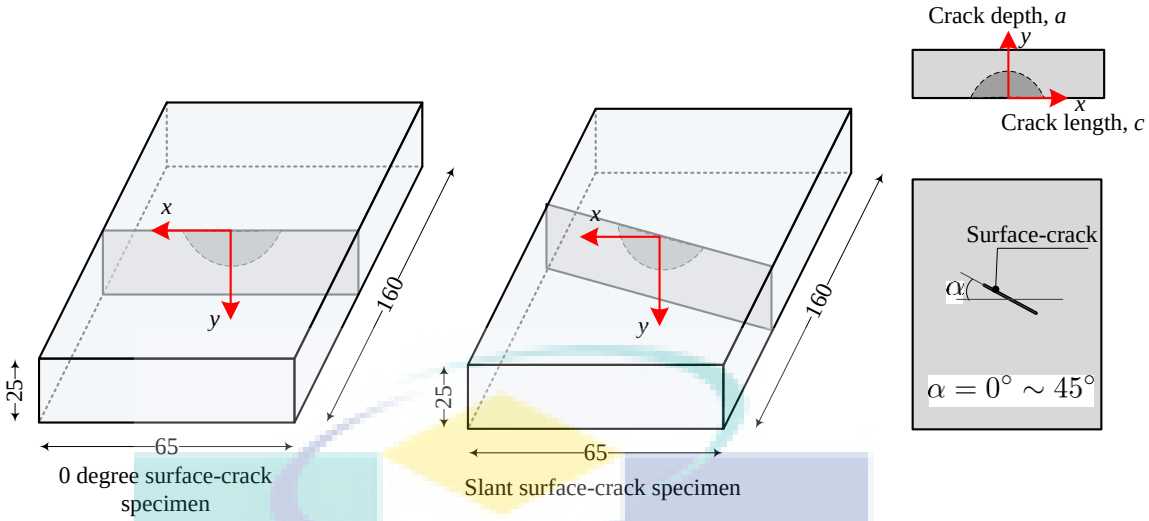

Figure 3.19 0° surface crack and slanted surface crack specimens

3.7.2 Experimental Procedure

A four-point bending fatigue test was conducted using a dynamic system from Instron®. The 8801 servo-hydraulic fatigue-testing machine is capable of performing a fatigue test with a load of up to 100 kN, and it varies in both a dynamic and static testing environment. It is a fully-digital servo-hydraulic controller that is able to provide an automatic calibration of all the compatible transducers. The console software is used as an interface for the controller. The calibration of a transducer requires a few steps in the interface. When the load cell or extensometer is changed, the controller automatically recognizes its characteristics and prevents it from starting a test until the calibration has been computed. The force amplitude is calibrated using a strain gauge load cell.

The mechanical system of the 8801 servo-hydraulic testing system consists of advanced features such as the Software®Bluehil for static tests and the WaveMatrix™ for cyclic block loading software. The test was carried out at ambient temperature to ensure that failure due to any unwanted mechanism would be avoided. Since the objective of this research was to investigate the crack growth of the specimen under a fatigue load, a wider surface crack plane in the specimen was needed. Thus, a non-

standard test was conducted. A wider surface crack plane was provided in the specimen to enable the crack to grow.

In a previous study (Kikuchi, Maitireymu, et al., 2010), the frequency was set at 20 Hertz for all experimental conditions. Due to the significance of plastic strain, the maximum usable frequency was set at 20 Hertz (El-Zeghayar et al., 2011). As shown in Figure 3.20, the specimen was located at the centre of the rigs. The upper and lower rigs could be adjusted according to the geometry of the specimen. The length for the lower rig was 140 mm and that for the upper rig was 70 mm. It should be noted that the upper rig position and length were meant to replicate the four-point bending test. Therefore, the measurements were according to the study by Kikuchi et al. (2010). The specimen was positioned in the middle of the test rig, with the surface crack facing the lower test rig. Once the specimen had been placed according to the required specifications, the lower rig was slowly adjusted until the force transducer showed the value zero or close to zero. This was to ensure that the specimen was fixed and that the loading could be transferred directly to the specimen.

The entire experimental process was conducted continuously via the automatic settings in the WaveMatrix™ that allowed the user to set the loading history. The Instron servo-hydraulic testing machine is equipped with many accessories and sensors to fulfil the needs of researchers. Among them are a transducer for the force and the displacement. The force transducer allows users to monitor and apply the loading. However, if a user would like to perform the experiment using the displacement, then the displacement will replace the force as the input. The WaveMatrix™ also allows users to set the type of motion such as sinusoidal, square or even random motion. In this research, a constant sinusoidal wave was used to replicate the constant amplitude loading.

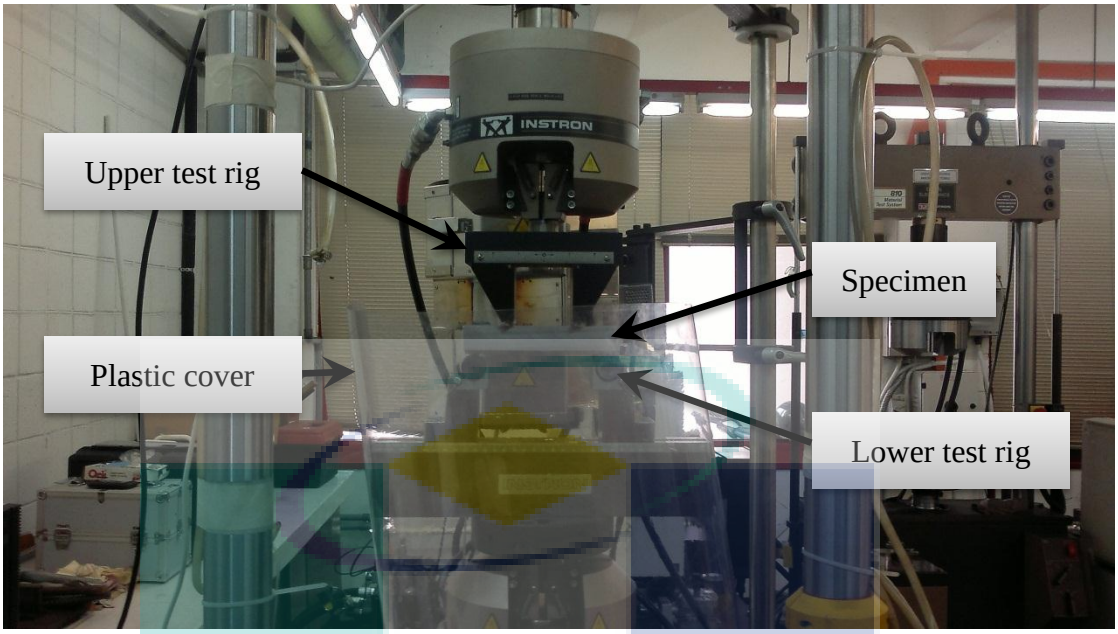

Figure 3.20 Specimen positioned in the middle of the upper and lower test rigs

Subsequently, the WaveMatrix™ software was used to set up the loading history of the experiment, as shown in Figure 3.21. The user-friendly graphic interface made it easier for the tester to use the software and to design the loading. Using a maximum stress (*Fmax*) set at 45 kN, the loading history was then designed following the stress ratio (*R*) of 0.1 for the crack propagation and 0.8 for the beach marks. By having a maximum load of 45 kN and using 0.1 as the stress ratio, the minimum load would then be 4.5 kN, and the mean stress was calculated to be 24.75 kN. Figure 3.21 shows the loading history that was designed in order to produce the beach marks, and this sequence was repeated. The stress ratios of 0.1 and 0.8 were conducted for up to 20,000 cycles and 100,000 cycles, respectively. The fatigue test was stopped when the specimen failed, i.e. in this case, broke into two pieces. The complete experimental process is shown in Figure 3.22.

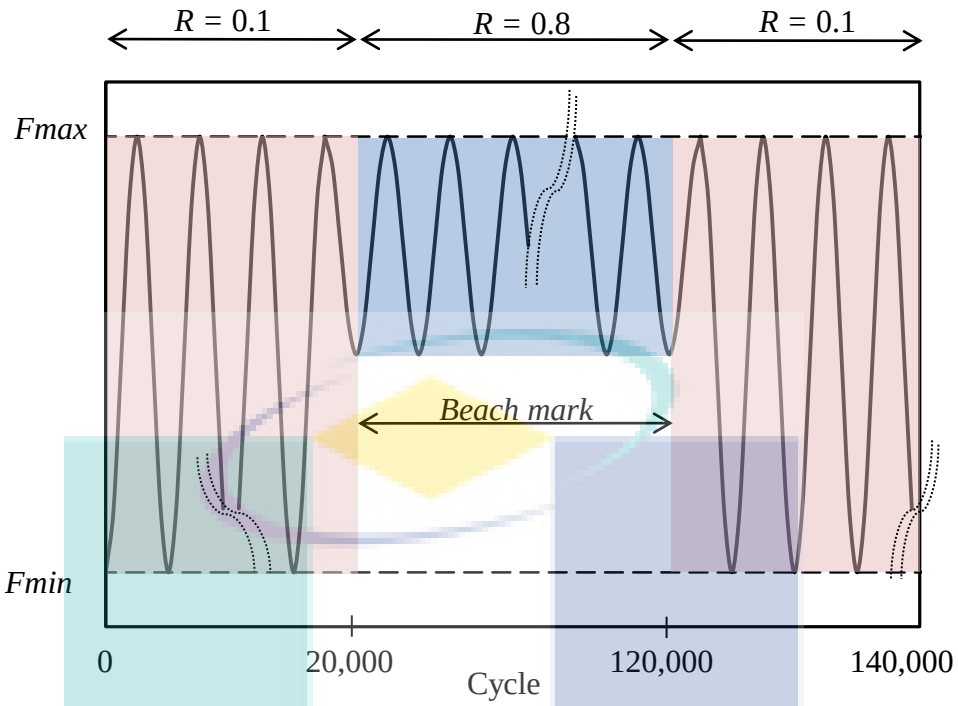

Figure 3.21 Amplitude of cyclic loading

Since two different stress ratios were computed, two different fracture surfaces were developed, as shown in Figure 3.23. The reason why the beach mark phenomenon was introduced was to allow the crack length, *c* and the crack depth, *a* to be measured. The crack length and crack depth were measured from the distance of two beach marks, as shown in Figure 3.24, as captured using a Baty Vision System - Venture System. The beach marks could be clearly seen and were measured using the Baty precision instruments. Hence, instead of having to monitor the specimen for a number of cycles before taking the measurement, this experimental procedure was much more effective in reducing experimental errors since once the measurements of the specimen had been taken, it had to go through the whole process again, starting from the placement to the assigning of the loading. Thus, the experimental procedure could be questionable since the experiment had to be stopped to remove the specimen for measurement before placing it back to continue with the experiment.

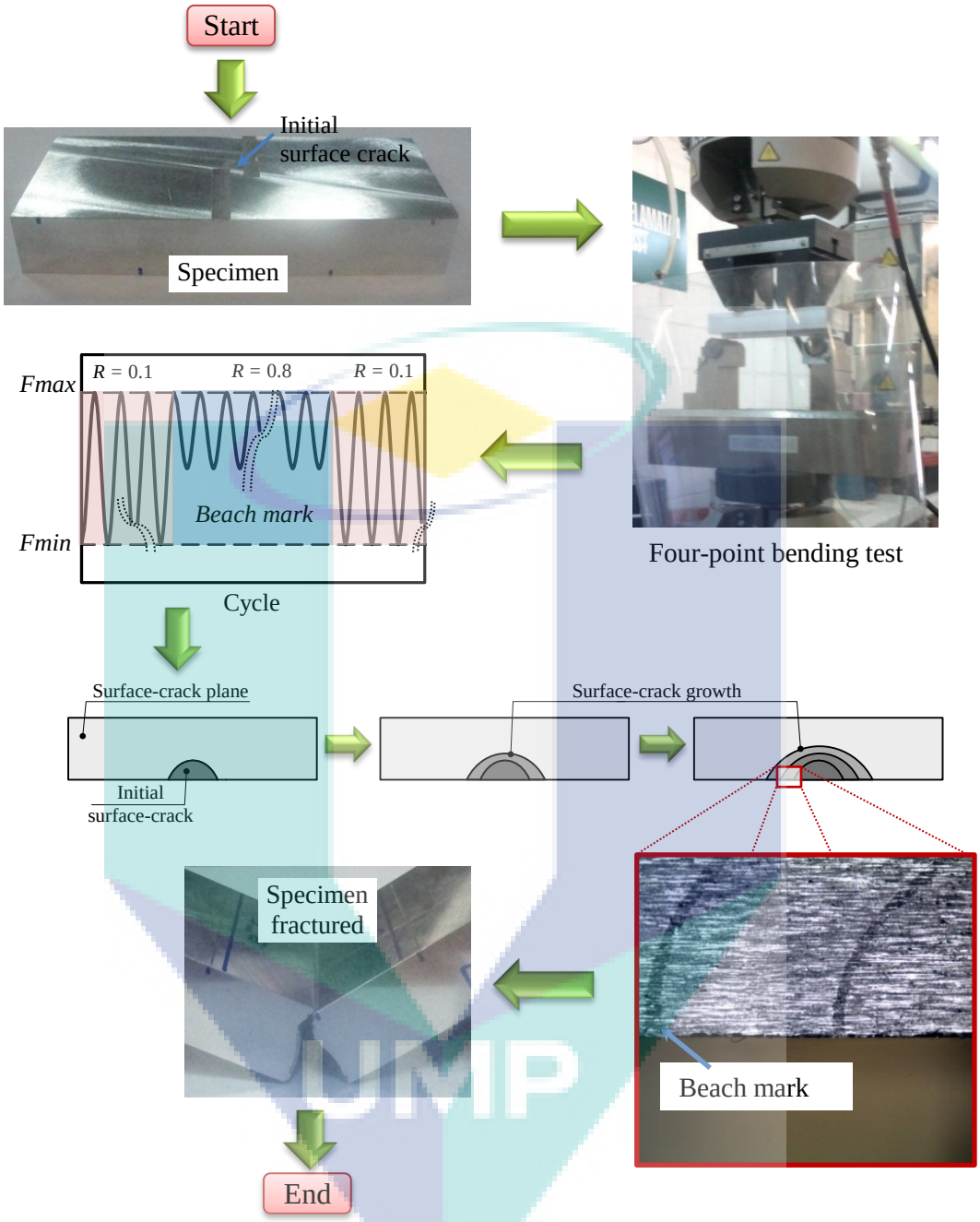

Figure 3.22 Experimental process

Finally, the coordinates were plotted and the number of cycles was calculated. The results were verified by plotting the experimental and ProbS-FEM outcomes in the same graph. The failure cycle was also validated to show the capability of the ProbS-FEM.

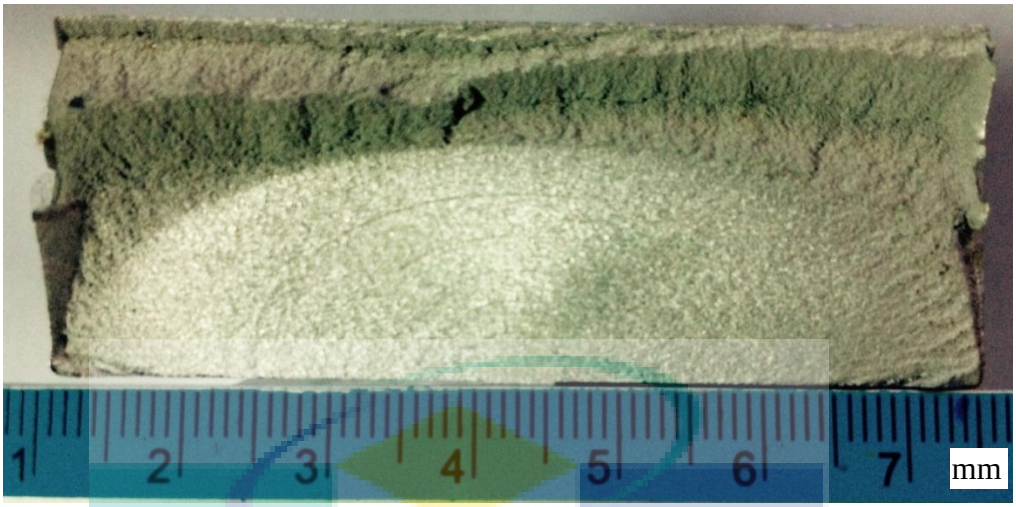

(a)

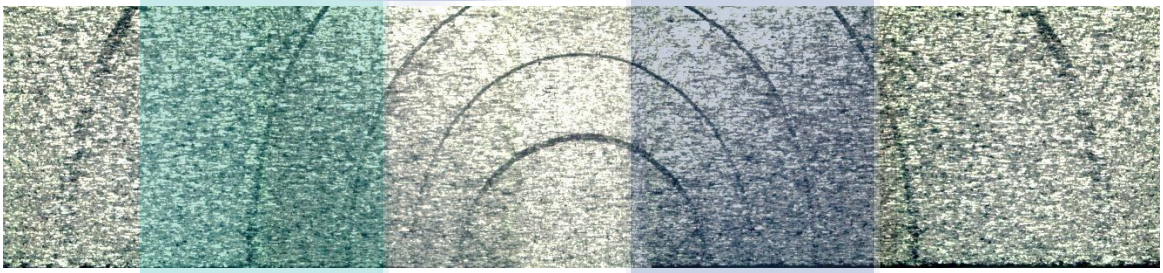

(b)

Figure 3.23 Specimen photo taken by (a) normal camera (b) Baty Vision System - Venture System

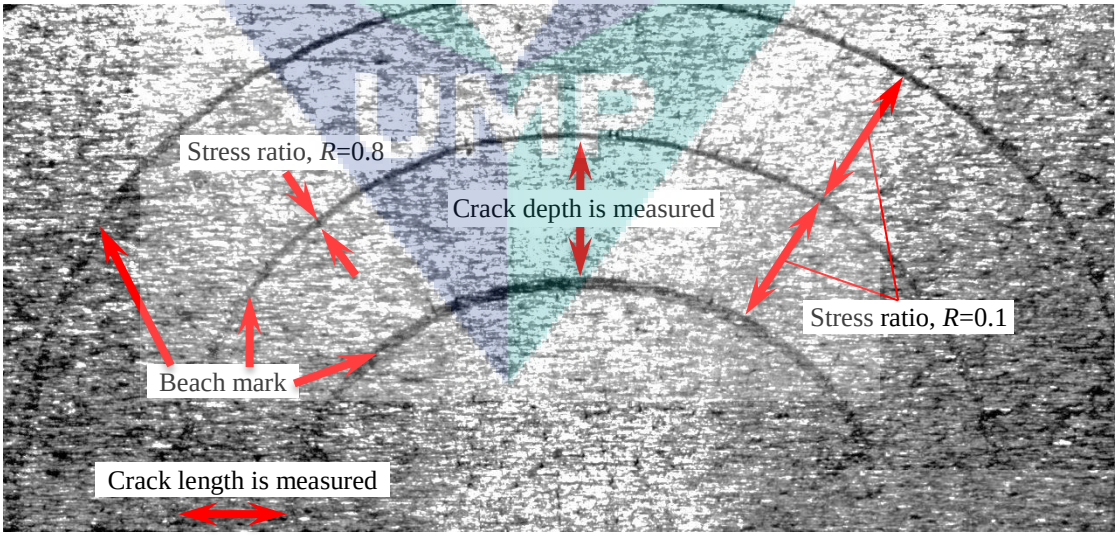

Figure 3.24 Crack length and depth measurement

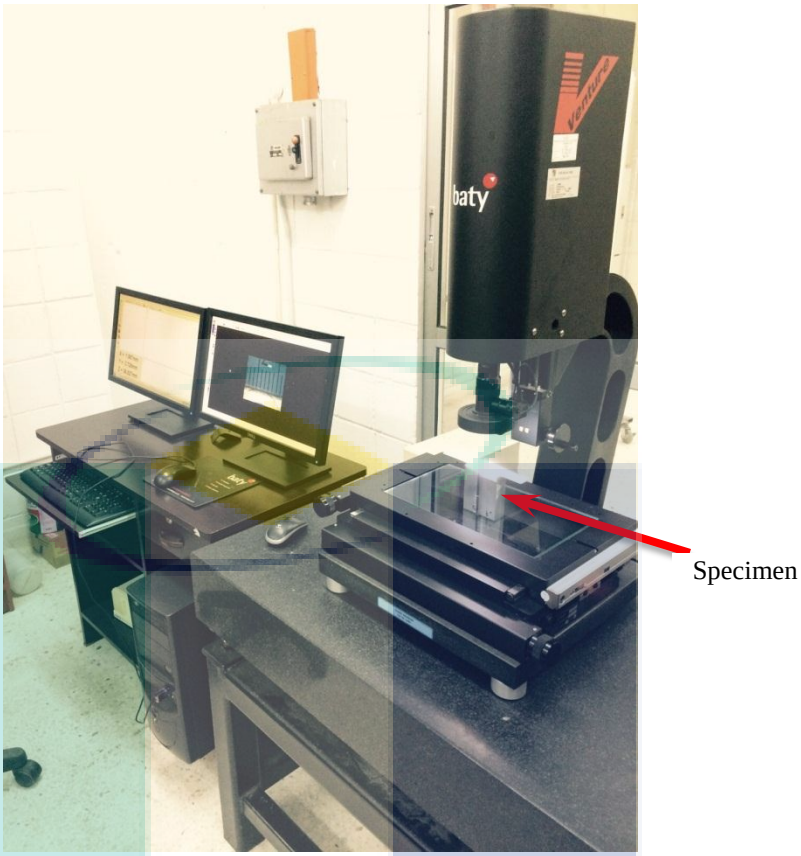

Figure 3.25 The Baty Vision System - Venture System

3.8 SUMMARY

Section 3.1 presented an overview of Chapter 3 with the objective of delivering the ProbS-FEM formulation from the governing equation until the sampling technique of the probabilistic analysis. In order to model the uncertainty, Sections 3.3 and 3.4 addressed the typical understanding of the finite element formulation and the enhancement of the ProbS-FEM finite element model.

The development of a stiffness matrix at the overlaid region was the key point in the development of the ProbS-FEM. The crucial part was the development of the strain displacement matrix $[B]$ and displacement function for two different types of meshes, namely global and local. The $[B^G]$ matrix was constructed by using the integration of the Gauss point coordinates in the local and global elements. The Gauss point coordinates were calculated based on the Newton-Raphson method. Once the $[B^G]$ matrix had been calculated, the stiffness matrix for the global, local and global-

local mesh could be computed. The stiffness matrix was used to calculate the relationship of $\{F\} = [k]\{u\}$. The displacement of each node was calculated based on the relationship and was used for the construction of the stress-strain equation.

Once the stress-strain of the structure had been computed, the analysis was further extended to the calculation of the fatigue crack growth and direction based on Paris's law and Richard's criterion, respectively.

This was followed by the modelling of the uncertainty in the ProbS-FEM using the MCS, with quite a bit of time being taken up for the generation of samples. The LHS was used to reduce the number of samples. This chapter ends with an explanation of the experiment since few results were validated by the experimental findings. The applications and findings of the ProbS-FEM are presented in the following chapter.

CHAPTER IV

RESULTS AND DISCUSSION

4.1 CHAPTER OUTLINE

The mathematical model of the ProbS-FEM was incorporated with the Monte Carlo simulation and the LHS model, as discussed in Chapter 3. This chapter presents the numerical calculations for the ProbS-FEM that was developed. It starts with the verification of the SIF, crack growth and fatigue life. The analysis then continues with the crack growth distribution and the statistical test for use in engineering applications. Subsequently, the sample reduction technique in the ProbS-FEM is presented.

4.2 VERIFICATION OF THE ProbS-FEM APPROACH

This section presents the results and discussion of the ProbS-FEM approach in validating the outputs. Since an algorithm for probabilistic surface crack analysis was developed in this research, it was important to validate the results with other deterministic numerical solutions. Therefore, a comparison was made of the probabilistic and deterministic approaches so that a conclusion could be drawn as to the reliability of the ProbS-FEM. The following subsection presents the verification of the:

(i) Stress intensity factor;
(ii) Crack growth for mode *I*;
(iii) Crack growth for mixed mode; and
(iv) Prediction of fatigue life.

4.2.1 Stress Intensity Factor

A three-dimensional tension model pioneered by Newman & Raju (1981), as shown in Figure 4.1, was used for the verification of the ProbS-FEM. The model was subjected to tension loads. The mode *I* for the SIFs along the crack front was calculated and compared for verification purposes.

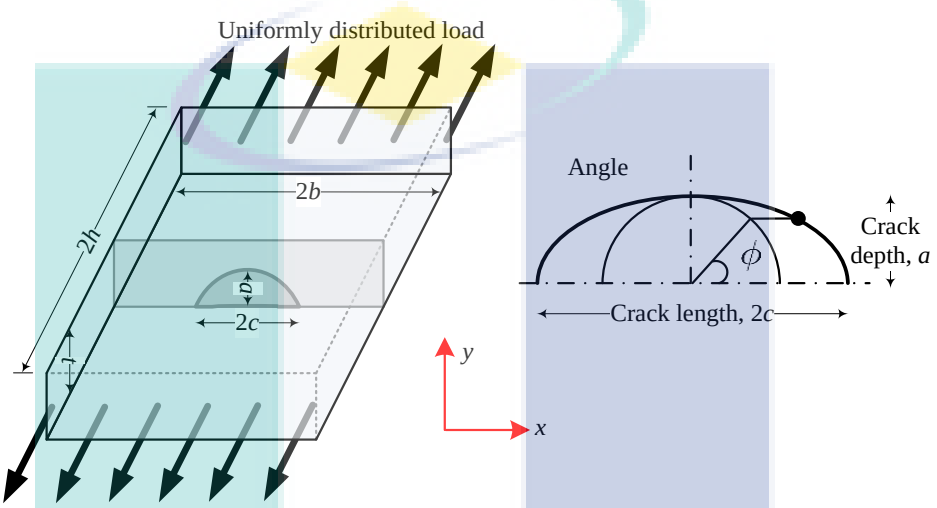

Figure 4.1 Surface crack at centre of tension model

Three models with various aspect ratios were considered to show the capability of the ProbS-FEM in generating SIF values. The details of the models are shown in Table 4.1.

Table 4.1 Classification of the tension model

Tension model	Crack shape aspect ratio, a/c		Crack size aspect ratio, a/t	Model width aspect ratio, c/b	Tension Load, MPa
	Mean	Standard Deviation			
A	0.4	0.01	0.2	0.1	10
B	1.0	0.01	0.2	0.1	10
C	1.0	0.01	0.2	0.1	201

Tension models A and B had different crack shape aspect ratios, while tension model B had a longer crack depth compared to model A. The simulations of models A and B were carried out to show the prediction of the ProbS-FEM for different crack sizes, while the simulation of tension model C was to show the prediction for uncertain load values.

Figure 4.2 and Figure 4.3 show the normalised SIFs along the crack front for tension models A and B. Models A and B were selected to present the various crack shape aspect ratios that can be simulated by the ProbS-FEM. These ratios referred to the crack shape aspect ratios of 0.4 and 1.0, from which different curve patterns could be expected. The SIF values were normalised by $Q(a/c)\sqrt{\pi a}$, where $Q(a/c)$ is the shape factor. The reason for the normalisation was to generalize the result. In this case, the result was not dependent on either the load or the crack size. The loads, as shown in Table 4.1, were based on the calculation in the ProbS-FEM. The ProbS-FEM needs a load to start the calculation since it is based on the principle of virtual work. That was why the loads were stated, as in Table 4.1. Then, the SIF results from the ProbS-FEM were normalised by $Q(a/c)\sqrt{\pi a}$. The normalised results were suitable for comparison purposes regardless of the load and crack size. A detailed explanation regarding the shape factor can be referred to in the study by Murakami et al.(1987). The shape factor is given by

$$Q\left(\frac{a}{c}\right) = \sqrt{\int_0^{\pi/2} \left[1 - \left(1 - \frac{a^2}{c^2}\right) sin^2\theta\right]^{1/2} d\theta} \approx 1 + 1.464\left(\frac{a}{c}\right)^{1.65} \quad (4.1)$$

Figure 4.2(a) and (b) show the comparison of the normalised SIFs along the crack front for tension model A. The SIF curve that was constructed using the ProbS-FEM was compared with the numerical solution by Newman & Raju (1981) (shown as Newman-Raju in Figure 4.2(a) and (b)) and the deterministic S-FEM (Det. S-FEM) solution. The results of the Newman-Raju and deterministic S-FEM solutions were plotted based on the aspect ratio for model A, as shown in Table 4.1. Then, the mean

of the ProbS-FEM was plotted together with the upper and lower bounds (shown as bounds in the Figure 4.2(a)) of the normalised SIFs with the mean and standard deviation of the crack shape aspect ratios of 0.4 and 0.01, respectively. The crack shape aspect ratios were distributed based on the Gaussian distribution. According to Liu & Mahadevan (2009), the crack shape has large uncertainties that cause additional difficulties for the prediction of probabilistic life. This is the reason for the randomness of the crack shape aspect ratio. The mean of the ProbS-FEM was constructed based on a hundred samples. The bounds were calculated based on the minimum and maximum result of the ProbS-FEM.

As shown in Figure 4.2(a), the SIF was higher at $2\phi/\pi = 1$ than at 0. This confirmed that the numerical results were plausible. With respect to the surface crack depth, the calculation of the SIF in the ProbS-FEM was sensitive (as reflected in these results). A comparison showed that the mean ProbS-FEM agreed with the finding of the Newman-Raju solution. As the angle was increased, the mean of the ProbS-FEM showed a slight deviation from the finding of the Newman-Raju solution as it was influenced by the modelling of uncertainties in the analysis. The bounds showed the range of the normalised SIFs as the crack shape aspect ratio was modelled as an uncertain parameter.

Figure 4.2(b) shows that the same results were obtained by the Newman-Raju solution as by the deterministic S-FEM and mean ProbS-FEM in Figure 4.2(a), except for the bounds. The bounds in Figure 4.2(b) had a 95% confidence level, based on the calculation using Eq.(3.60). The 95% confidence bounds are the range within which 95% of the results of the ProbS-FEM can be found. The 95% confidence bounds are presented in Figure 4.2(b) due to their application in fatigue analysis such as in aircraft structural designs (Huang et al., 2012). Figure 4.2(b) shows that the results of the Newman-Raju solution were excluded from the range of the 95% confidence bounds. The highest deviation between the mean ProbS-FEM and the Newman-Raju solution was five per cent at an angle of zero. This was considered a small deviation since it involved a few assumptions in the Newman-Raju solution. For instance, the

Newman-Raju solution assumes a limiting behaviour as *a*/*t* approaches zero. Thus, a five per cent error is acceptable.

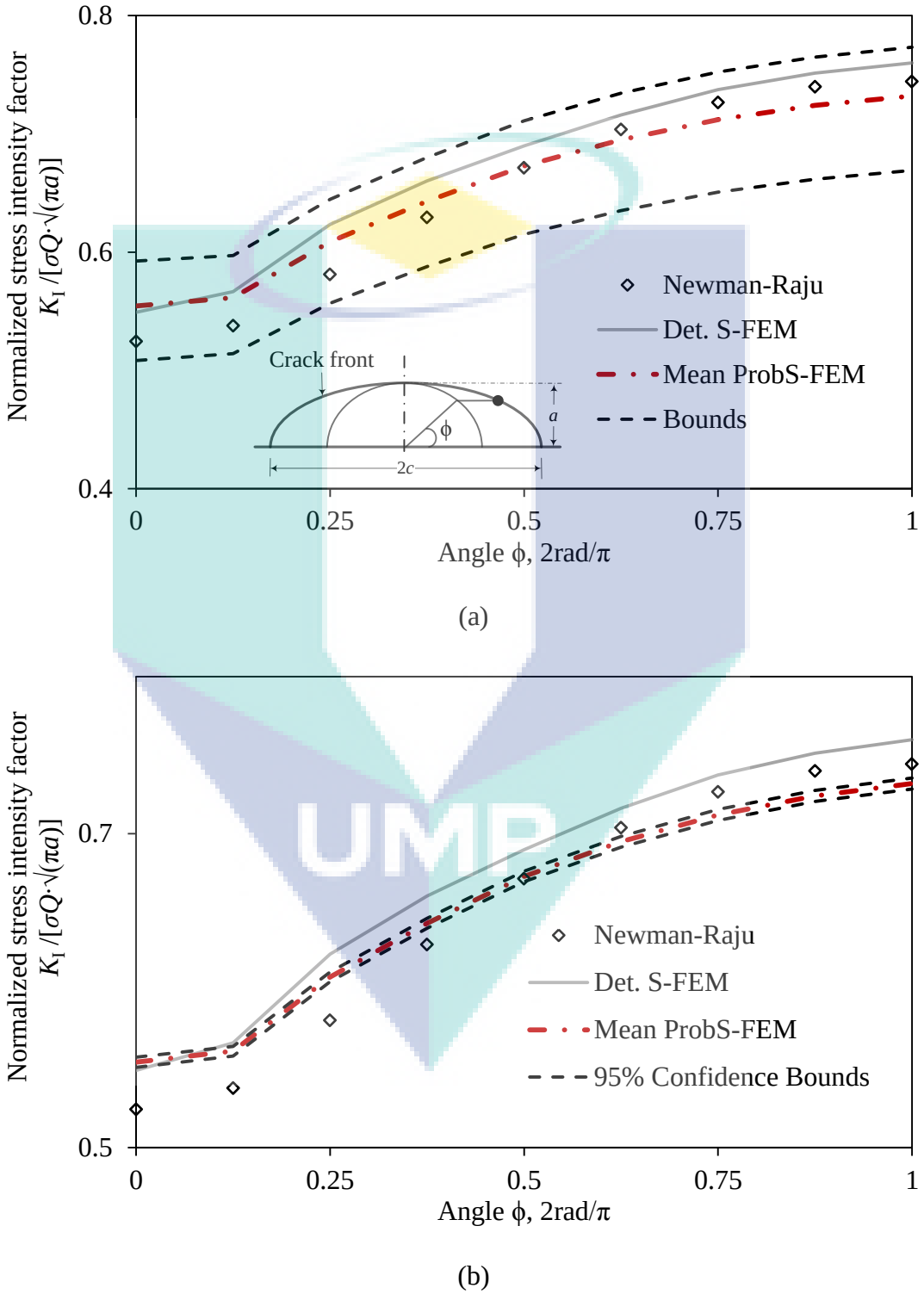

Figure 4.2 Normalised SIFs along crack front in tension model A with (a) upper and lower bounds (b) 95% confidence bounds

Figure 4.3(a) and (b) show the comparison of the normalised SIFs along the crack front for tension model B. Unlike tension model A, the crack shape aspect ratio for model B was increased to 1.0, whereas the crack size and model width aspect ratio were maintained the same as with model A. The reason behind this was to certify the prediction of the SIFs by the ProbS-FEM for larger crack shapes. The calculation was compared with the results using the Newman & Raju (1981) solution (shown as Newman-Raju in Figure 4.3(a) and (b)) and the deterministic S-FEM (Det. S-FEM). The results were plotted based on the aspect ratio for model B, as shown in Table 4.1. Subsequently, the mean of the ProbS-FEM was plotted together with the upper and lower bounds (shown as bounds in Figure 4.3(a)) of the normalised SIFs with the mean and standard deviation of the crack shape aspect ratio being 1.0 and 0.1, respectively. The mean of the ProbS-FEM was constructed based on a hundred samples. The bounds were the maximum and minimum samples from the ProbS-FEM. The mean value curve of the SIF deviated by less than four per cent from the numerical solution of the Newman-Raju equation.

Figure 4.3(b) shows the 95% confidence bounds with the results of the Newman-Raju solution, the deterministic S-FEM and the mean ProbS-FEM that were duplicated from Figure 4.3(a). The comparison shows that the 95% confidence bounds deviated four percent from the Newman-Raju solution at a zero angle due to the assumption of a semi-elliptical shape for the surface crack in the Newman-Raju solution. That was the reason why the maximum deviation occurred at a zero angle.

Then, the normalised SIFs that had been calculated by the ProbS-FEM were plotted against the normalised SIFs calculated by the Newman-Raju solution, as shown in Figure 4.4. In order to measure how much of the variance in the ProbS-FEM was explained by the Newman-Raju solution, the coefficient of determination, R^2 was calculated. If R^2 was close to one, then the normalised SIF that had been calculated by the ProbS-FEM tightly mirrored that of the Newman-Raju solution. The R^2 calculated

from the correlation analysis in Figure 4.4 showed a good prediction by the ProbS-FEM.

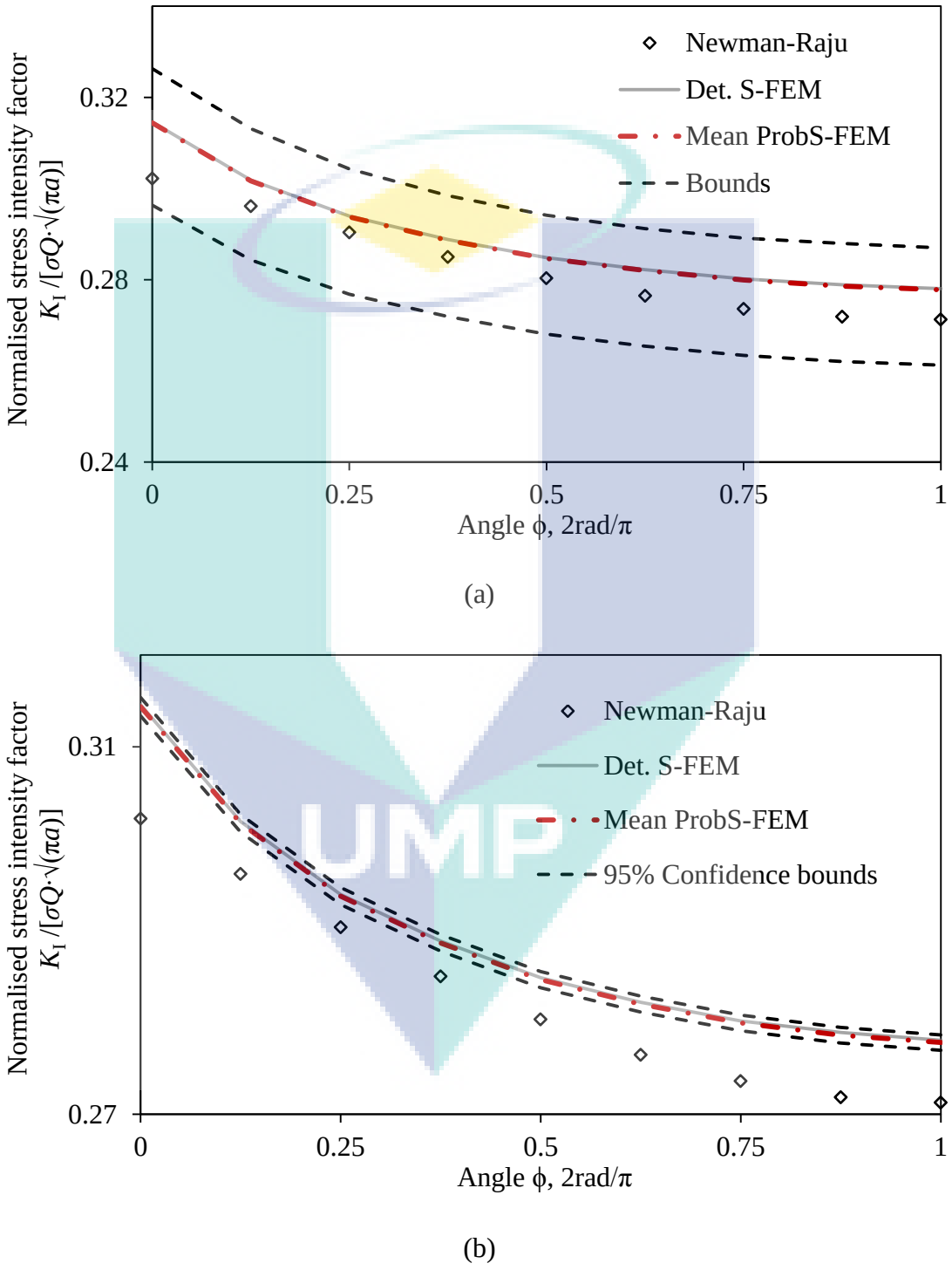

Figure 4.3 Normalised SIFs along crack front in a tension model B with (a) upper and lower bounds, and (b) 95% confidence bounds

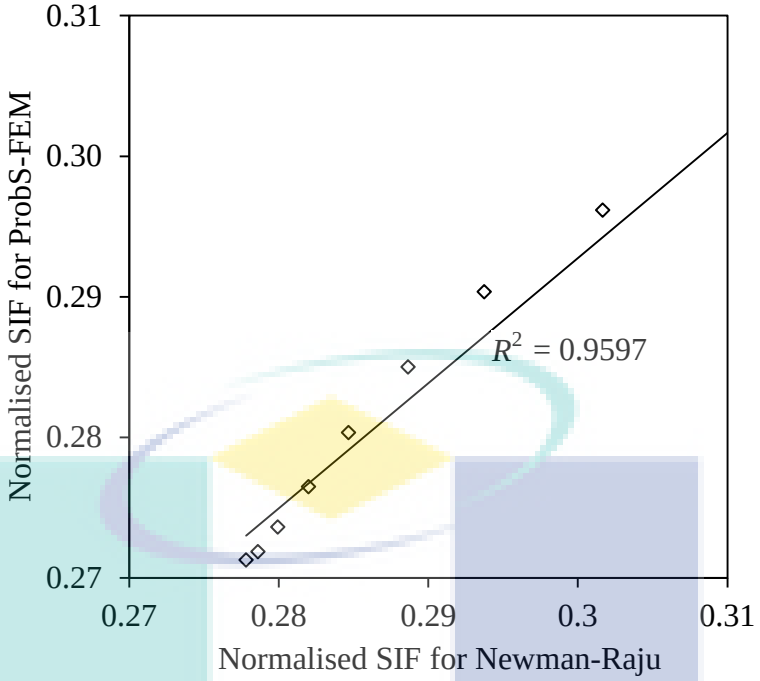

Figure 4.4 Comparison of normalized SIFs between Newman-Raju and ProbS-FEM

The proposed ProbS-FEM approach revealed an important issue when the un-normalised SIFs versus the angles were plotted. The random load with a constant amplitude loading was considered with a mean of 201 MPa and a standard deviation of 20.1 MPa. The load was considered since it was less than the yield strength and was an average load for Aluminium 7075-T6 in industrial applications (Liu & Mahadevan, 2009). Figure 4.5(a) and (b) show the SIFs along the crack front for tension model C. Details of the aspect ratio for model C can be referred to in Table 4.1. The material properties of Aluminium 7075-T6 were used for this model, as shown in Table 4.2. The deterministic results did not exceed the critical SIF of 29 MPa·√m, thus predicting a safe structure because an unstable crack growth will not occur for an SIF below this critical value. However, this only reflected the mean behaviour. The upper bound exceeded the critical SIF, thus indicating a significant probability for unstable crack growth, as shown in Region Z in Figure 4.5(a). Thus, the fracture of the material and the structural component could occur. A quantitative result for the structural safety was obtained with the probability of failure estimated from the sampled data. Figure 4.5(b) shows the 95% confidence bounds with the calculated results from Figure 4.5(a). In this case, the Newman-Raju solution was within the range of the 95%

confidence bounds. A small deviation occurred at a zero angle in Figure 4.5(b), but it was still within the range of the 95% confidence bounds.

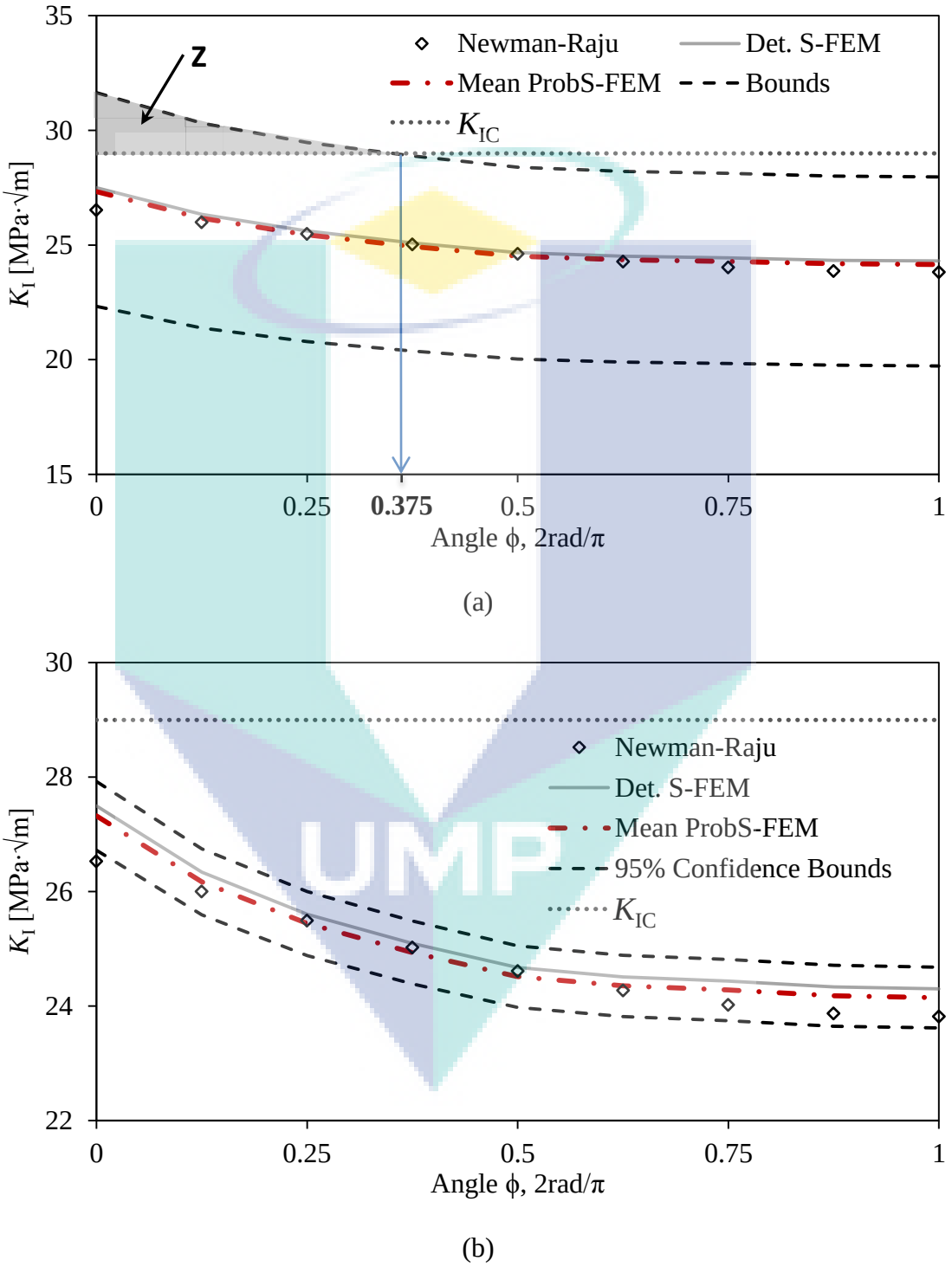

Figure 4.5 SIFs along crack front in tension model C with (a) upper and lower bounds, and (b) 95% confidence bounds

Table 4.2 Material properties for Aluminium 7075-T6

Variable	**Value**
Critical stress intensity factor, K_{IC}	29 MPa·√m
Fatigue power parameter, *n*	2.88
Poisson ratio, *PR*	0.33
Tensile Strength, Yield	503 MPa
Young's modulus, *E*	71.7 GPa
Paris coefficient, *C*	2.29×10^{-10}
Threshold value, ΔK_{th}	5.66 MPa·√m

Figure 4.6 shows the histogram for the SIF at $2\phi/\pi = 0$ for tension model C. The maximum and minimum stresses were 33.50 and 22.32 MPa·√m, respectively. The mean value was 27.50 MPa·√m. The maximum and minimum deviations from the mean were 6.00 and 5.18 MPa·√m, respectively. Although the range between the minimum and maximum was only approximately 11.20 MPa·√m, this did not produce a major uncertainty. Even though it showed a small range of uncertainty, it was crucial when analysed with a critical SIF. The critical SIF, K_{IC} for this case was 29 MPa·√m. Thus, 60% of the samples were in the safe region and 40% were in the failure region. The failure region means the occurrence of unstable crack growth. This forecast cannot be produced by the deterministic method. The deterministic approach predicts that the model is in a safe region at any angle. Figure 4.5(a) shows that the failure of the sample occurred from an angle of $2\phi/\pi = 0$ to 0.375. This result demonstrated the importance of a probabilistic analysis in the context of fatigue problems to avoid structural failure and potentially harmful consequences. Hence, an implementation of a probabilistic design is advisable in practical cases.

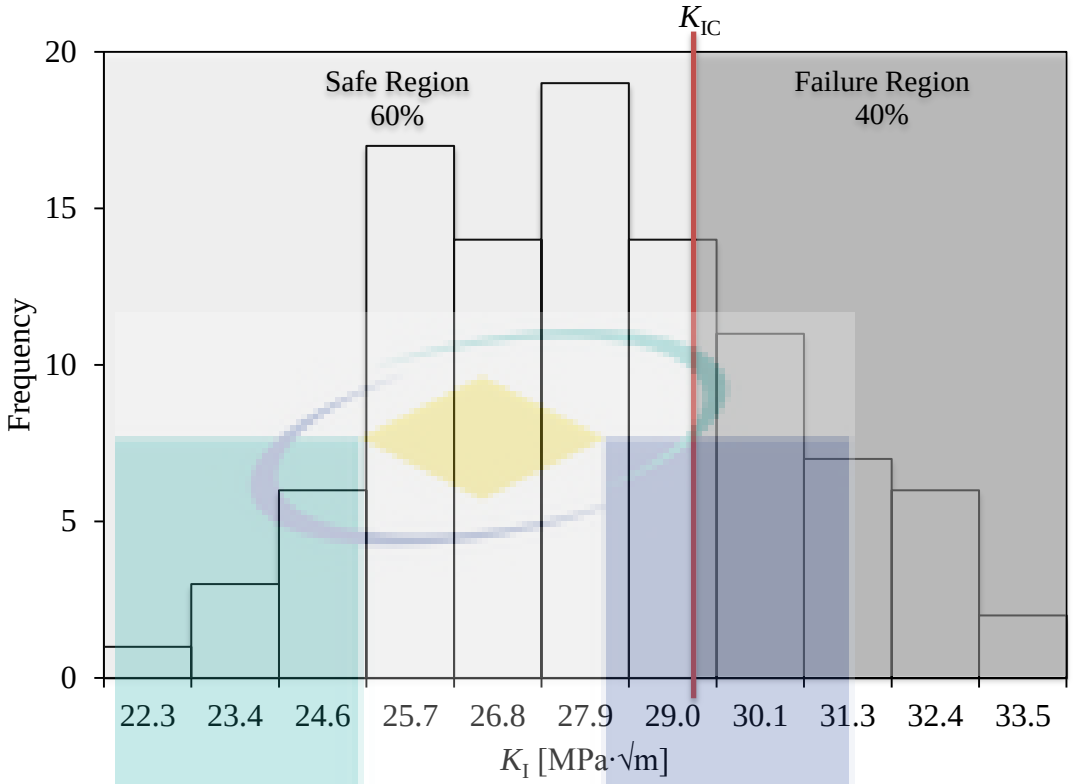

Figure 4.6 Histogram of SIFs at $2\phi/\pi = 0$ for tension model C

The calculation of the SIFs for tension models A and B were verified and shown to be in agreement with other deterministic numerical calculations in Figure 4.2 and Figure 4.3, respectively. Then, the important issues and applications were presented by tension model C. Thus, the reliability of the ProbS-FEM in producing the SIF was proven. The verification of the ProbS-FEM was continued with the surface crack growth.

4.2.2 Crack Growth for Mode *I*

A four-point bending model and specimen were used for the verification of crack growth. The experimental setup was conducted based on the procedure in Section 3.7. The crack length between the beach marks was measured and compared with the ProbS-FEM analysis. Figure 4.7 shows a photo of the surface crack plane from the 0-degree fractured specimen. The schematic diagram of the 0-degree specimen is shown in Figure 3.19.

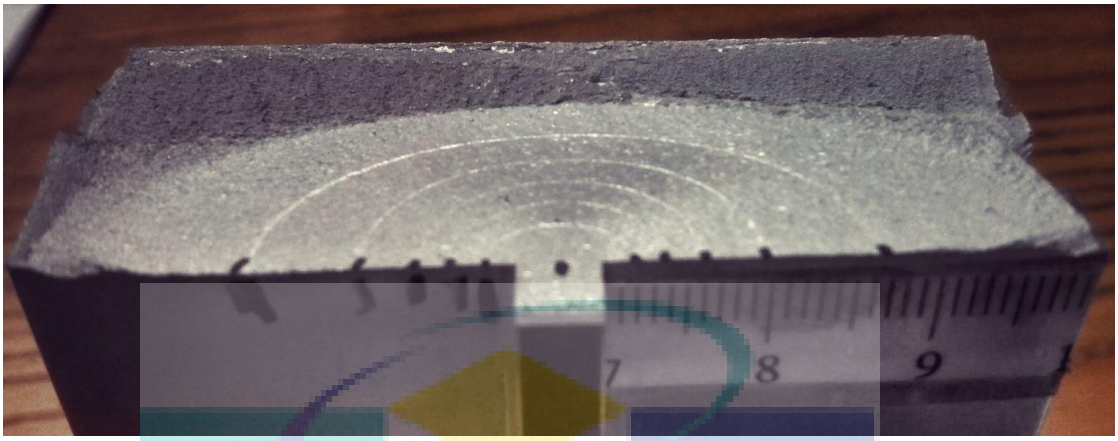

Figure 4.7 Photo of four-point bending specimen with centimetre label

The bending model shown in Figure 4.8 was used to predict the crack growth. The analysis demonstrated the flexibility in applying the developed approach with respect to different models. A specific feature of the bending model was the deceleration effect on the crack growth due to bending. Thus, the bending model was used for the purpose of verification. The material properties were simulated according to the specifications in Table 4.3. In order to control the acceleration of fatigue crack growth, the fatigue power parameter, n was set as a deterministic variable. The standard deviation for the critical SIF, K_{IC} and the yield tensile strength were set to zero as the variable itself acted as the value for comparison. Both the material constants were compared with the simulation results. For instance, the SIF that was calculated from the ProbS-FEM was compared with the critical SIF for the determination of unstable crack growth. Thus, it was not appropriate to randomise the critical SIF, K_{IC} and the yield tensile strength. The maximum load was 45 kN with a stress ratio of 0.1.

In the numerical simulation with the ProbS-FEM, the boundary conditions were defined to be the same as in the experiment, and the four-point bending process was analysed. The size of the pre-cracking area was modelled in a local mesh. The crack growth was calculated based on Eq. (3.50).

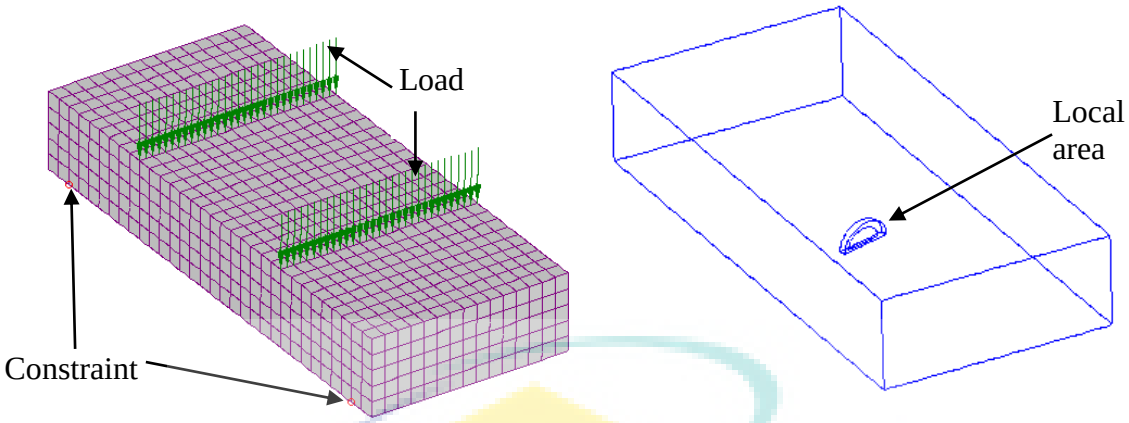

Figure 4.8 Global mesh with boundary conditions and overlaid local mesh in wireframe view of four-point bending model

Table 4.3 Input distribution for Aluminium 7075-T6

Variable	**Distribution**	**Deterministic / Mean Value**	**Standard deviation**
Critical stress intensity factor, K_{IC}	Deterministic	29 MPa·√m	0
Fatigue power parameter, n	Deterministic	2.88	0
Tensile Strength, Yield	Deterministic	503 MPa	0
Young's modulus, E	Gaussian	71.7 GPa	0.01
Paris coefficient, C	Lognormal	2.29×10^{-10}	4.01×10^{-10}
Threshold value, ΔK_{th}	Lognormal	5.66 MPa·√m	0.268
Initial crack depth, a_i	Gaussian	3.87 mm	0.1
Initial crack length, c_i	Gaussian	4.50 mm	0.1

In order to conduct the analysis in mode *I* condition, a zero-degree fatigue crack was used. Figure 4.9 shows half of the crack growth in the four-point bending specimen in the experiments and the deterministic S-FEM. Only two beach marks are shown to avoid a complicated graph. The deterministic results were represented by the dash lines. A divergence appeared when the experimental results were compared to the deterministic results, and thus, a remedy was required to improve the analysis. A probabilistic approach was used to enhance the outputs and to demonstrate the capability of the developed software. The ProbS-FEM was used to provide a probabilistic perspective of the results. In total, 50 samples were used to generate the

probabilistic crack growth. The mean of the 50 samples, which was named the Mean ProbS-FEM, is illustrated in Figure 4.9. The 95% confidence bounds from the results of the ProbS-FEM were plotted as in Figure 4.9. The 95% confidence bounds were calculated from Eq. (3.60). In addition, Figure 4.9 shows that the experimental results were between the lower and upper confidence bounds. Although the mean of the ProbS-FEM diverged from the experimental results, the experimental results were between the bounds of the ProbS-FEM. These results indicated that the consideration of uncertainty in the analysis produced an improvement in the crack growth results. A repetition of the experimental works exposed the uncertainties in the initial crack size and material. This was the main factor that caused the deterministic result to diverge from the experimental results. Therefore, the ProbS-FEM is a reliable simulation tool for the prediction of fatigue crack growth.

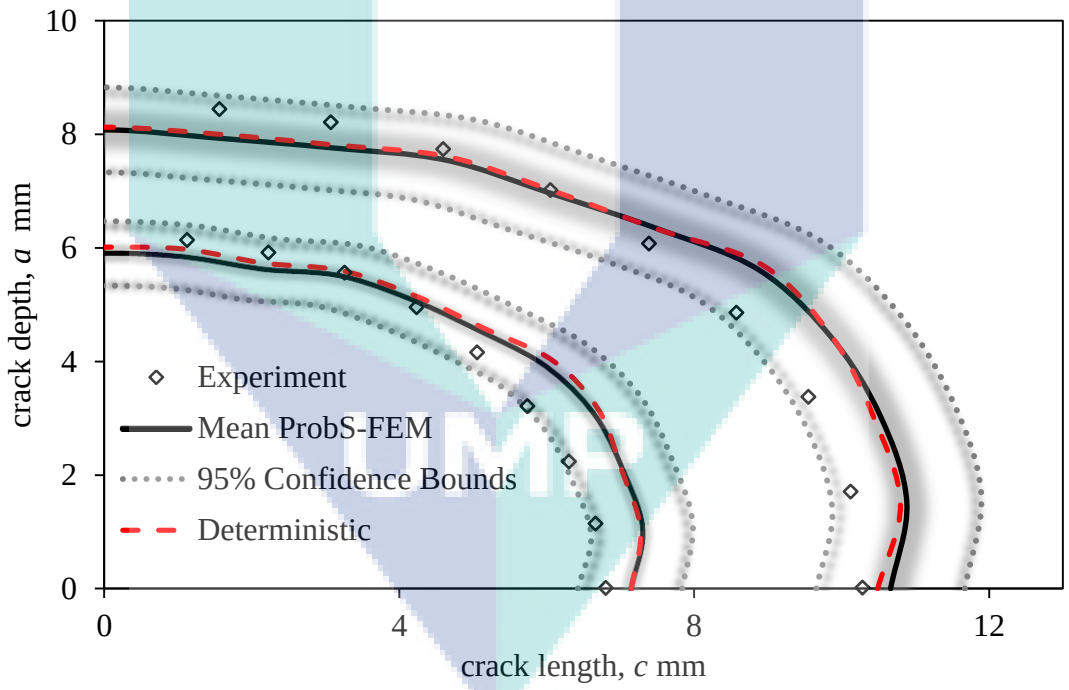

Figure 4.9 Comparison between experimental, deterministic and ProbS-FEM results for two 0-degree beach mark cracks

4.2.3 Crack Growth for Mixed Mode

The specimen with a 30-degree crack angle was prepared, as explained in the methodology section. Figure 4.10 shows a photo of the slanted surface crack plane from the fractured specimen. The load that was applied to the specimen was in a

mixed mode (mode *I* and *III*) condition because the crack was initiated at a 30-degree angle. The material properties were simulated according to the specifications in Table 4.3. This section presents the crack growth for the mixed mode condition.

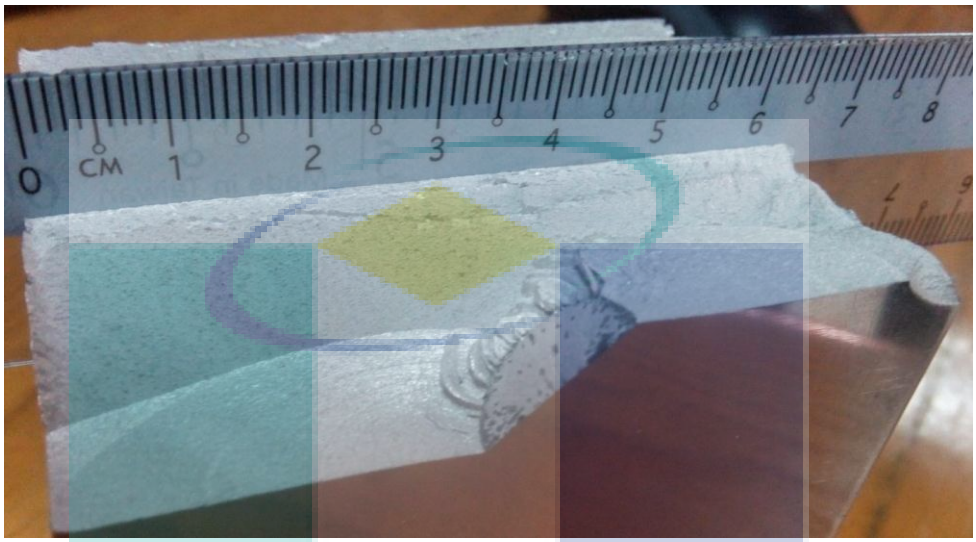

Figure 4.10 Photo of four-point bending specimen with mixed mode condition

Figure 4.11(a) and (b) show the comparisons between the deterministic, experimental and ProbS-FEM crack growth for the four-point bending specimen with a 30-degree crack angle. To present a well-ordered graph, two beach marks were plotted. Each beach mark had a deterministic, experimental, mean ProbS-FEM and bounds or confidence bounds result. The crack growth for the smaller beach marks in Figure 4.11(a) and (b) agreed with all the methods. As the crack grew, the crack length grew more than the crack depth because of the stress intensity factor in Mode *III* (as shown in the second beach mark). The deterministic result showed a noticeable divergence from the experimental finding. The mean ProbS-FEM approached the experimental finding. However, the mean ProbS-FEM showed a better comparison with the deterministic result. A complete view of the probabilistic analysis illustrated the advantages of the ProbS-FEM analysis, as shown by the bounds of the ProbS-FEM. The bounds were drawn and calculated from the minimum and maximum of the ProbS-FEM results. The experimental results were between the bounds, displaying the capability of the ProbS-FEM in predicting the bounds of crack growth for the mixed mode load. When the bounds were limited to the 95% confidence level, as shown in Figure 4.11(b), the experimental data were out of the 95% confidence bounds for the

second beach mark. However, this was not critical as only a deviation of less than five percent occurred.

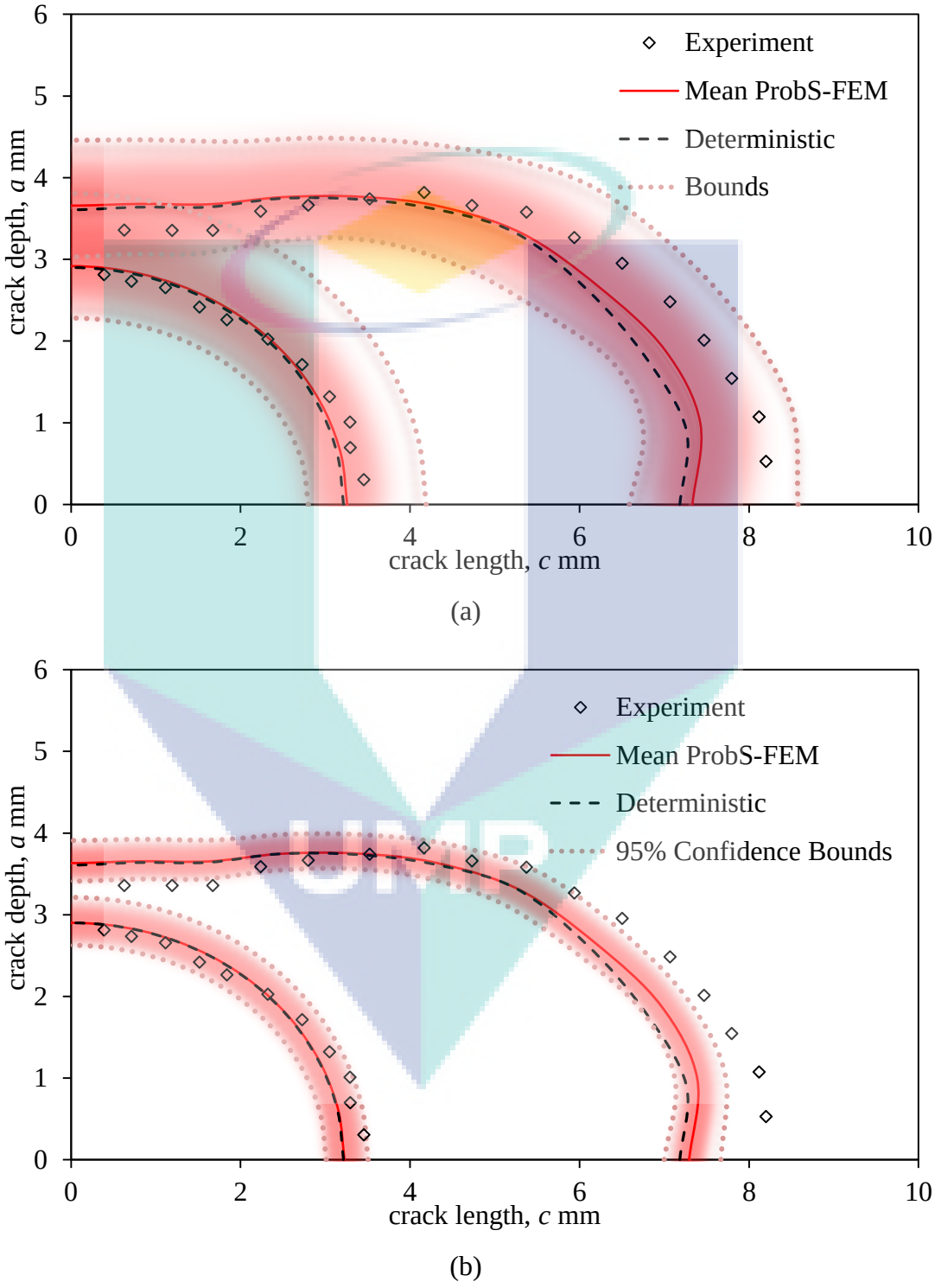

Figure 4.11 Comparison of the experimental, deterministic and ProbS-FEM results for two 30-degree beach mark cracks with (a) upper and lower bounds, and (b) 95% confidence bounds

4.2.4 Prediction of Fatigue Life

The verification of the ProbS-FEM continued with the prediction of fatigue life. The prediction of fatigue life is an essential feature in the development of source codes. Thus, the calculations of fatigue life by the experimental and deterministic approaches were compared for verification. Two models were used for the verification, namely a three-point bending model and a four-point bending model. A different material was used for both models to examine the capability of the ProbS-FEM in simulating various case studies. Table 4.4 shows the material properties of Aluminium (2017-T3), which was the material used for the three-point bending model. For the four-point bending model, Aluminium (7075-T6) was used, as shown in Table 4.3.

Table 4.4 Input distribution for the Sano (2010) model using Aluminium (2017-T3)

Variable	**Distribution**	**Deterministic / Mean Value**	**Standard deviation**
Critical stress intensity factor, K_{IC}	Deterministic	26 MPa·√m	0
Fatigue power parameter, n	Deterministic	2.93	0
Tensile Strength, Yield	Deterministic	333 MPa	0
Young's modulus, E	Gaussian	70.2 GPa	0.01
Paris coefficient, C	Lognormal	2.66×10^{-10}	$4.01\text{x}10^{-10}$
Threshold value, ΔK_{th}	Lognormal	6.7 MPa·√m	0.268
Initial crack depth, a_i	Gaussian	2.85 mm	0.05
Initial crack length, c_i	Gaussian	5.00 mm	0.05

Figure 4.12 shows the comparison between the experimental (Sano, 2010), deterministic and probabilistic fatigue crack growth for the three-point bending model. The fatigue crack growth was calculated based on Eq. (3.50). The deterministic results were obtained when the standard deviations for all the variables in Table 4.4 were set to zero. The mean fatigue life was calculated based on the average of one hundred samples. The deterministic and experimental results were predicted to be between the 95% confidence bounds (as denoted by the dash lines). The bounds represented the

range of possibilities for the fatigue life. They showed how certain the real fatigue life was scattered within the bounds. When compared with the deterministic approach, the mean ProbS-FEM analysis was found to be closer to the experimental results. Even though the correlation analysis in Figure 4.13 showed the same value of R^2, the trend of the mean ProbS-FEM towards the experimental findings in Figure 4.12 was noteworthy. The ProbS-FEM approach included the uncertainty of the material properties, the initial crack length and the initial crack depth in the analysis model. Meanwhile, the deterministic approach neglected the uncertainty in its calculation. Therefore, the ProbS-FEM solution was closer to reality. Moreover, the ProbS-FEM produced the minimum and maximum cycles before the unstable crack growth occurred. For instance, the minimum and maximum cycles at a 14-mm crack length were 36 and 44 Kilocycles, respectively. This result can assist maintenance personal in establishing an adequate repair schedule.

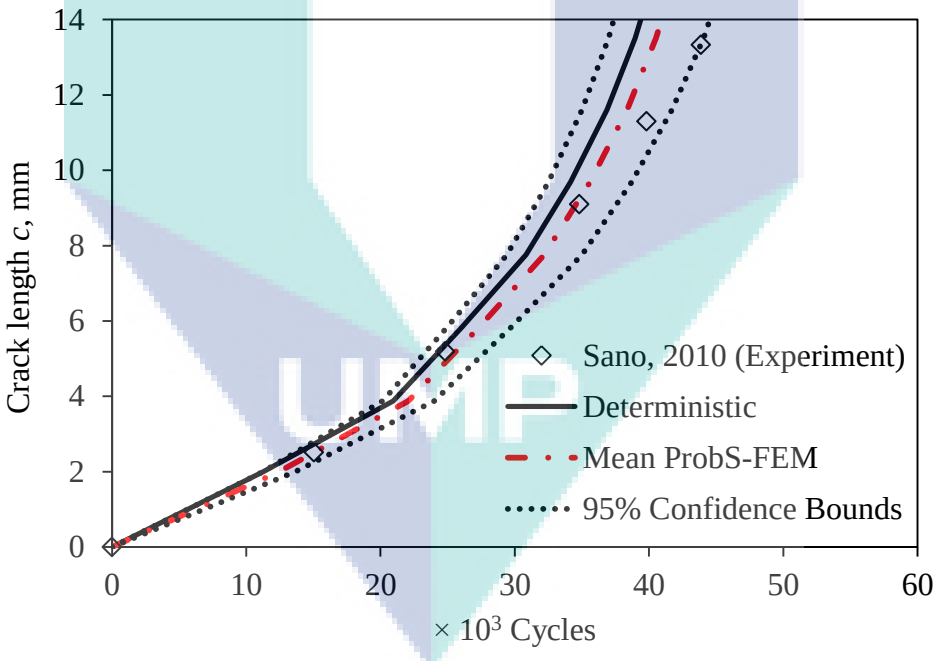

Figure 4.12 Comparison of experimental and ProbS-FEM results according to fatigue life prediction of three-point bending specimen

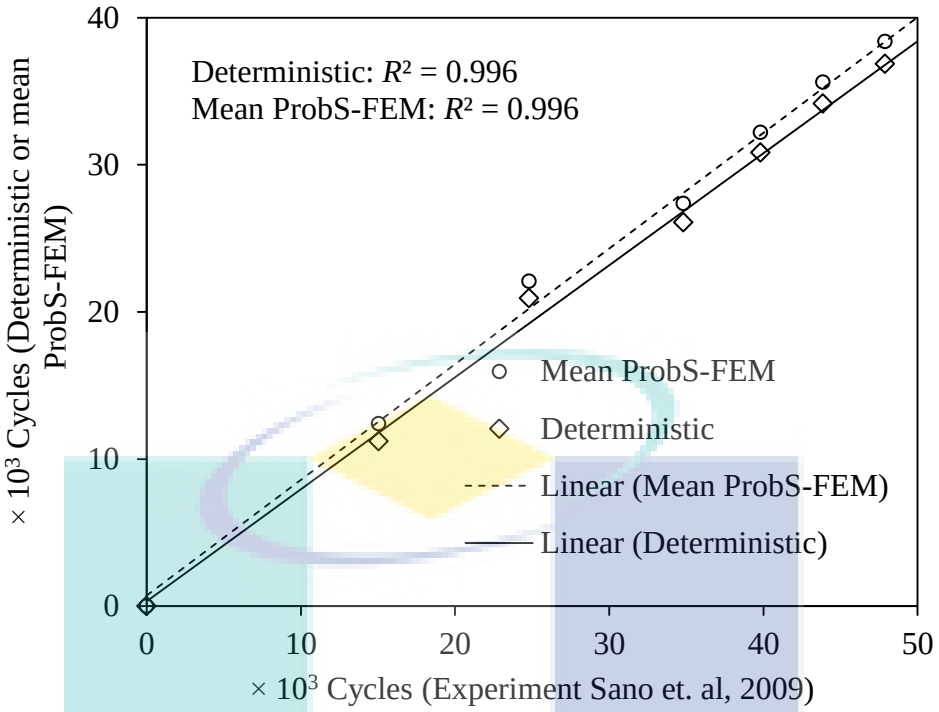

Figure 4.13 Correlation analysis of predicted cycles versus experimental cycles

The experimental results for the four-point bending test are shown in Figure 4.14. Six specimens were tested under the four-point bending test and various results were produced for the crack length versus the cycles. The mean with the bound bar of the experimental results were plotted, as shown in Figure 4.14. The bound bars were plotted based on the calculation of the mean and standard deviation obtained from the experimental results. The details of the calculation can be referred to in Eq. (3.60). The uncertainty in the material contributed to the wider bounds in the results. The experimental results were then compared with the results of the simulation conducted by Ohdama (2012). The input variables in Ohdama (2012) were identical to the mean in Table 4.3. Because Ohdama (2012) conducted a deterministic analysis, no standard deviation was involved. The deterministic analysis was conducted through the S-version of the FEM, and a divergence was noted resulting from the uncertainty in the experimental work. In addition, the crack depth and length size varied for each specimen, and the average of the sizes was used as the crack size in the deterministic S-version of the FEM. Therefore, the results presented by Ohdama (2012) had a smaller number of cycles.

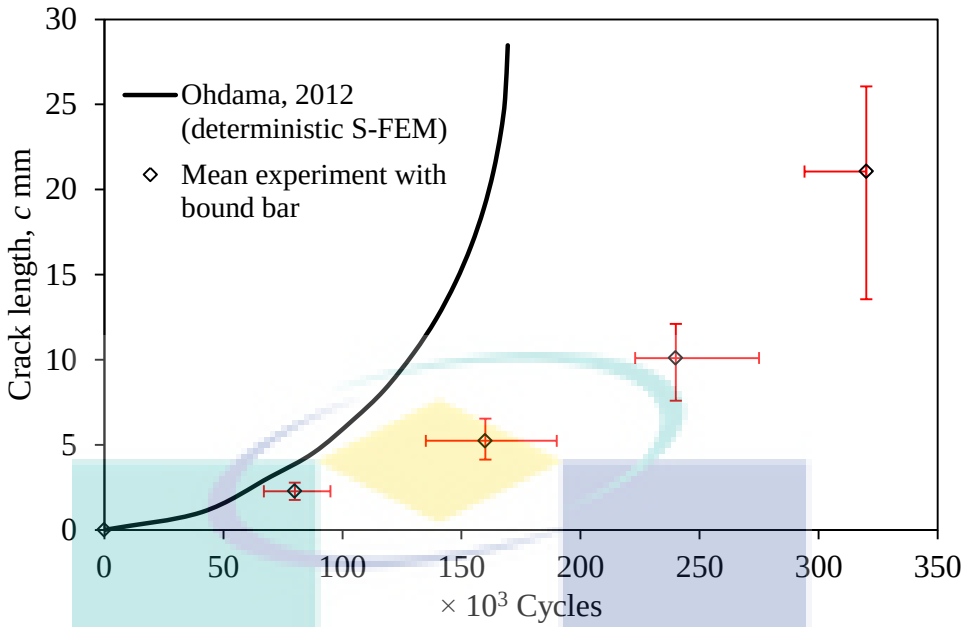

Figure 4.14 Comparison of results of fatigue life between experimental and deterministic S-FEM by Ohdama (2012) for four-point bending model

Subsequently, the specimen was modelled by the ProbS-FEM, and a comparison between the experimental, deterministic and probabilistic results is shown in Figure 4.15. The deterministic and experimental results were duplicated from Figure 4.14. The dash lines with circle markers represent the probabilistic results. The mean ProbS-FEM was plotted from the average of 50 samples. The input variables for each sample were generated from Table 4.3. The mean of the ProbS-FEM was nearer to the mean of the experimental results than the deterministic results. Therefore, the improved results were shown. The prediction of the fatigue life that was obtained using the ProbS-FEM was more accurate than that obtained by a deterministic analysis. A few of the uncertain parameters that were modelled in the ProbS-FEM contributed more to the randomness of the fatigue cycles. This depended on the sensitivity of the parameters.

The Young's modulus, E, the initial crack depth, a_i, and the initial crack length, c_i were the sensitive parameters in the calculation of the fatigue cycles, as shown in Figure 4.16. This was due to the correlation of conversion of the energy release rate to the SIF in Equations (3.47), (3.48) and (3.49). Then, the equivalent SIF, ΔK_{eq} was directly used for the fatigue cycle calculation. In addition, the high magnitude of the Young's modulus contributed more sensitivity to the fatigue cycle

calculation. Besides the Young's modulus, the initial crack depth and crack length were also implicitly correlated with the fatigue cycle. That was why the initial crack depth and crack length had a smaller sensitivity compared to the Young's modulus. The sensitivity analysis was based on the Pearson function. This function returns the Pearson product moment correlation coefficient, r_P, as shown below

$$r_P = \frac{\sum(x-\bar{x})(y-\bar{y})}{\sqrt{\sum(x-\bar{x})^2 \sum(y-\bar{y})^2}} \tag{4.2}$$

where x is the independent value and y is the dependent value. The Pearson product moment correlation coefficient, r_P is a dimensionless index that ranges from -1.0 to 1.0. The r_P reflects the extent of a linear relationship between a random parameter and a fatigue cycle. Based on Figure 4.16, the Young's modulus, initial crack depth and initial crack length were the main factors that contributed to an increase or decrease in the fatigue cycles. A positive sensitivity contributed to an increase in the fatigue cycles and vice versa.

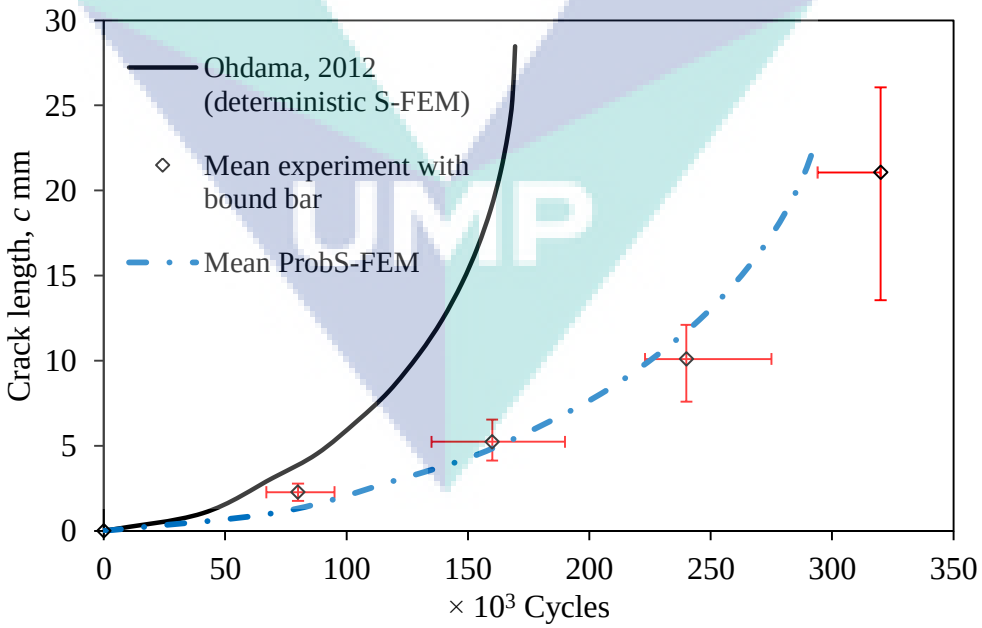

Figure 4.15 Comparison of the means of the experimental, probabilistic and deterministic S-FEM (Ohdama, 2012) results for the four-point bending model

The sensitivity of the Young's modulus was contributed during the conversion of the energy release rate to the SIF, as shown in Equations (3.47) and (3.48). The leading cause of this was the direct correlation for the Young's modulus during the conversion from the energy release rate to the SIF. The initial crack depth, a_i and initial crack length, c_i displayed sensitivity to the fatigue cycles due to the implicit correlation with the fatigue cycle calculation. Thus, three random parameters showed sensitivity to the fatigue cycle calculation.

The Paris coefficient and threshold value had less influence on the calculation of fatigue life. Since the value of the Paris coefficient was too small, it had no influence on the calculation of the fatigue cycle. The threshold value was used to determine whether the fatigue criteria applied or vice versa. Thus, the threshold value indicated no sensitivity to the fatigue cycle. Therefore, this result showed that the ProbS-FEM was capable of predicting the fatigue life of cracked structures by producing a sensitivity analysis of each uncertain parameter.

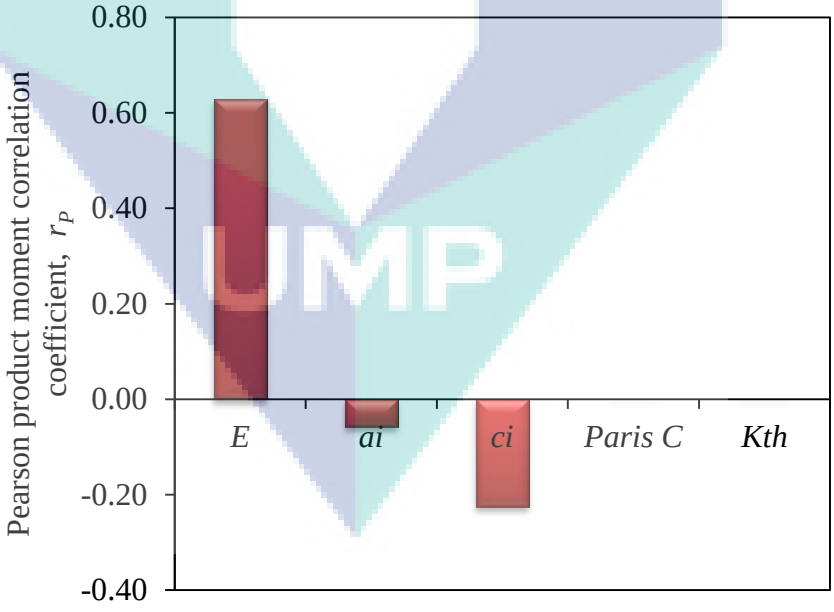

Figure 4.16 Sensitivity analysis for the fatigue cycle calculation of four-point bending model

4.3 CONTRIBUTIONS AND IMPROVEMENTS IN ANALYSIS

This section presents the engineering applications of the ProbS-FEM as a contribution to the existing probabilistic crack analysis. The single and multiple surface cracks analyses were conducted to show the contribution to the computational aspect of fracture mechanics analysis. The subsection on 'Sample reduction in the ProbS-FEM' presents the enhancement of the sampling strategy in the analysis. The three subsections are presented next.

4.3.1 Single Surface Crack

Even though the single surface crack problem was presented in Section 4.2, a further analysis of the ProbS-FEM is continued in this current section. This subsection focuses on the crack growth distribution and the statistical test for determining the underlying crack growth distribution. The four-point bending model was simulated, based on the specifications in Table 4.3.

The variability in the crack growth (due to the randomness of the uncertain parameters) is shown in Figure 4.17. These results covered all the possible options for crack growth. The histograms for both the crack depth and crack length increments were plotted in this illustration. The range for the crack depth increment was [2.05, 2.29] mm, while the range for the crack length increment at point Z was [3.31, 3.68] mm. The crack length and crack depth increments in the samples showed a skewness and kurtosis that were close to zero. This motivated an approximation of the histograms with a Gaussian distribution. The mean and standard deviation of the crack length and depth increments are presented in Table 4.5.

The empirical CDFs (ECDFs) are shown in Figure 4.18 (see also Table 4.5 for their estimated parameters). The ECDF was calculated based on the corresponding stepwise CDF of the observed ordered samples. The ECDF is like an ideal CDF line for the assumed distribution. For instance, the crack depth increment was assumed to fit as a Gaussian distribution, as shown in Table 4.5.

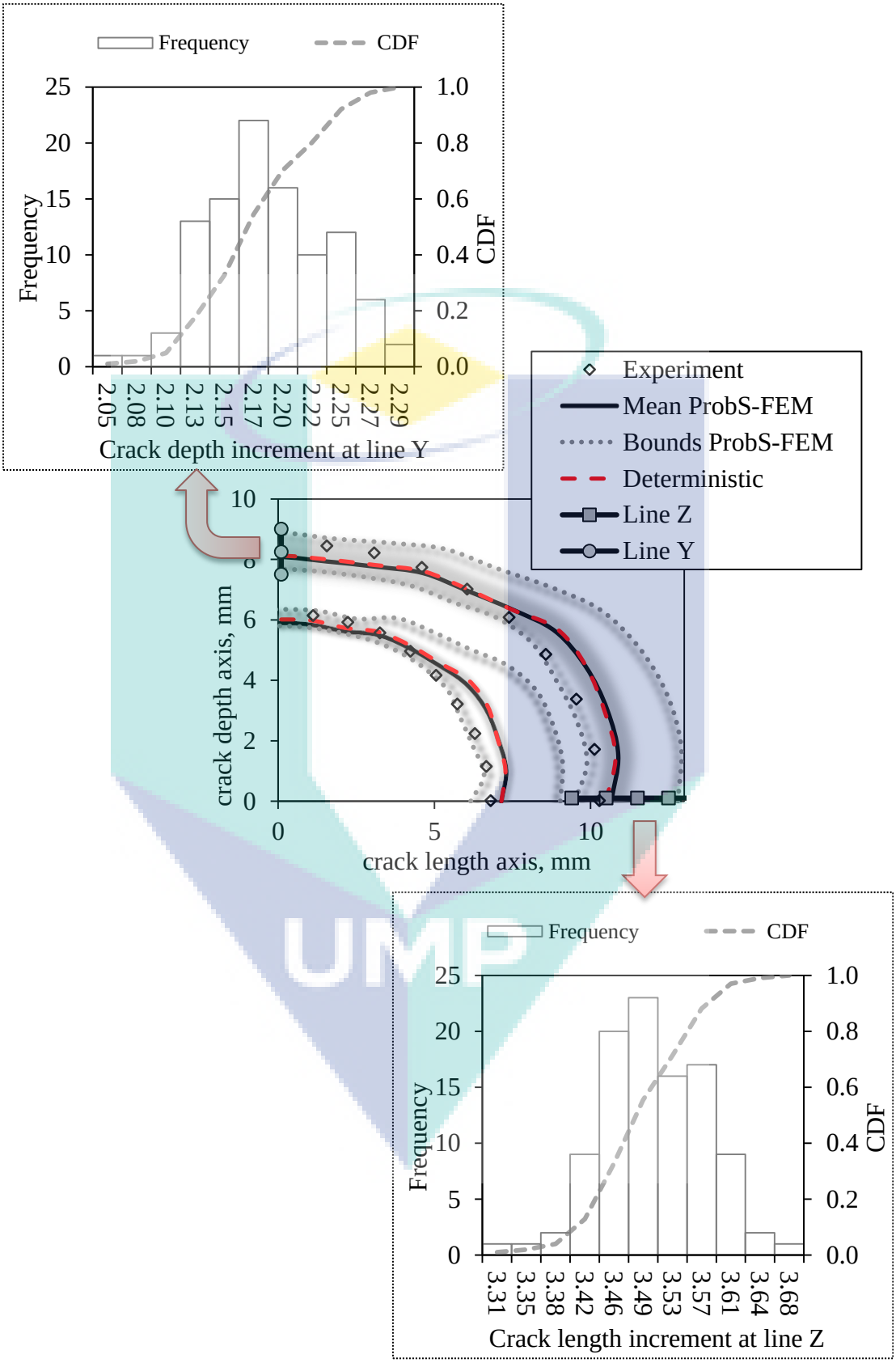

Figure 4.17 Crack growth on surface crack with distribution of crack length and depth increments

Therefore, the ECDF (in this case, a Gaussian CDF) was a step function that had a step of one over the total samples at each of the observed data points (as plotted in Figure 4.18). It was found that the ECDF was an estimate of the true CDF. In order to compare the ECDF with the CDF of the crack length or depth increment, the CDF from Figure 4.17 was redrawn in Figure 4.18 and labelled as the ProbS-FEM. The CDFs of the crack length and depth increment were generated from the ProbS-FEM simulation.

Table 4.5 Statistical data of crack growth distribution

Point	**Mean (mm)**	**Standard deviation (mm)**	**Assumed type of distribution**	**Maximum difference,** D_n
Y	2.17	0.052	Gaussian	0.0464
Z	3.49	0.065	Gaussian	0.0441

A K-S test was performed to assess the suitability of the Gaussian models for the crack growth at points Y and Z. Table 4.5 shows the maximum differences between the ECDFs and the estimated Gaussian distributions as a basis for the K-S test. The largest rejection probability found was 0.1360 for points Y and Z. Since the maximum difference, D_n was less than the largest rejection probability, the crack growth could be represented as a Gaussian distribution. Figure 4.18 shows that the estimated Gaussian distributions were in good agreement with the ECDFs. These results support the Gaussian model for both crack length and crack depth increments. This type of model is useful for the maintenance process if the crack length is below the threshold of an inspection limit. Since the crack growth displayed some amount of scatter, it was imperative to treat the residual life from a probabilistic viewpoint.

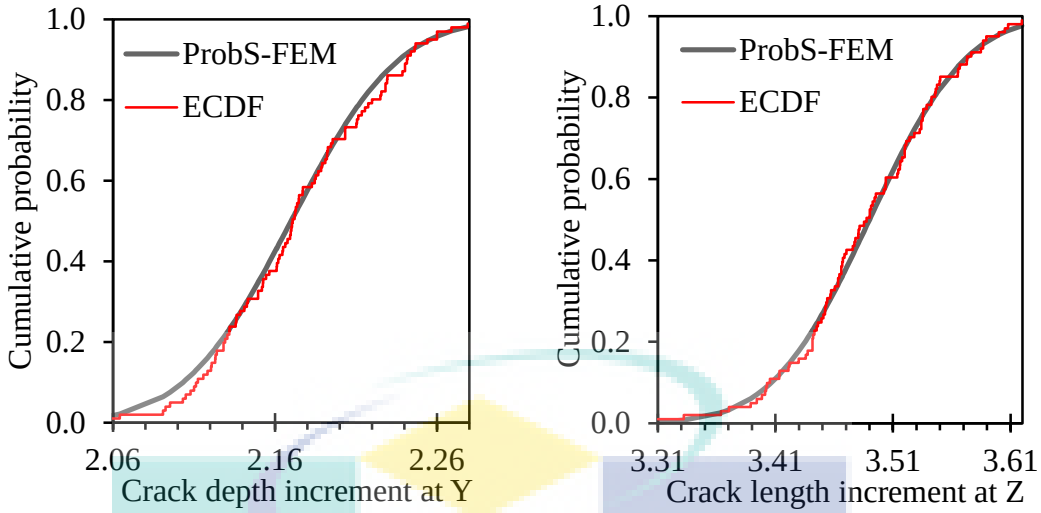

Figure 4.18 K-S test for distribution of crack depth and length

4.3.2 Multiple Surface Cracks

This section presents the results and discussion of the problem of multiple surface cracks. The aim was to emphasize the competency of the ProbS-FEM in predicting crack growth, fatigue life and SIF for problems that are more complex. In addition, the ProbS-FEM can be a tool to predict the standard deviation of initial cracks. The findings are explained as follows.

Multiple cracks were modelled using the ProbS-FEM, as shown in Figure 4.19, where two surface cracks were introduced in the middle of a four-point bending model. The sizes of the initial crack depth and length were based on the measurements in the experimental specimen. The material that was selected for this model was Aluminium 7075-T6, and the description of the material is given in Table 4.3. A cyclic load was applied to this model with a maximum load of 45 kN and a stress ratio of 0.1. Figure 4.20 shows the model for multiple crack growth in the ProbS-FEM.

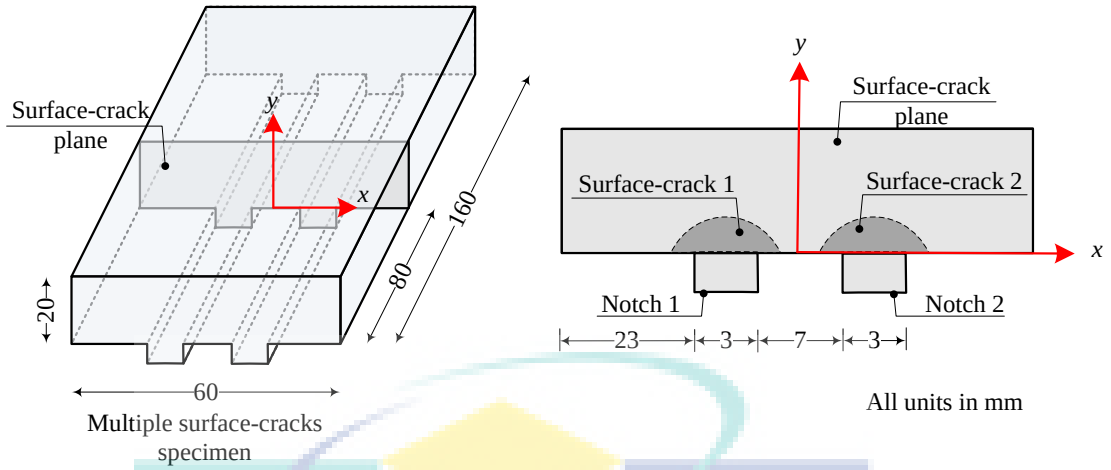

Figure 4.19 Multiple surface cracks model

The comparison between the deterministic results and the experimental data is depicted in Figure 4.21. After 60×10^3 cycles, the two cracks were combined and merged into a single surface crack. Since the mode *I* loading was applied, no crack transformation was shown perpendicular to the axis of the surface crack.

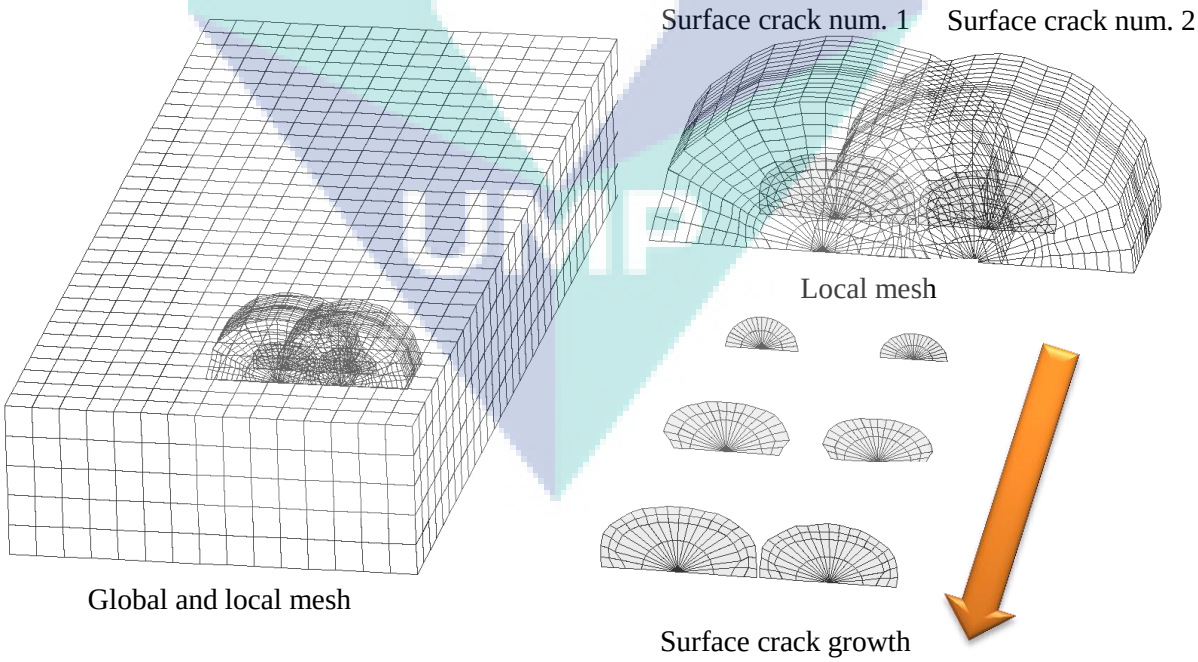

Figure 4.20 Growth of multiple surface cracks using ProbS-FEM modelling

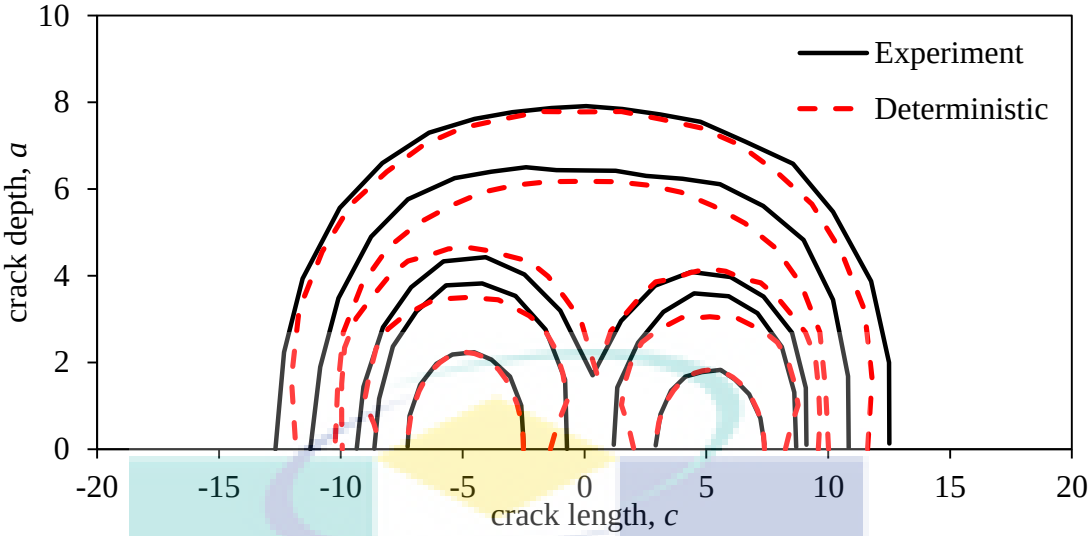

Figure 4.21 Comparison of the results between the deterministic and experimental data

An improvement in the prediction of crack growth was achieved by the ProbS-FEM, as shown in Figure 4.22. The mean of the ProbS-FEM was drawn in Figure 4.22 and it was shown to be closer to the experimental result due to the consideration of uncertainty in the crack growth increment. The crack growth increment plays an important role in the determination of the number of cycles, as shown in Eq.(3.50). Next, the calculated cycles were used to determine the crack length of the remaining nodes at the crack front. Thus, small changes in the crack growth increment influenced the crack length.

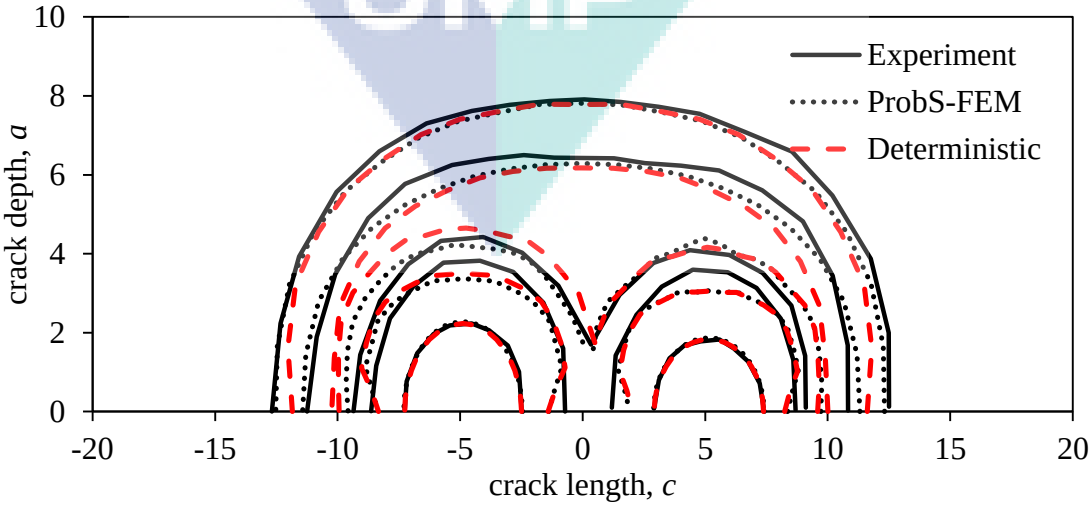

Figure 4.22 Comparison of the results between the ProbS-FEM and experimental data

Additionally, the fatigue life calculation was improved by using the ProbS-FEM. Figure 4.23 shows the verification of the fatigue life between the ProbS-FEM, the deterministic and the experimental results. There was a noticeable divergence in the deterministic results from the experimental findings. This was due to the variation in the initial crack size in the experimental work. The ProbS-FEM was using a standard deviation of 0.001 mm for the initial crack size. In order to control the randomness effect of the remaining random parameters in Table 4.3, the standard deviations were set to zero. As can be seen in Figure 4.23, the upper and lower bounds of the ProbS-FEM covered all the experimental data. The mean ProbS-FEM was closer to the experimental results compared to the deterministic results. In order to show how close the curves were, the correlation analysis was shown in Figure 4.24. The value of R^2 for the mean ProbS-FEM was higher than that of the deterministic results, thus indicating that the mean ProbS-FEM was closer than the deterministic approach. The divergences of the deterministic and ProbS-FEM results from the experimental results were due to the inadequate crack distribution, which represented the randomness of the experimental results. Thus, the value of the standard deviation for the initial crack was increased from 0.001 to 0.1.

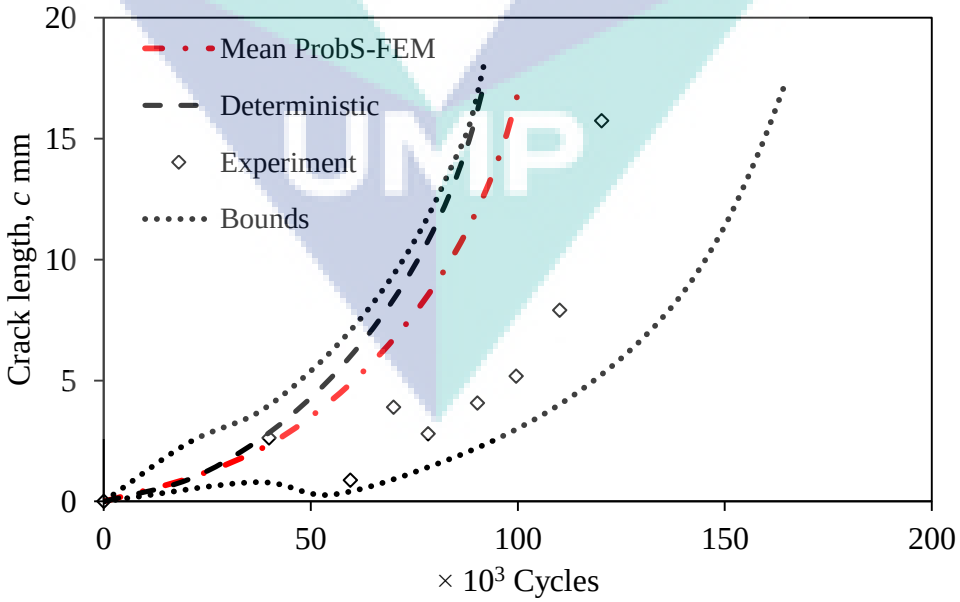

Figure 4.23 Fatigue life for multiple surface cracks problem with 0.001 mm standard deviation of the initial crack

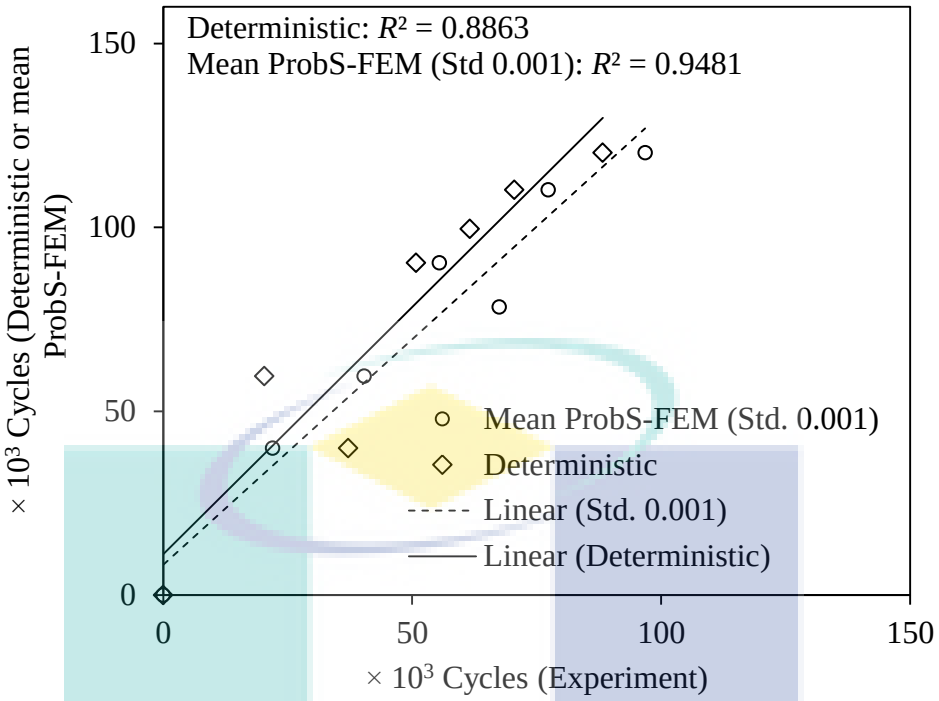

Figure 4.24 Correlation analysis of predicted cycles versus experimental cycles for 0.001 mm standard deviation of the initial crack

In order to demonstrate the effect of the initial crack size, a different value of the standard deviation of the initial crack size was implemented. Hence, in the following example, the same material properties, as shown in Table 4.3, were used with the deterministic setting, except that the standard deviation for the initial crack size was set to 0.1 mm. Figure 4.25 shows the fatigue life for an initial crack size with a standard deviation of 0.1 mm. It indicates a wider range of upper and lower bounds because of the wider distribution of the initial crack size. The mean ProbS-FEM shifted slightly towards the experimental data. In order to determine the best results that were closest to the experimental data, the correlation analysis was presented in Figure 4.26. The mean ProbS-FEM with a higher standard deviation of initial crack size computed a higher value of R^2. Thus, a suitable standard deviation for the initial crack size can be predicted through a ProbS-FEM analysis.

Figure 4.27 shows all the samples for the fatigue life of the multiple surface cracks problem with a standard deviation of 0.1 mm of the initial crack. The distribution of the crack length can be determined at different cycles or the distribution of cycles to the critical crack length can be estimated. Scientists are able

to set the critical crack length and, based on the critical crack length, the distribution of the cycle can be estimated. The cycle can be converted to the lifespan of the engineering application, depending on the number of cycles within a period. In addition, the crack length can be estimated for a certain lifespan. This process helps scientists to make decisions with regard to maintenance works. Apart from that, scientists are also keen to know the SIF at the surface crack.

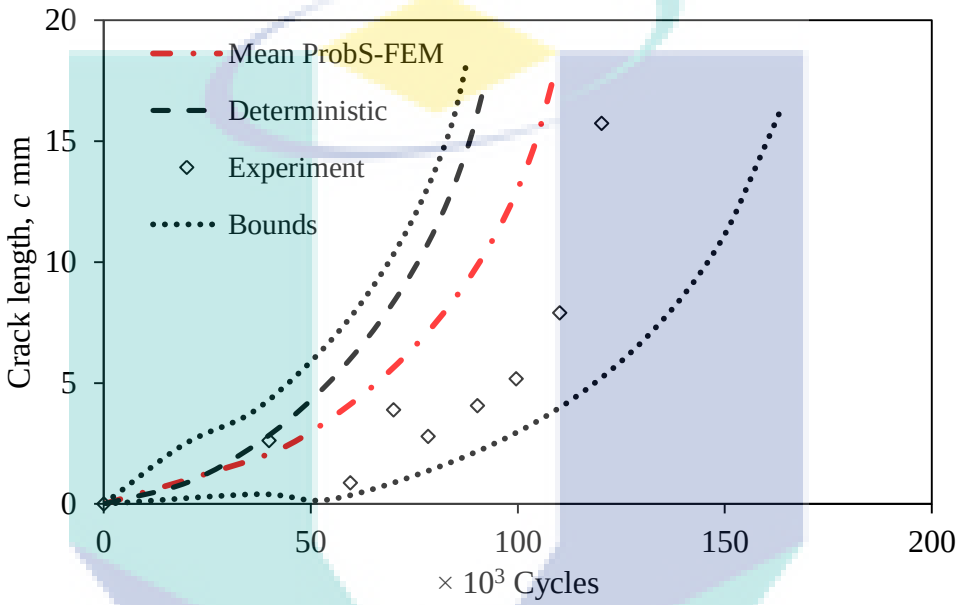

Figure 4.25 Fatigue life for multiple surface cracks problem with a standard deviation of 0.1 mm of the initial crack

The mean of the stress intensity factors for the first beach mark of two surface cracks is shown in Figure 4.28. Obviously, the stress intensity factors, K_{II} and K_{III}, were zero because no load was involved for modes *II* and *III*. The stress intensity factor, K_I, at the crack front for each surface crack is shown in the same figure. Figure 4.29 shows the mean of the stress intensity factor, K_I for the final beach mark before the specimen was fractured. The maximum K_I stress intensity factor at the final beach mark did not exceed the value of the critical stress intensity factor for Al 7075-T6. Thus, unstable crack growth occurred after the final beach mark. Since the four-point bending model was using a constant amplitude load, variations in the stress intensity factors were not noticeable. The load is the sensitive parameter in the calculation of the distribution of the values of the stress intensity factor, as shown in Eq. (3.47). Thus, in the current case, the bounds of the ProbS-FEM did not affect the SIF.

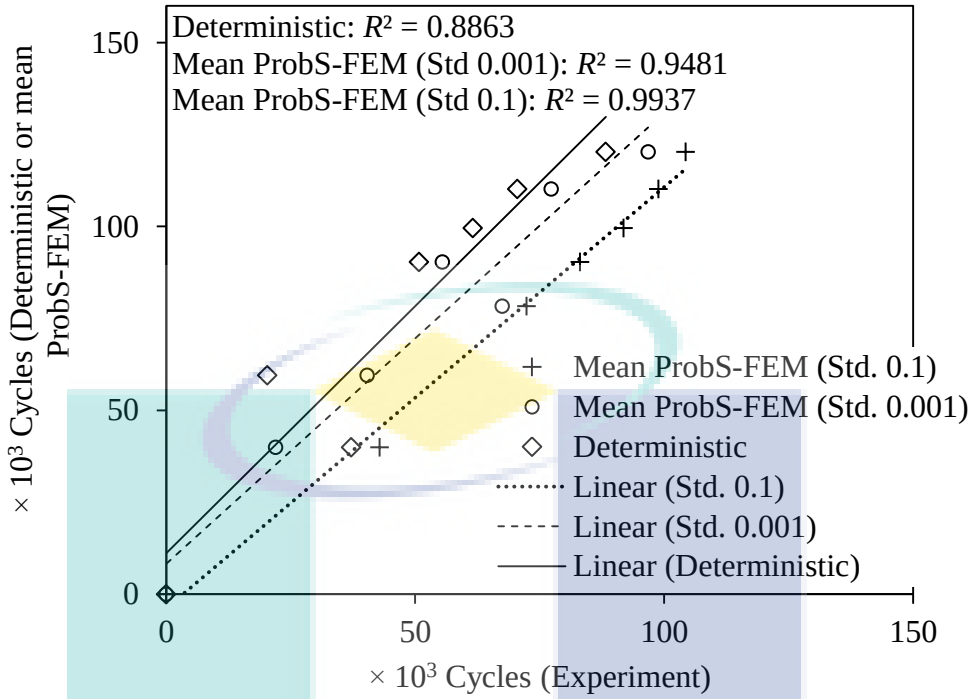

Figure 4.26 Correlation analysis of predicted cycles versus experimental cycles for standard deviations of 0.001 and 0.1 mm of the initial crack

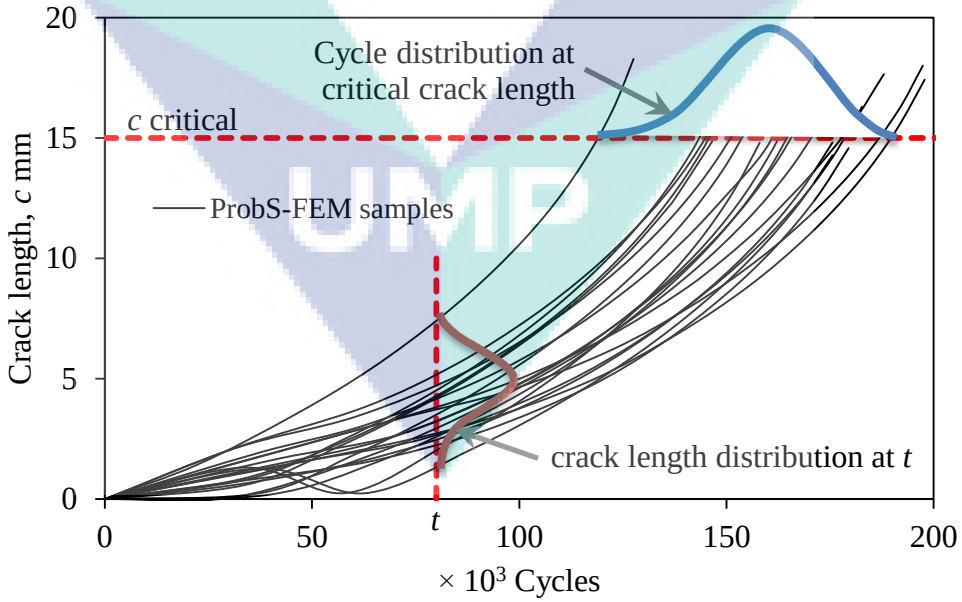

Figure 4.27 Cycle and crack length distribution from ProbS-FEM samples

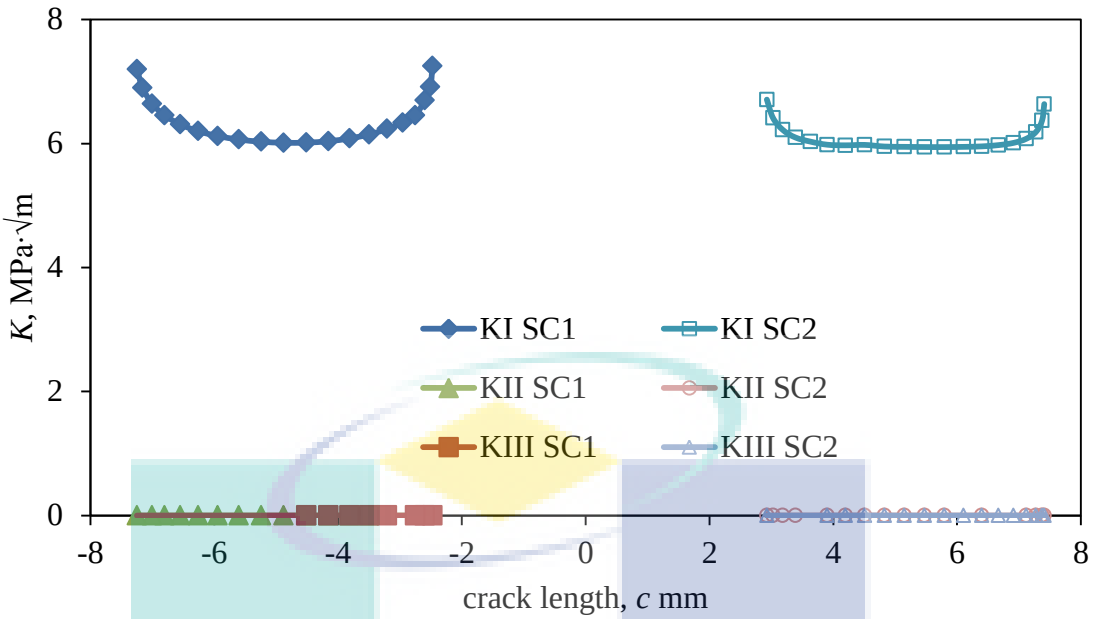

Figure 4.28 Mean of the stress intensity factors for the first beach mark of surface crack numbers one (SC1) and two (SC2)

4.3.3 Sample Reduction in the ProbS-FEM

The accuracy of the new combination of the two analyses of the so-called ProbS-FEM was based on the sampling strategy. Two sampling strategies, the MCS and LHS, were developed in the ProbS-FEM. These two sampling strategies offered an alternative approach that catered to the uncertainty in the analysis (Helton & Davis, 2003; Patelli et al., 2012). The MCS and LHS results were compared to analyse the efficiency of each sampling method. The end result of the ProbS-FEM was to obtain the probability of failure with the optimum time and iterations. The efficiency of the ProbS-FEM is demonstrated and discussed in this section.

The LHS and MCS generated random parameters from random numbers, as explained in the methodology section. Since the initial crack length, a_i, is one of the major factors that contribute to the randomness in the fatigue fracture, the generation of the initial crack length is presented in this section. Five thousand samples of initial crack lengths were generated according to the Gaussian distribution with a mean of 4.5 mm and a standard deviation of 0.1. As the mean was 4.5 mm, the frequency for the range that covered the mean value was expected to be the highest.

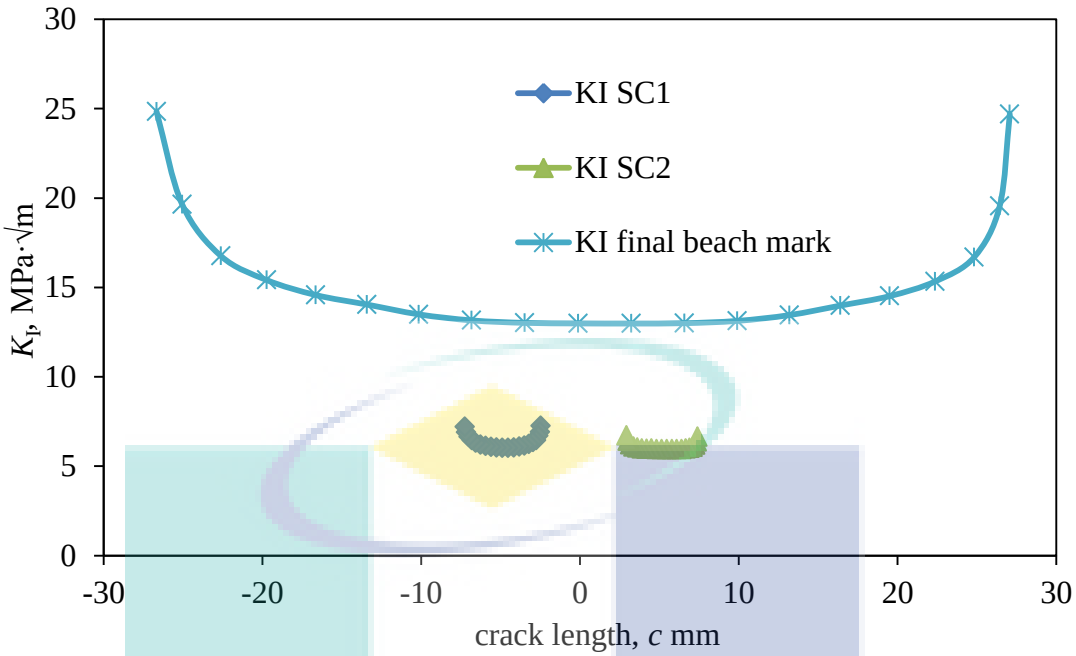

Figure 4.29 Mean of K_I stress intensity factors for the first and final beach marks

Figure 4.30 shows the quantification for the uncertainty of the crack length from the ProbS-FEM code using the LHS and MCS sampling methods. The LHS method showed well-generated random parameters. The frequency increased slightly before the mean value, as shown in Figure 4.30. After the mean value, the frequency decreased slightly as the generation reached the end of the distribution. The MCS generated the same trend as the LHS, but the peaks of the probability distribution were slightly different. The LHS provided a denser frequency at the mean, while the MCS generated a higher frequency at the shoulder of the distribution. The higher frequency at the shoulder of the distribution happened due to the unstructured random numbers that were generated around the mean value. The LHS provided a structured random number generation along the CDF. It contributed to the smooth frequency generated in the PDF. From this perspective, the LHS generates better random parameters.

In addition, the LHS covers a wider distribution. In this example, the LHS covered a distribution ranging from 4.16 to 4.86, while the MCS covered from 4.19 to 4.81. The LHS provided a wider coverage, especially at the tail of the distribution. The samples at the tail of the distribution can represent the extreme condition of the parameter. It was essential to simulate the extreme condition since it can contribute to

the failure of a structure. The upper and lower bounds as well were affected by the samples at the tail of the distribution. Therefore, the samples at the tail of the distribution were initiated by the portion of generated random numbers. By using the LHS technique, every range of the CDF was divided into portions. A sample was generated for every portion, thus producing a wider coverage. The MCS used a random number generator with an uncontrolled technique. Therefore, a denser frequency was generated at the shoulder of the distribution. This reflected the maximum frequency reached by the mean range. The highest frequency generated by the LHS was 695, while the MCS generated a frequency that was less than 624 for the mean range.

Figure 4.31 shows the convergence of the mean and standard deviation for the generated parameter. The mean of the generated parameter was compared for the LHS and MCS, as in Figure 4.31(a). The iteration was classed into seven different groups, namely 50, 100, 200, 300, 500, 1000 and 5000. An iteration of 50 meant that 50 samples were used for this group, while an iteration of 1000 consisted of the generation of 1000 samples for that group. Once the number of samples was sufficient in each of the iterations, the mean of the generated parameter was calculated.

Since the initial crack length was generated for a mean of 4.5, it was necessary for each iteration to provide a mean value that was as close as possible to 4.5. The mean was calculated and compared for the LHS and MCS, as in Figure 4.31(a). The mean for the LHS was more stable since each of the iterations provided a difference of less than 0.005 from the targeted mean value. The mean value generated by the LHS decreased slightly from 4.504 as the number of iterations was increased. The MCS started with a difference of 0.001 from the targeted mean, and then suddenly increased to 4.509. There was a slight decrease in the difference as the number of iterations increased. The MCS needed a longer time and more iterations to generate a stable mean. The MCS created the input distribution through sampling with enough iterations. However, a problem with clustering arose when a small number of iterations were performed, as shown for 100 iterations in Figure 4.31(a).

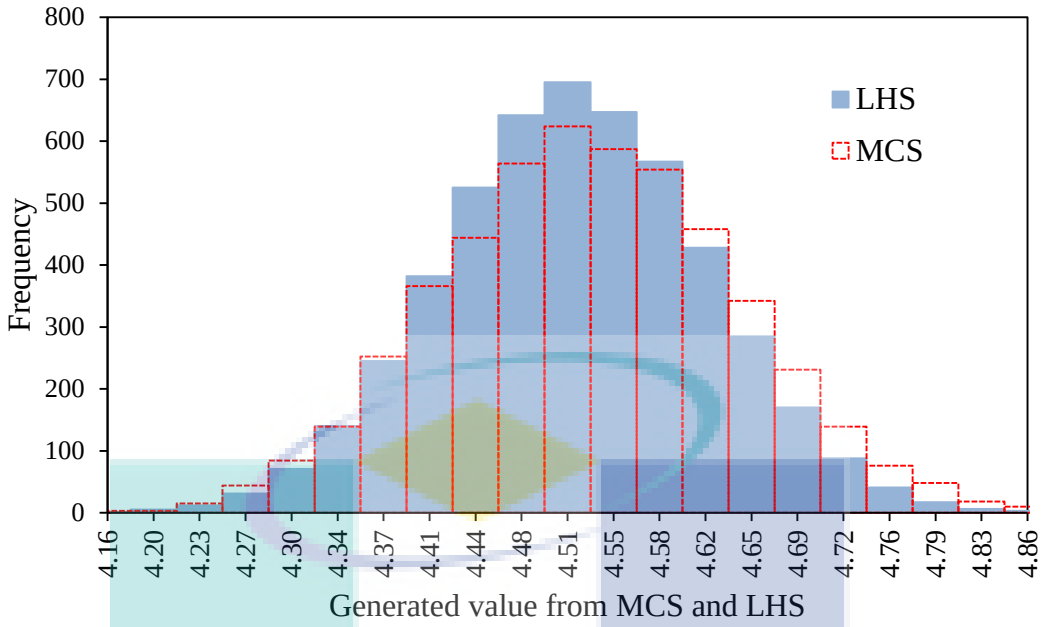

Figure 4.30 Quantification of uncertainty for values generated by MCS and LHS

Figure 4.31 (b) shows the standard deviation generated for the LHS and MCS with various numbers of iterations. As the standard deviation for the initial crack length was 0.100, it was essential for the LHS and MCS to generate a standard deviation that was as close as possible to the targeted standard deviation. The LHS was shown to be a more stable generator of the standard deviation than the MCS as the number of iterations was increased. The standard deviation for the MCS was unstable since it started at the same level with the LHS and then deviated from the targeted standard deviation (written as Targeted Std. in Figure 4.31(b)) at iterations 200 until 500. This shows that the accuracy of the MCS in the generation of random parameters is questionable. The MCS was dependent on the randomness of the pseudo-random numbers, and the hits surrounding the mean value had higher chances due to the random numbers transferred to the CDF. Therefore, the accuracy of the standard deviation deviated from the targeted value.

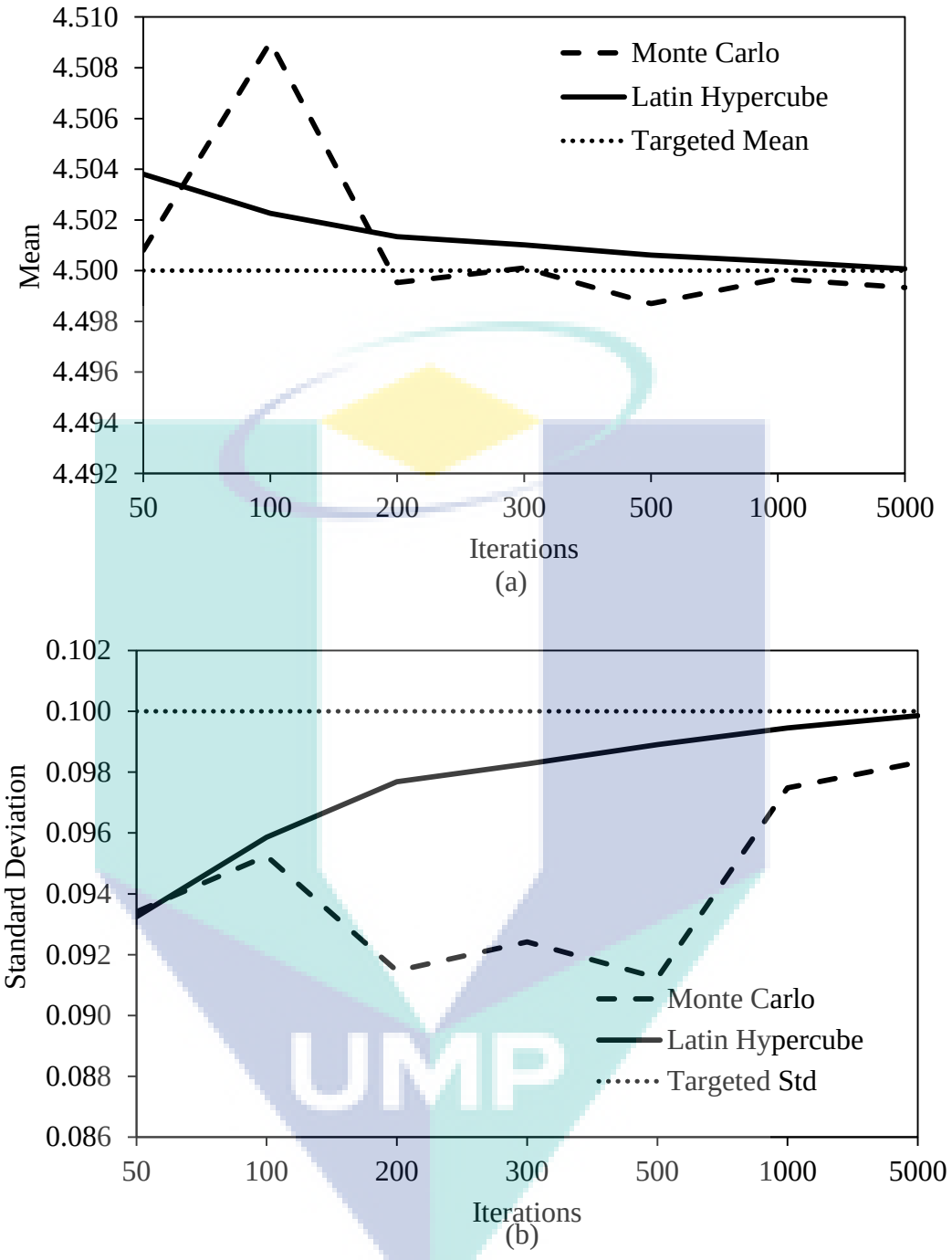

Figure 4.31 Stability of the generated (a) mean and (b) standard deviation of the LHS and MCS

The consistency of the sampling method in producing values that were closer to the theoretical ones is shown in Figure 4.32. Seven separate simulations for the MCS and LHS were conducted with various numbers of iterations. The simulation was repeated ten times, and the mean and standard deviation of the results were

presented. The standard deviation of the generated means and the generated standard deviations were plotted against the iterations.

The consistency of the generated value was measured against the value of the standard deviation. As the standard deviation deviated to zero, it meant that the sampling method produced values that were consistent with the theoretical values. Figure 4.32 shows that the LHS produced values that were more consistent compared to the MCS. This was because the portions in the LHS created a stage for the generation of values, even for a lesser number of iterations. The LHS computed a lesser value of standard deviation at 50 iterations due to the sampling strategy. The LHS generated portions to divide the distribution, and distributed the samples for the whole distribution evenly. Even though each iteration was repeated ten times, the LHS strategy still produced a better consistency. At 50 iterations, the generation deviated 0.001 from each of the iterations for both the generated mean and the standard deviation. This showed that the LHS is feasible for simulating a model with a small number of iterations.

The MCS was incapable of doing so since it needed iterations of up to 5000 for the generated mean and standard deviation to reach a standard deviation of zero. This is because the MCS generates values randomly within a distribution and thus, it needs more samples to cover all the distributions. A small number of iterations are insufficient for the MCS to cover the distribution. As a result, the MCS produced an inconsistent mean value, as shown in Figure 4.32(a). The standard deviation of the generated means for the MCS increased after reaching zero for 300 iterations. If supposing the standard deviation value was maintained at zero, and more iterations were generated until 500, 1000 and 5000 iterations, then, due to the unstructured generation of the random values, the deviation between the set of samples of 500 iterations would increase slightly. Figure 4.32(b) shows that the iterations for the MCS produced the fluctuated value of the standard deviation. Therefore, the LHS is capable of producing consistent random values with less number of iterations.

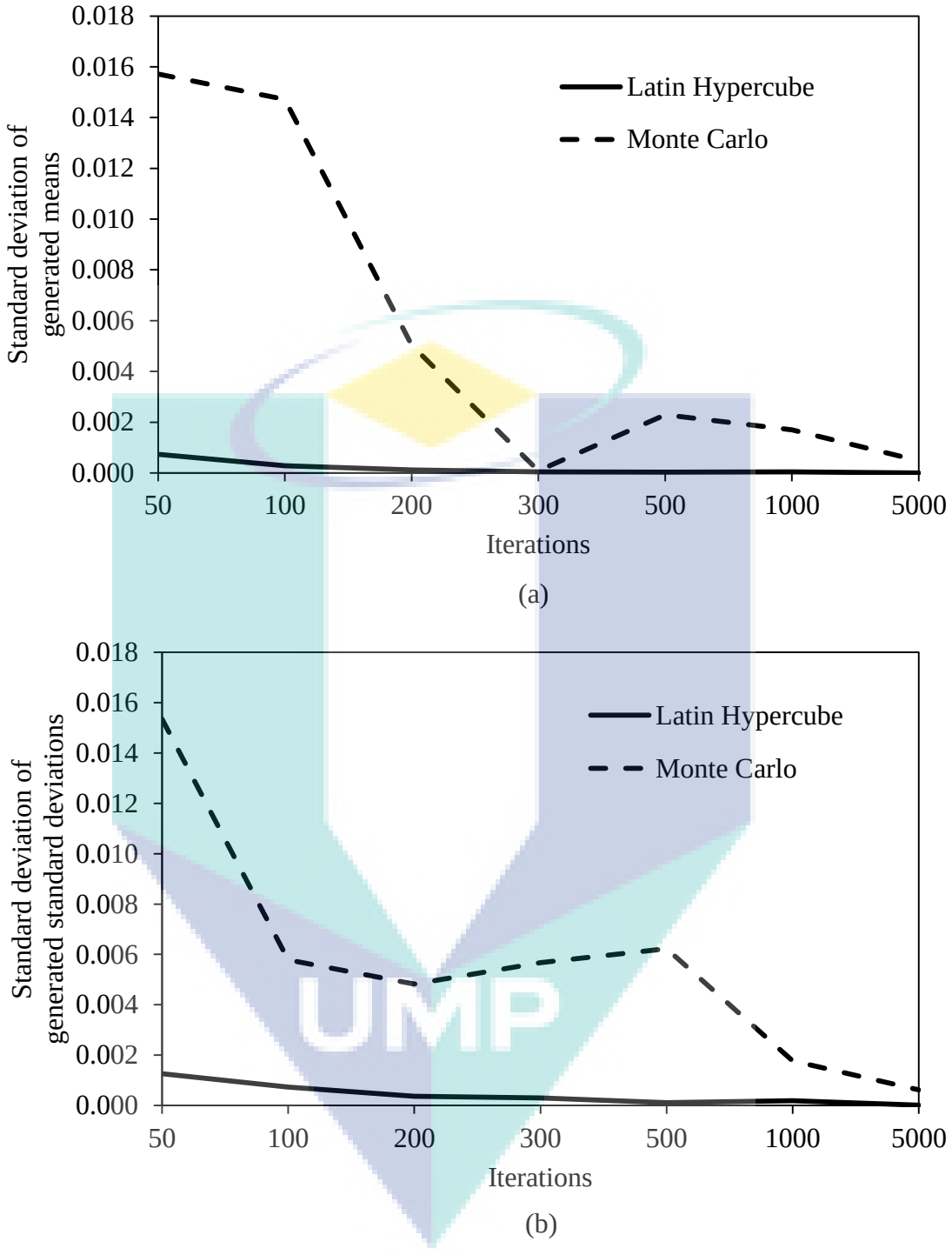

Figure 4.32 Standard deviation of generated (a) means and (b) standard deviation

The LHS was the preferred sampling strategy for the analysis of fatigue surface crack growth. The LHS generated a wider coverage of distribution and higher frequency at the mean of the initial surface crack. In addition, the LHS computed a stable mean and standard deviation value with less number of iterations. In addition to

the consistency of the generated value, the LHS was capable of producing consistent random values in comparison to the MCS. The embedded sampling strategy in the ProbS-FEM was capable of obtaining the probability of failure with the optimum time and number of iterations. The iteration time for the LHS was reduced by 20%.

4.4 SUMMARY

Overall, the ProbS-FEM was developed to consider the uncertainties in the analysis. The verification of the developed code was presented to show the capability of the ProbS-FEM in predicting the SIF, the crack growth for different modes of loading, and the fatigue life distribution. Single and multiple surface cracks were simulated to indicate the level of complexity that could be solved by the ProbS-FEM. The new understanding of the SIF, crack growth and fatigue life distribution, particularly for the case of single and multiple surface cracks, have been discussed. The integrity of the components could be observed through the ProbS-FEM analysis. The ProbS-FEM produced a range of outputs because of the existence of uncertainty in the material properties and the crack initiation. The new contribution has improved the previous solution model that mostly revealed the static or deterministic results only. The range of outputs produced in the ProbS-FEM provided a remedy for stray deterministic predictions, particularly in fatigue behaviour. Computationally, the application of the probabilistic approach by the developed algorithm contributed to the enhancement of the S-FEM compared to the previous approach.

The major finding was the modelling of the uncertainties feature in the FEA for the application of the fatigue crack problem. The introduction of uncertainties in the analysis successfully defined the improvement in the prediction of the SIF, crack growth and fatigue life. Thus, the results will help scientists to make decisions regarding future maintenance and inspection strategies, as well as on the appropriate remedial actions to be taken following the inspection results. Therefore, the proper priority will be given to maintenance with the ProbS-FEM.

Even though the current research has focused on a constant amplitude loading and the basic fatigue crack growth model (Paris' law), the ProbS-FEM can be further developed for a more complex loading and fatigue crack growth model.

CHAPTER V

CONCLUSIONS

5.1 INTRODUCTION

The main objective of this thesis was to develop, test and provide a computational fracture mechanics model that emphasizes the quantification of uncertainties for surface cracks. It can be concluded that this objective has been successfully achieved. The uncertainties element in real engineering applications was adopted in the current advanced FEM analysis. The ProbS-FEM was introduced and it successfully solved the problem of the randomness of variables. This chapter presents the conclusions drawn from the abovementioned investigations and suggestions for future work.

5.2 CONCLUSIONS

Based on the research findings, the research objectives have been achieved, and the main conclusions are summarized as below:

(i) In the present study, the mathematical model for the distribution of surface crack growth has been successfully represented by a Gaussian model with a certain value of the mean and standard deviation. The mathematical model has shown an acceptable range of agreement via a K-S statistical test evaluation. The dispersion of a set of input data, particularly for the initial surface crack size and material properties in the ProbS-FEM, led to the development of the surface crack distribution. The distribution of fatigue life was also successfully addressed by the standard deviation of the initial surface crack. The developed model for crack growth distribution, taking into account the randomness of the

initial surface crack and the material properties, indicated the achievement of research objective (i).

(ii) An effective algorithmic solution for the ProbS-FEM was developed in this research. It was demonstrated by the bounds of the ProbS-FEM, which showed better predictions in dealing with randomness outputs. The standard deviation of the initial surface crack size influenced the prediction accuracy of the mean ProbS-FEM. The effectiveness of the ProbS-FEM was enhanced with the implementation of the Latin Hypercube Sampling. An effective algorithmic solution was presented for the ProbS-FEM to reduce the number of samples and the iteration time.

(iii) An extension of the S-version of the Finite Element Model for surface cracks was successfully shown. The ProbS-FEM was introduced to solve the existence of the uncertainties element in real applications for finite element analysis. The ProbS-FEM successfully modelled the material and geometrical uncertainties, as proven by the results, which were in agreement with the experimental findings.

(iv) The uncertainties that have been ignored in deterministic finite element codes can lead to conservative results with regard to the SIF, crack growth, failure prediction and fatigue life. The SIF was analysed and validated by deterministic and experimental methods, and the results were the same. The verification of the crack growth and fatigue life showed a small degree of dispersion of the results from the experimental results. The dispersion was influenced by not only the material properties but also by the initial crack size. The mean and bounds produced by the ProbS-FEM showed that there was an enhancement in the prediction of crack growth and fatigue life.

5.3 KNOWLEDGE CONTRIBUTION

The results-based contribution by the ProbS-FEM has been presented implicitly and explicitly in the Results and Discussion section. In short, the study has successfully contributed to knowledge in the following aspects:

(i) A new probabilistic model for the S-FEM: In this study, the uncertainty issue in relation to the SIF, surface crack growth and fatigue life of surface cracks was examined. A newly embedded probabilistic model with the S-FEM, called the ProbS-FEM, was proposed. This is the current advanced S-FEM version that combines the probabilistic analysis in the S-FEM.

(ii) Formulation of uncertainties feature in the analysis: The introduction of uncertainties in the numerical formulations has successfully defined the improvements in the prediction of the SIF, surface crack growth and fatigue life by modelling the dispersion of the initial surface crack. The mean and the upper and lower bounds indicate the improvements.

(iii) Methodological contribution: The accurate determination of the distribution of surface crack growth is problematic when a three-dimensional surface crack growth is involved due to the repetition of the re-meshing and sampling process. Therefore, the ProbS-FEM is a new numerical model for defining the methodological algorithm based on the S-FEM technique. So far, the probabilistic analysis has been used for the FEM, but not for the S-FEM, as provided in this study. No researcher has produced an embedded probabilistic analysis with the S-FEM, particularly for a three-dimensional analysis.

(iv) Practical contribution to the ProbS-FEM codes: The deterministic S-FEM was presented with the exception of a probabilistic element. With the proposed ProbS-FEM model, the outcomes may lead to a proper improvement of the S-FEM codes in an effort to include the uncertainties element in assessing industrial flaws and defects.

5.4 SUGGESTIONS FOR FURTHER WORK

The work that has been carried out provides several promising avenues for further probabilistic surface crack researches as follows:

(i) The dispersion of the presented initial surface crack size was limited to the standard deviation approach. Thus, a study on a new methodology to calculate the equivalent initial flaw size distribution is highly encouraged. The initial flaw size distribution should be determined to confirm the changes in the fatigue life results.

(ii) The variable amplitude loading for mode *I* and *II* with the same geometrical model should be conducted to assess the change in the mixed mode fracture, and the dominant mode can be determined. In addition, it is essential to consider the introduction of a variable amplitude load in the ProbS-FEM. The variable amplitude load exposes the scatter input in an analysis.

(iii) The present study dealt with a continuum scale level. The study on a microstructural scale level is advisable because at microstructural level, high sensitivity is shown towards different loading modes, such as uniaxial with and without mean stress, torsion and equibiaxial tension. The probabilistic modelling of fatigue in relation to the microstructural level would be one of the choices to embark on.

(iv) One of the challenges in the implementation is the unpredictable environment. One example is the working or operational environment which is exposed to uncertain loading. In addition, the temperature and corrosion contribute to the unpredictable operational environment. Nevertheless, the simulation of real engineering environments will increase the commercial value of the ProbS-FEM.

REFERENCES

Aguilarespinosa, A. A., Fellows, N. A. & Durodola, J. F. 2013. Experimental Measurement of Crack Opening and Closure Loads for 6082-T6 Aluminium Subjected to Periodic Single and Block Overloads and Underloads. *International Journal of Fatigue* 47: 71-82.

Akramin, M. R. M. 2008. Analisis Kegagalan Struktur Retak Menggunakan Kaedah Hibrid Unsur Terhingga Dan Monte Carlo. Master Thesis, Department of Mechanical & Materials Engineering, Universiti Kebangsaan Malaysia [in Malaysian].

Anderson, T. L. 2005. *Fracture Mechanics: Fundamentals and Applications*. 3rd. Boca Raton: Taylor & Francis Group,CRC.

Angioni, S. L., Visrolia, A. & Meo, M. 2012. Combining X-Fem and a Multilevel Mesh Superposition Method for the Analysis of Thick Composite Structures. *Composites Part B: Engineering* 43: 559-568.

ASTM E740-03. 2008. *Standard Practice for Fracture Testing with Surface-Crack Tension Specimens*, Section 3. West Conshohocken, USA.

Barker, V. M., Steven Johnson, W., Adair, B. S., Antolovich, S. D. & Staroselsky, A. 2013. Load and Temperature Interaction Modeling of Fatigue Crack Growth in a Ni-Base Superalloy. *International Journal of Fatigue* 52: 95-105.

Beden, S. M. 2010. Assessment of Fatigue Crack Growth under Variable Amplitude Loading. PhD Thesis, Mechanical and Materials Department, Faculty of Engineering and Built Environment, Universiti Kebangsaan Malaysia.

Beden, S. M., Abdullah, S. & Ariffin, A. K. 2009. Review of Fatigue Crack Propagation Models for Metallic Components. In. (edit.). *European Journal of Scientific Research*, 28. pp. 364-397. EuroJournals Publishing, Inc.

Beer, M. & Liebscher, M. 2008. Designing Robust Structures – a Nonlinear Simulation Based Approach. *Computers & Structures* 86: 1102-1122.

Berer, M. & Pinter, G. 2013. Determination of Crack Growth Kinetics in Non-Reinforced Semi-Crystalline Thermoplastics Using the Linear Elastic Fracture Mechanics (Lefm) Approach. *Polymer Testing* 32: 870-879.

Brighenti, R. 2001. External Longitudinal Flaws in Pipes under Complex Loading. *Journal of Pressure Vessel Technology, Transactions of the ASME* 123: 139-145.

Brighenti, R. & Carpinteri, A. 2013. Surface Cracks in Fatigued Structural Components: A Review. *Fatigue and Fracture of Engineering Materials and Structures* 36: 1209-1222.

Broek, D. 1986. *Elementary Engineering Fracture Mechanics*. AD Dordrecht, The Netherlands: Kluwer Academic Publishers.

Cai, T., Wang, S. & Xu, Q. 2015. Monte Carlo Optimization for Site Selection of New Chemical Plants. *Journal of Environmental Management* 163: 28-38.

Cai, Y., Han, L., Tian, L. & Zhang, L. 2016. Meshless Method Based on Shepard Function and Partition of Unity for Two-Dimensional Crack Problems. *Engineering Analysis with Boundary Elements* 65: 126-135.

Carpinteri, A. 1993. Shape Change of Surface Cracks in Round Bars under Cyclic Axial Loading. *International Journal of Fatigue* 15: 21-26.

Carpinteri, A., Brighenti, R. & Vantadori, S. 2009. Notched Double-Curvature Shells with Cracks under Pulsating Internal Pressure. *International Journal of Pressure Vessels and Piping* 86: 443-453.

Carpinteri, A., Ronchei, C. & Vantadori, S. 2013. Stress Intensity Factors and Fatigue Growth of Surface Cracks in Notched Shells and Round Bars: Two Decades of Research Work. *Fatigue and Fracture of Engineering Materials and Structures* 36: 1164-1177.

Carpinteri, A. & Vantadori, S. 2009. Sickle-Shaped Cracks in Metallic Round Bars under Cyclic Eccentric Axial Loading. *International Journal of Fatigue* 31: 759-765.

Carpinteri, A. & Vantadori, S. 2009. Sickle-Shaped Surface Crack in a Notched Round Bar under Cyclic Tension and Bending. *Fatigue and Fracture of Engineering Materials and Structures* 32: 223-232.

Cendõn, D. A., Torabi, A. R. & Elices, M. 2015. Fracture Assessment of Graphite V-Notched and U-Notched Specimens by Using the Cohesive Crack Model. *Fatigue and Fracture of Engineering Materials and Structures* 38: 563-573.

Cetin, A., Härkegård, G. & Naess, A. 2013. The Fatigue Limit: An Analytical Solution to a Monte Carlo Problem. *International Journal of Fatigue* 55: 194-201.

Choi, S., Grandhi, R. V. & Canfield, R. A. 2007. *Reliability-Based Structural Design*. 1st. London: Springer.

Chowdhury, M. S., Song, C. & Gao, W. 2014. Probabilistic Fracture Mechanics with Uncertainty in Crack Size and Orientation Using the Scaled Boundary Finite Element Method. *Computers & Structures* 137: 93-103.

Daud, R. 2012. Analysis of Elastic Interacting Cracks in Finite Body. PhD Thesis, Department of Mechanical & Materials Engineering, Universiti Kebangsaan Malaysia.

De Matos, P. F. P. & Nowell, D. 2009. Experimental and Numerical Investigation of Thickness Effects in Plasticity-Induced Fatigue Crack Closure. *International Journal of Fatigue* 31: 1795-1804.

Dong, Y., He, X., Xue, D. & Liu, W. 2015. Sif Solution for a Single Hole-Edge Crack in a Finite Plate with Clamped Ends. *Yingyong Lixue Xuebao/Chinese Journal of Applied Mechanics* 32: 187-191.

Doshi, K. & Vhanmane, S. 2013. Probabilistic Fracture Mechanics Based Fatigue Evaluation of Ship Structural Details. *Ocean Engineering* 61: 26-38.

Dowling, N. E. 1999. *Mechanical Behavior of Materials*. 2nd Edition. Prentice Hall.

Dugdale, D. S. 1960. Yielding of Steel Sheets Containing Slits. *J. Mech. Phys. Solids* 8: 100.

Duquesnay, D. L. & Underhill, P. R. 2010. Fatigue Life Scatter in 7xxx Series Aluminum Alloys. *International Journal of Fatigue* 32: 398-402.

El-Zeghayar, M., Topper, T. H., Conle, F. A. & Bonnen, J. J. F. 2011. Modeling Crack Closure and Damage in Variable Amplitude Fatigue Using Smooth Specimen Fatigue Test Data. *International Journal of Fatigue* 33: 223-231.

Elishakoff, I. & Ren, Y. 1999. The Bird's Eye View on Finite Element Method for Structures with Large Stochastic Variations. *Computer Methods in Applied Mechanics and Engineering* 168: 51-61.

Emery, J. M., Hochhalter, J. D., Wawrzynek, P. A., Heber, G. & Ingraffea, A. R. 2009. Ddsim: A Hierarchical, Probabilistic, Multiscale Damage and Durability Simulation System – Part I: Methodology and Level I. *Engineering Fracture Mechanics* 76: 1500-1530.

Estecahandy, M., Bordes, L., Collas, S. & Paroissin, C. 2015. Some Acceleration Methods for Monte Carlo Simulation of Rare Events. *Reliability Engineering & System Safety* 144: 296-310.

Feng, Z., Mao, K., Zou, T. & Yang, Y. 2014. Discussion on Airworthiness Requirement of Widespread Fatigue Damage – Safe-Life Methodology or Damage-Tolerance Methodology. *Procedia Engineering* 80: 392-398.

Fish, J. 1992. The S-Version of the Finite Element Method. *Computers & Structures* 43: 539-547.

Forth, S. C., Everett, R. A. & Newman, J. A. 2002. A Novel Approach to Rotorcraft Damage Tolerance. *6th joint FAA/DoD/NASA aging aircraft conference*, pp. 1-18.

Freedman, D. A. 2009. Statistical Models: *Theory and Practice,* Cambridge: Cambridge University Press.

Gdoutos, E. E. 2005. Fracture Mechanics: *An Introduction,* Vol. 123. Dordrecht: Springer Netherlands.

Grell, W. A. & Laz, P. J. 2010. Probabilistic Fatigue Life Prediction Using Afgrow and Accounting for Material Variability. *International Journal of Fatigue* 32: 1042-1049.

Haldar, A. & Mahadevan, S. 2000. *Probability, Reliability, and Statistical Method in Engineering Design*. John Wiley & Sons, Inc.

Hariharan, M., Yaacob, S. & Awang, S. A. 2011. Pathological Infant Cry Analysis Using Wavelet Packet Transform and Probabilistic Neural Network. *Expert Systems with Applications* 38: 15377-15382.

Helton, J. C. & Davis, F. J. 2003. Latin Hypercube Sampling and the Propagation of Uncertainty in Analyses of Complex Systems. *Reliability Engineering & System Safety* 81: 23-69.

Hou, C.-Y. 2011. Simulation of Surface Crack Shape Evolution Using the Finite Element Technique and Considering the Crack Closure Effects. *International Journal of Fatigue* 33: 719-726.

Huang, W., Wang, T.-J., Garbatov, Y. & Guedes Soares, C. 2012. Fatigue Reliability Assessment of Riveted Lap Joint of Aircraft Structures. *International Journal of Fatigue* 43: 54-61.

Iranpour, M., Taheri, F. & Vandiver, J. K. 2008. Structural Life Assessment of Oil and Gas Risers under Vortex-Induced Vibration. *Marine Structures* 21: 353-373.

Irwin, G. R. 1957. Analysis of Stresses and Strains near the End of a Crack Traversing a Plate. *J. Appl. Mech.* 24: 361.

Iyyer, N., Sarkar, S., Merrill, R. & Phan, N. 2007. Aircraft Life Management Using Crack Initiation and Crack Growth Models – P-3c Aircraft Experience. *International Journal of Fatigue* 29: 1584-1607.

Janssen, H. 2013. Monte-Carlo Based Uncertainty Analysis: Sampling Efficiency and Sampling Convergence. *Reliability Engineering & System Safety* 109: 123-132.

Johan Singh, P., Mukhopadhyay, C. K., Jayakumar, T., Mannan, S. L. & Raj, B. 2007. Understanding Fatigue Crack Propagation in Aisi 316 (N) Weld Using Elber's Crack Closure Concept: Experimental Results from Gcmod and Acoustic Emission Techniques. *International Journal of Fatigue* 29: 2170-2179.

Kaczor, G., Młynarski, S. & Szkoda, M. 2016. Verification of Safety Integrity Level with the Application of Monte Carlo Simulation and Reliability Block Diagrams. *Journal of Loss Prevention in the Process Industries* 41: 31-39.

Kapoor, R., Rao, V. S. H., Mishra, R. S., Baumann, J. A. & Grant, G. 2011. Probabilistic Fatigue Life Prediction Model for Alloys with Defects: Applied to A206. *Acta Materialia* 59: 3447-3462.

Khan, S. U., Alderliesten, R. C., Rans, C. D. & Benedictus, R. 2010. Application of a Modified Wheeler Model to Predict Fatigue Crack Growth in Fibre Metal Laminates under Variable Amplitude Loading. *Engineering Fracture Mechanics* 77: 1400-1416.

Kikuchi, M., Maitireymu, M. & Sano, H. 2010. Study on Fatigue Crack Growth Criterion 1st Report, Paris' Law of a Surface Crack under Pure Mode I Loading. *Nihon Kikai Gakkai Ronbunshu, A Hen/Transactions of the Japan Society of Mechanical Engineers, Part A* 76: 516-522.

Kikuchi, M., Wada, Y., Maitireyimu, M. & Sano, H. 2010. Closure Effect on Interaction of Two Surface Cracks under Cyclic Bending. *American Society of Mechanical Engineers, Pressure Vessels and Piping Division*, pp. 415-421.

Kikuchi, M., Wada, Y., Shimizu, Y. & Li, Y. 2012. Crack Growth Analysis in a Weld-Heat-Affected Zone Using S-Version Fem. *International Journal of Pressure Vessels and Piping* 90–91: 2-8.

Kikuchi, M., Wada, Y., Shimizu, Y. & Yulong, L. 2010. Crack Growth Analysis in Weld-Heat Affected Zone Using S-Version Fem. *American Society of Mechanical Engineers, Pressure Vessels and Piping Division*, pp. 401-406.

Kikuchi, M., Wada, Y., Shintaku, Y., Suga, K. & Li, Y. 2014. Fatigue Crack Growth Simulation in Heterogeneous Material Using S-Version Fem. *International Journal of Fatigue* 58: 47-55.

Kikuchi, M., Wada, Y., Shmizu, Y. & Li, Y. 2011. Stress Corrosion Cracking Analysis under Thermal Residual Stress Field Using S-Fem. *Key Engineering Materials* 462-463: 431-436.

Kikuchi, M., Wada, Y. & Suga, K. 2011. Surface Crack Growth Simulation under Mixed Mode Cyclic Loading Condition. *Procedia Engineering* 10: 427-432.

Kim, C.-Y., Choi, J.-M. & Song, J.-H. 2013. Fatigue Crack Growth and Closure Behavior under Random Loadings in 7475-T7351 Aluminum Alloy. *International Journal of Fatigue* 47: 196-204.

Kim, J.-S., An, D.-H., Lee, S.-Y. & Lee, B.-Y. 2009. A Failure Analysis of Fillet Joint Cracking in an Oil Storage Tank. *Journal of Loss Prevention in the Process Industries* 22: 845-849.

Kim, J., Zi, G., Van, S. N., Jeong, M., Kong, J. & Kim, M. 2011. Fatigue Life Prediction of Multiple Site Damage Based on Probabilistic Equivalent Initial Flaw Model. *Structural Engineering and Mechanics* 38: 443-457.

Kim, W., Lee, H. C., Pyeon, C. H., Shin, H. C. & Lee, D. 2016. Monte Carlo Analysis of the Accelerator-Driven System at Kyoto University Research Reactor Institute. *Nuclear Engineering and Technology* 48: 304-317.

Kimoto, K. & Ichikawa, Y. 2015. A Finite Difference Method for Elastic Wave Scattering by a Planar Crack with Contacting Faces. *Wave Motion* 52: 120-137.

Larrosa, N. O., Navarro, A. & Chaves, V. 2015. Calculating Fatigue Limits of Notched Components of Arbitrary Size and Shape with Cracks Growing in Mode I. *International Journal of Fatigue* 74: 142-155.

Leander, J., Aygül, M. & Norlin, B. 2013. Refined Fatigue Assessment of Joints with Welded in-Plane Attachments by Lefm. *International Journal of Fatigue* 56: 25-32.

Leira, B. J., Næss, A. & Brandrud Næss, O. E. 2016. Reliability Analysis of Corroding Pipelines by Enhanced Monte Carlo Simulation. *International Journal of Pressure Vessels and Piping* 144: 11-17.

Liu, R., Zhang, T., Wu, X. J. & Wang, C. H. 2006. Determination of Stress Intensity Factors for a Cracked Shell under Bending with Improved Shell Theories. *Journal of Aerospace Engineering* 19: 21-28.

Liu, Y. & Mahadevan, S. 2009. Probabilistic Fatigue Life Prediction Using an Equivalent Initial Flaw Size Distribution. *International Journal of Fatigue* 31: 476-487.

Mehrzadi, M. & Taheri, F. 2013. A Material Sensitive Modified Wheeler Model for Predicting the Retardation in Fatigue Response of Am60b Due to an Overload. *International Journal of Fatigue* 55: 220-229.

Ming-Zhou, G., Guo-Ping, C. & Ying, N. 2016. Finite-Time Fault-Tolerant Control for Flutter of Wing. *Control Engineering Practice* 51: 26-47.

Möller, B., Graf, W. & Beer, M. 2003. Safety Assessment of Structures in View of Fuzzy Randomness. *Computers & Structures* 81: 1567-1582.

Mora-López, L. & Mora, J. 2015. An Adaptive Algorithm for Clustering Cumulative Probability Distribution Functions Using the Kolmogorov–Smirnov Two-Sample Test. *Expert Systems with Applications* 42: 4016-4021.

Murakami, Y., Aoki, S., Hasebe, N., Itoh, Y., Miyata, H., Miyazaki, N. & Al., E. 1987. *Stress Intensity Factors Handbook*. Pergamon Press.

Narayanan, G., Rezaei, K. & Nackenhorst, U. 2016. Fatigue Life Estimation of Aero Engine Mount Structure Using Monte Carlo Simulation. *International Journal of Fatigue* 83, Part 1: 53-58.

Nejati, M., Paluszny, A. & Zimmerman, R. W. 2015. On the Use of Quarter-Point Tetrahedral Finite Elements in Linear Elastic Fracture Mechanics. *Engineering Fracture Mechanics* 144: 194-221.

Newman, J. A., Baughman, J. M. & Wallace, T. A. 2010. Investigation of Cracks Found in Helicopter Longerons. *Engineering Failure Analysis* 17: 416-430.

Newman Jr, J. C. & Raju, I. S. 1981. An Empirical Stress Intensity Factor Equation for the Surface Crack. *Engineering Fracture Mechanics* 15: 185-192.

Newman Jr, J. C. & Ramakrishnan, R. 2016. Fatigue and Crack-Growth Analyses of Riveted Lap-Joints in a Retired Aircraft. *International Journal of Fatigue* 82, Part 2: 342-349.

Ohdama, C. 2012. Effect of Kiii on Fatigue Crack Growth Behavior. Master Thesis, Department of Mechanical Engineering, Tokyo University of Science, Japan [in Japanese].

Okada, H., Higashi, M., Kikuchi, M., Fukui, Y. & Kumazawa, N. 2005. Three Dimensional Virtual Crack Closure-Integral Method (Vccm) with Skewed and Non-Symmetric Mesh Arrangement at the Crack Front. *Engineering Fracture Mechanics* 72: 1717-1737.

Olsson, A., Sandberg, G. & Dahlblom, O. 2003. On Latin Hypercube Sampling for Structural Reliability Analysis. *Structural Safety* 25: 47-68.

Pang, J. H. L., Tsang, K. S. & Hoh, H. J. 2016. 3d Stress Intensity Factors for Weld Toe Semi-Elliptical Surface Cracks Using Xfem. *Marine Structures* 48: 1-14.

Patelli, E., Murat Panayirci, H., Broggi, M., Goller, B., Beaurepaire, P., Pradlwarter, H. J. & Schuëller, G. I. 2012. General Purpose Software for Efficient Uncertainty Management of Large Finite Element Models. *Finite Elements in Analysis and Design* 51: 31-48.

Paul, S. K. 2016. Numerical Models of Plastic Zones and Associated Deformations for a Stationary Crack in a C(T) Specimen Loaded at Different R-Ratios. *Theoretical and Applied Fracture Mechanics* (In Press).

Paul, S. K. & Tarafder, S. 2013. Cyclic Plastic Deformation Response at Fatigue Crack Tips. *International Journal of Pressure Vessels and Piping* 101: 81-90.

Pavlou, D. G. 2015. Chapter 1 - an Overview of the Finite Element Method. In. (edit.). *Essentials of the Finite Element Method*, pp. 1-18. Academic Press.

Peng, C., Wu, W. & Zhang, B. 2015. Three-Dimensional Simulations of Tensile Cracks in Geomaterials by Coupling Meshless and Finite Element Method. *International Journal for Numerical and Analytical Methods in Geomechanics* 39: 135-154.

Pook, L. P. 1982. Fracture and Fatigue: Thin Sheet and Micromechanism Problems. Edited By: J.C. Radon. *International Journal of Fatigue* 4: 48.

Pook, L. P. 2000. *Linear Elastic Fracture Mechanics for Engineers: Theory and Application*. Southampton: WIT Press.

Quaranta, G. 2011. Finite Element Analysis with Uncertain Probabilities. *Computer Methods in Applied Mechanics and Engineering* 200: 114-129.

Rajabi, M. M., Ataie-Ashtiani, B. & Janssen, H. 2015. Efficiency Enhancement of Optimized Latin Hypercube Sampling Strategies: Application to Monte Carlo Uncertainty Analysis and Meta-Modeling. *Advances in Water Resources* 76: 127-139.

Ramirez-Marquez, J. E. & Levitin, G. 2008. Algorithm for Estimating Reliability Confidence Bounds of Multi-State Systems. *Reliability Engineering & System Safety* 93: 1231-1243.

Reh, S., Beley, J.-D., Mukherjee, S. & Khor, E. H. 2006. Probabilistic Finite Element Analysis Using Ansys. *Structural Safety* 28: 17-43.

Rhymer, D. W., Johnson, W. S., Singh, R. & Pettit, R. 2008. Stress Intensity Solutions of Thermal Fatigue Induced Cracks in a Thin Plate Hot Spot Using Lefm and Finite Element Analysis. *Engineering Fracture Mechanics* 75: 2826-2841.

Richard, H. A., Fulland, M. & Sander, M. 2005. Theoretical Crack Path Prediction. *Fatigue & Fracture of Engineering Materials & Structures* 28: 3-12.

Rodríguez, J. A., Garcia, J. C., Alonso, E., El Hamzaoui, Y., Rodríguez, J. M. & Urquiza, G. 2015. Failure Probability Estimation of Steam Turbine Blades by Enhanced Monte Carlo Method. *Engineering Failure Analysis* 56: 80-88.

Sain, T. & Chandra Kishen, J. M. 2008. Probabilistic Assessment of Fatigue Crack Growth in Concrete. *International Journal of Fatigue* 30: 2156-2164.

Sallberry, C. J., Helton, J. C. & Hora, S. C. 2007. Extension of Latin Hypercube Samples with Correlated Variables. *Reliability Engineering and System Safety* 93: 1047-1059.

Sanches, R. F., De Jesus, A. M. P., Correia, J. a. F. O., Da Silva, A. L. L. & Fernandes, A. A. 2015. A Probabilistic Fatigue Approach for Riveted Joints Using Monte Carlo Simulation. *Journal of Constructional Steel Research* 110: 149-162.

Sankaran, K. K., Perez, R. & Jata, K. V. 2001. Effects of Pitting Corrosion on the Fatigue Behavior of Aluminum Alloy 7075-T6: Modeling and Experimental Studies. *Materials Science and Engineering: A* 297: 223-229.

Sano, H. 2010. Fatigue Crack Growth Prediction in Consideration of a Plasticity Induced Closure Effect. Master Thesis, Department of Mechanical Engineering, Tokyo University of Science, Japan.

Savaidis, G., Savaidis, A., Zerres, P. & Vormwald, M. 2010. Mode I Fatigue Crack Growth at Notches Considering Crack Closure. *International Journal of Fatigue* 32: 1543-1558.

Schöllman, M., Richard, H. A., Kullmer, G. & Fulland, M. 2002. A New Criterion for the Prediction of Crack Developement in Multiaxially Loaded Structures *International Journal of Fracture* 117: 129-141.

Schuëller, G. I. & Pradlwarter, H. J. 2006. Computational Stochastic Structural Analysis (Cossan) – a Software Tool. *Structural Safety* 28: 68-82.

Shi, K., Cai, L., Chen, L. & Bao, C. 2014. A Theoretical Model of Semi-Elliptic Surface Crack Growth. *Chinese Journal of Aeronautics* 27: 730-734.

Shields, M. D., Teferra, K., Hapij, A. & Daddazio, R. P. 2015. Refined Stratified Sampling for Efficient Monte Carlo Based Uncertainty Quantification. *Reliability Engineering & System Safety* 142: 310-325.

Sih, G. C. 1990. *Mechanics of Fracture Initiation and Propagation*. Dodrecht, Netherlands: Kluwer Academic Publishers.

Śnieżek, L., Ślęzak, T., Grzelak, K. & Hutsaylyuk, V. 2016. An Experimental Investigation of Propagation the Semi-Elliptical Surface Cracks in an Austenitic Steel. *International Journal of Pressure Vessels and Piping*

Song, P. S. & Shieh, Y. L. 2004. Crack Growth and Closure Behaviour of Surface Cracks. *International Journal of Fatigue* 26: 429-436.

Stephens, R. I., Fatemi, A., Stephens, R. R. & Fuchs, H. O. 2001. *Metal Fatigue in Engineering*. 2nd. New York: John Wiley & Sons.

Taylor, D. 2007. Chapter 1 - Introduction: Materials under Stress. In. Taylor, D. (edit.). *The Theory of Critical Distances*, pp. 1-19. Oxford: Elsevier Science Ltd.

Thacker, B. H., Riha, D. S., Fitch, S. H. K., Huyse, L. J. & Pleming, J. B. 2006. Probabilistic Engineering Analysis Using the Nessus Software. *Structural Safety* 28: 83-107.

Thomas, S. B., Mhaiskar, M. J. & Sethuraman, R. 2000. Stress Intensity Factors for Circular Hole and Inclusion Using Finite Element Alternating Method. *Theoretical and Applied Fracture Mechanics* 33: 73-81.

Tian, L., Dong, L., Bhavanam, S., Phan, N. & Atluri, S. N. 2014. Mixed-Mode Fracture &Amp; Non-Planar Fatigue Analyses of Cracked I-Beams, Using a 3d Sgbem–Fem Alternating Method. *Theoretical and Applied Fracture Mechanics* 74: 188-199.

Toribio, J., Matos, J. C., González, B. & Escuadra, J. 2014. Numerical Modelling of Cracking Path in Round Bars Subjected to Cyclic Tension and Bending. *International Journal of Fatigue* 58: 20-27.

Toribio, J., Matos, J. C., González, B. & Escuadra, J. 2015. Evolution of Crack Paths and Compliance in Round Bars under Cyclic Tension and Bending. *Theoretical and Applied Fracture Mechanics*

Tran, V.-X. & Geniaut, S. 2012. Development and Industrial Applications of X-Fem Axisymmetric Model for Fracture Mechanics. *Engineering Fracture Mechanics* 82: 135-157.

Tvedt, L. 2006. Proban – Probabilistic Analysis. *Structural Safety* 28: 150-163.

Underhill, P. R. & Duquesnay, D. L. 2008. The Effect of Dynamic Loading on the Fatigue Scatter Factor for Al 7050. *International Journal of Fatigue* 30: 614-622.

Underhill, P. R. & Duquesnay, D. L. 2009. Effect of Small Cycles and Load Spectrum Truncation on the Fatigue Life Scatter in 7050 Al Alloy. *International Journal of Fatigue* 31: 538-543.

Walz, G. & Riesch-Oppermann, H. 2006. Probabilistic Fracture Mechanics Assessment of Flaws in Turbine Disks Including Quality Assurance Procedures. *Structural Safety* 28: 273-288.

Wang, C. Q., Xiong, J. J., Shenoi, R. A., Liu, M. D. & Liu, J. Z. 2016. A Modified Model to Depict Corrosion Fatigue Crack Growth Behavior for Evaluating Residual Lives of Aluminum Alloys. *International Journal of Fatigue* 83, Part 2: 280-287.

Wang, G. S. 1999. A Probabilistic Damage Accumulation Solution Based on Crack Closure Model. *International Journal of Fatigue* 21: 531-547.

Wang, W., Liang, K., Wang, C. & Wang, Q. 2014. Comparative Analysis of Failure Probability for Ethylene Cracking Furnace Tube Using Monte Carlo and Api Rbi Technology. *Engineering Failure Analysis* 45: 278-282.

Wang, Y.-B. & Sun, Y.-Z. 2005. A New Boundary Integral Equation Method for Cracked 2-D Anisotropic Bodies. *Engineering Fracture Mechanics* 72: 2128-2143.

Wang, Y., Cui, W., Wu, X., Wang, F. & Huang, X. 2008. The Extended Mcevily Model for Fatigue Crack Growth Analysis of Metal Structures. *International Journal of Fatigue* 30: 1851-1860.

Zhang, X., Boscolo, M., Figueroa-Gordon, D., Allegri, G. & Irving, P. E. 2009. Fail-Safe Design of Integral Metallic Aircraft Structures Reinforced by Bonded Crack Retarders. *Engineering Fracture Mechanics* 76: 114-133.

Zhuang, Z., Liu, Z., Cheng, B. & Liao, J. 2014. Chapter 4 - Fundamental Concept and Formula of X-Fem. In. Zhuang, Z., Cheng, Z. L. & Liao, J. (edit.). *Extended Finite Element Method*, pp. 51-73. Oxford: Academic Press.

APPENDIX A

MATRIX FORMULATION

The material property matrix $[D]$ is expressed as

$$[D] = \frac{E}{(1+\nu)(1-2\nu)} \begin{bmatrix} 1-\nu & \nu & \nu & 0 & 0 & 0 \\ \nu & 1-\nu & \nu & 0 & 0 & 0 \\ \nu & \nu & 1-\nu & 0 & 0 & 0 \\ 0 & 0 & 0 & \frac{1-2\nu}{2} & 0 & 0 \\ 0 & 0 & 0 & 0 & \frac{1-2\nu}{2} & 0 \\ 0 & 0 & 0 & 0 & 0 & \frac{1-2\nu}{2} \end{bmatrix} \tag{0.1}$$

The shape function, $[N]$ is given by

$$[N] = \begin{bmatrix} N_1 & 0 & 0 & N_2 & 0 & 0 & \cdots & N_{20} & 0 & 0 \\ 0 & N_1 & 0 & 0 & N_2 & 0 & \cdots & 0 & N_{20} & 0 \\ 0 & 0 & N_1 & 0 & 0 & N_2 & \cdots & 0 & 0 & N_{20} \end{bmatrix} \tag{0.2}$$

where

$$N_1 = (\frac{1}{8})(1-\xi)(1-\eta)(1-\zeta)(-\xi-\eta-\zeta-2)$$
$$N_2 = (\frac{1}{8})(1+\xi)(1-\eta)(1-\zeta)(-\xi-\eta-\zeta-2)$$
$$N_3 = (\frac{1}{8})(1+\xi)(1+\eta)(1-\zeta)(-\xi-\eta-\zeta-2)$$
$$N_4 = (\frac{1}{8})(1-\xi)(1+\eta)(1-\zeta)(-\xi+\eta-\zeta-2)$$
$$N_5 = (\frac{1}{8})(1-\xi)(1-\eta)(1+\zeta)(-\xi-\eta+\zeta-2)$$
$$N_6 = (\frac{1}{8})(1+\xi)(1-\eta)(1+\zeta)(-\xi+\eta-\zeta-2)$$
$$N_7 = (\frac{1}{8})(1+\xi)(1+\eta)(1+\zeta)(+\xi+\eta-\zeta-2)$$

$$N_8 = (\frac{1}{8})(1-\xi)(1+\eta)(1+\zeta)(-\xi+\eta+\zeta-2)$$
$$N_9 = (\frac{1}{4})(1-\xi^2)(1-\eta)(1-\zeta)$$
$$N_{10} = (\frac{1}{4})(1+\xi)(1-\eta^2)(1-\zeta)$$
$$N_{11} = (\frac{1}{4})(1-\xi^2)(1+\eta)(1-\zeta)$$
$$N_{12} = (\frac{1}{4})(1-\xi)(1-\eta^2)(1-\zeta)$$
$$N_{13} = (\frac{1}{4})(1-\xi)(1-\eta)(1-\zeta^2)$$
$$N_{14} = (\frac{1}{4})(1-\xi^2)(1-\eta)(1+\zeta)$$
$$N_{15} = (\frac{1}{4})(1-\xi^2)(1+\eta^2)(1+\zeta)$$
$$N_{16} = (\frac{1}{4})(1-\xi^2)(1+\eta)(1-\zeta)$$
$$N_{17} = (\frac{1}{4})(1-\xi^2)(1-\eta)(1+\zeta)$$
$$N_{18} = (\frac{1}{4})(1+\xi)(1-\eta^2)(1+\zeta)$$
$$N_{19} = (\frac{1}{4})(1-\xi^2)(1+\eta)(1+\zeta)$$
$$N_{20} = (\frac{1}{4})(1-\xi)(1-\eta^2)(1+\zeta)$$

The $[B]$ matrix can be presented as

$$[B] = \begin{bmatrix} \frac{\delta}{\delta x} & 0 & 0 \\ 0 & \frac{\delta}{\delta y} & 0 \\ 0 & 0 & \frac{\delta}{\delta z} \\ \frac{\delta}{\delta y} & \frac{\delta}{\delta x} & 0 \\ 0 & \frac{\delta}{\delta z} & \frac{\delta}{\delta y} \\ \frac{\delta}{\delta z} & 0 & \frac{\delta}{\delta x} \end{bmatrix} [N] \tag{0.3}$$

The expended of Eq. (3.16) can be expressed as

$$\{\varepsilon\} = \begin{bmatrix} \frac{\delta N_1}{\delta x} & 0 & 0 & \frac{\delta N_2}{\delta x} & 0 & 0 & \cdots & \frac{\delta N_{20}}{\delta x} & 0 & 0 \\ 0 & \frac{\delta N_1}{\delta y} & 0 & 0 & \frac{\delta N_2}{\delta y} & 0 & \cdots & 0 & \frac{\delta N_{20}}{\delta y} & 0 \\ 0 & 0 & \frac{\delta N_1}{\delta z} & 0 & 0 & \frac{\delta N_2}{\delta z} & \cdots & 0 & 0 & \frac{\delta N_{20}}{\delta z} \\ \frac{\delta N_1}{\delta y} & \frac{\delta N_1}{\delta x} & 0 & \frac{\delta N_2}{\delta y} & \frac{\delta N_2}{\delta x} & 0 & \cdots & \frac{\delta N_{20}}{\delta y} & \frac{\delta N_{20}}{\delta x} & 0 \\ 0 & \frac{\delta N_1}{\delta z} & \frac{\delta N_1}{\delta y} & 0 & \frac{\delta N_2}{\delta z} & \frac{\delta N_2}{\delta y} & \cdots & 0 & \frac{\delta N_{20}}{\delta z} & \frac{\delta N_{20}}{\delta y} \\ \frac{\delta N_1}{\delta z} & 0 & \frac{\delta N_1}{\delta x} & \frac{\delta N_2}{\delta z} & 0 & \frac{\delta N_2}{\delta x} & \cdots & \frac{\delta N_{20}}{\delta z} & 0 & \frac{\delta N_{20}}{\delta x} \end{bmatrix} \begin{Bmatrix} u_1 \\ v_1 \\ w_1 \\ u_2 \\ v_2 \\ w_2 \\ \vdots \\ u_{20} \\ v_{20} \\ w_{20} \end{Bmatrix} \quad (0.4)$$

APPENDIX B

VOID OF ProbS-FEM

```
#include<stdio.h>
#include<stdlib.h>
#include<malloc.h>
#include<math.h>
#include<time.h>
#include<unistd.h>

#define  DIM               3
#define  NUMNODEELEM       20
#define  SzINT   sizeof(int)
#define  SzDBL   sizeof(double)

typedef  int     INT;
typedef  double  DBL;
typedef  INT **  IMatrix_t;
typedef  INT *   IVector_t;
typedef  DBL *   DVector_t;

typedef  struct {
  INT  numNode;
  INT  numElem;
  INT  dummy1;
  INT  dummy2;
}  Size_t;

typedef  struct {
  DVector_t  coord;
}  Node;
typedef  Node *  Node_t;

typedef  struct {
  IVector_t  node;
  int *kkm;
  int *nflag;
}  Elem;
typedef  Elem *  Elem_t;

typedef  struct {
  INT  numBC;
  IVector_t node;
} Bc;
typedef Bc * Bc_t;

typedef  struct {
  Size_t   size;
  Node_t   node;
  Elem_t   elem;
  IVector_t bc_node;
  INT       numBC;
  Bc_t     bc;
  INT      numLayer;
  IMatrix_t vccm;
}  FEM;
typedef FEM * FEM_t;


int  main( int argc, char *argv[])
{
  if( argc !=5 ){                       //edit by akramin
```

```
    printf("Usage: $numStep $probsample $numLayer $numLocal \n",argv[0] );
    exit(1);
  }

/*  FILE *write_port_E = fopen ("portion-strat-E.dat","a");
  FILE *read_port_E  = fopen ("portion-strat-E.dat","r");

  FILE *read_portstrat_Pc    = fopen ("portion-strat-Pc.dat","r");
  FILE *write_port_Pc        = fopen ("portion-strat-Pc.dat","a");
*/

  int step       = atoi(argv[1]);
  int probsample    = atoi(argv[2]);
  int numlayer      = atoi(argv[3]);
  int numlocal      = atoi(argv[4]);

  char character,fileName[256];
  int sample,local1,local2;
  float cycle[probsample+1][step+1][numlocal+1],
xo[numlocal+1][probsample+1][step+1][numlayer+1],
yo[numlocal+1][probsample+1][step+1][numlayer+1],
zo[numlocal+1][probsample+1][step+1][numlayer+1],
xn[numlocal+1][probsample+1][step+1][numlayer+1],
yn[numlocal+1][probsample+1][step+1][numlayer+1],
zn[numlocal+1][probsample+1][step+1][numlayer+1],
cycletotal[probsample+1][step+1][numlocal+1];

  FILE *read_PC    = fopen ("Prob_cycle.dat","r");

  for (int i=0;i<=15;i++){
     fscanf( read_PC,"%c \n",&character);//Di susun dari local
  }

  fscanf( read_PC,"%d \n",&local1);//1

  for (int i=0;i<=12;i++){
     fscanf( read_PC,"%c \n",&character);//sehingga local
  }

  fscanf( read_PC,"%d \n",&local2);//end of local num
  for (int j=0;j<=probsample;j++){
       for (int i=0;i<=5;i++){
         fscanf( read_PC,"%c \n",&character);//sample
       }
       fscanf( read_PC,"%d \n",&sample);//0
       for (int i=0;i<=step;i++){
           for (int m=0;m<numlocal;m++){
               fscanf( read_PC,"%e
\n",&cycle[j][i][m]);//cycle[probsample][step]
               cycletotal[j][i][m]=cycletotal[j][i-1][m]+cycle[j][i][m];
           }
       }

       for (int m=0;m<=numlocal;m++){
           cycletotal[j+1][0-1][m]=0.0;
       }
  }


/**************Read pS**,local1.crack***************/
  for (int l=0;l<numlocal;l++){
       for (int j=0;j<=probsample;j++){
           sprintf(fileName, "pS%d,local%d.crack",j,l+1);
           FILE *read_pS0    = fopen (fileName,"r");

           for (int k=0;k<=step;k++){
               for (int i=0;i<=5;i++){
```

```
                    fscanf( read_pS0,"%c \n",&character);//sample
                }

                fscanf( read_pS0,"%d \n",&sample);//0
                for (int i=0;i<=3;i++){
                    fscanf( read_pS0,"%c \n",&character);//step
                }

                fscanf( read_pS0,"%d \n",&sample);//0
                for (int i=0;i<=4;i++){
                    fscanf( read_pS0,"%c \n",&character);//Local
                }

                fscanf( read_pS0,"%d \n",&sample);//0
                for (int i=0;i<=62;i++){
                    fscanf( read_pS0,"%c \n",&character);
                }

                for (int i=0;i<=numlayer;i++){
                    fscanf( read_pS0,"%e %e %e %e %e
%e",&xo[l][j][k][i],&yo[l][j][k][i],&zo[l][j][k][i],&xn[l][j][k][i],&yn[l][j]
[k][i],&zn[l][j][k][i]); //coord old x y z new x y z
                }
                fscanf( read_pS0,"%c \n",&character);//sample
            }//end for all steps
        }//end for allprobsample
    } //end for all numlocal


/**************write_avsn***************/
    for (int m=0;m<numlocal;m++){
        sprintf(fileName, "Prob_avsn_l%d.dat",m+1);
        FILE *write_avsn = fopen (fileName,"a");

        sprintf(fileName, "Prob_allpS_l%d.dat",m+1);
        FILE *write_pS0 = fopen (fileName,"a");

        for (int j=0;j<=probsample;j++){
/**************open this for none EIFS***************/
//          fprintf(write_avsn,"0.000000e+00 0.000000e+00 0.000000e+00
0.000000e+00 ");
/**************open this for EIFS***************/
              fprintf(write_avsn,"0.000000e+00 %e %e %e ",
fabs(xo[m][j][0][0]), fabs(yo[m][j][0][10]), fabs(xo[m][j][0][20]));

        }
        fprintf(write_avsn,"\n");

        for (int k=0;k<=step;k++){
            for (int j=0;j<=probsample;j++){
/**************open this for none EIFS***************/
//              fprintf(write_avsn,"%e %e %e %e ",cycletotal[j][k][m],
fabs(xo[m][j][k+1][0]-xo[m][j][0][0]), fabs(yo[m][j][k+1][10]-
yo[m][j][0][10]), fabs(xo[m][j][k+1][20]-xo[m][j][0][20]));
/**************open this for EIFS***************/
              fprintf(write_avsn,"%e %e %e %e ",cycletotal[j][k][m],
fabs(xo[m][j][k+1][0]), fabs(yo[m][j][k+1][10]), fabs(xo[m][j][k+1][20]));
//            printf("%e %e %e %e %e %e %e\n",cycle[j][k][m],
xo[m][j][k+1][0],xo[m][j][0][0], yo[m][j][k+1][10],yo[m][j][0][10],
xo[m][j][k+1][20],xo[m][j][0][20]);
            }
            fprintf(write_avsn,"\n");
        }

/**************write_Prob_allpS_l1.dat***************/
        for (int k=0;k<=step;k++){
            for (int j=0;j<=probsample;j++){
```

```
            fprintf(write_pS0,"Sampel %d Step %d Local0 - -
",j,k);
        }
        fprintf(write_pS0,"\n");
        fprintf(write_pS0,"Oldcracktip[DIM], Newcracktip[DIM] (About Node
(calculate by spline))\n");
        fprintf(write_pS0,"\n");
        for (int i=0;i<=numlayer;i++){
            for (int j=0;j<=probsample;j++){
                fprintf(write_pS0," %e  %e  %e  %e  %e  %e - ",
xo[m][j][k][i], yo[m][j][k][i], zo[m][j][k][i], xn[m][j][k][i],
yn[m][j][k][i], zn[m][j][k][i]);
//               printf(" %e  %e  %e  %e  %e - \n", xo[j][k][i],
yo[j][k][i], zo[j][k][i], xn[j][k][i], yn[j][k][i], zn[j][k][i]);
//              printf("cycle %e j%d k%d cycletotal
%e\n",cycle[j][k],j,k,cycletotal[j][k]);
            }
            fprintf(write_pS0,"\n");
        }
        fprintf(write_pS0,"\n\n");
    }
  }//end for all numlocal

/**************read_pre_all.vccm1/2***************/
  char char1, char2, char3, char4;
  float KI[numlocal+1][probsample+1][step+1][numlayer+1],
KII[numlocal+1][probsample+1][step+1][numlayer+1],
KIII[numlocal+1][probsample+1][step+1][numlayer+1];
  int layer[numlocal+1][probsample+1][step+1][numlayer+1],dummy;

  for (int m=0;m<numlocal;m++){
      sprintf(fileName, "pre_all.vccm%d",m+1);
      FILE *read_pre_all_vccm = fopen (fileName,"r");

      for (int j=0;j<=probsample;j++){
           for (int k=0;k<=step;k++){
               for (int i=0;i<=6;i++){
                   fscanf( read_pre_all_vccm,"%c \n",&character);//sample
               }

               fscanf( read_pre_all_vccm,"%d \n",&dummy);//0

               for (int i=0;i<=3;i++){
                   fscanf( read_pre_all_vccm,"%c \n",&character);//step
               }

               fscanf( read_pre_all_vccm,"%d \n",&dummy);//0

               for (int l=0;l<=43;l++){
                   fscanf(read_pre_all_vccm,"%c", &character);//Layer KI KII
KIII
               }

               for (int i=0;i<numlayer;i++){
                   fscanf(read_pre_all_vccm,"%d %e %e %e",
&layer[m][j][k][i], &KI[m][j][k][i], &KII[m][j][k][i], &KIII[m][j][k][i]);
               }
           }
      }
  }


/**************write_Pre_all.vccm1/2***************/
  float KI_total=0.0, KII_total=0.0, KIII_total=0.0;

  for (int m=0;m<numlocal;m++){
```

```
        sprintf(fileName, "Pre_all_L%d.vccm",m+1);
        FILE *write_pre_all_vccm = fopen (fileName,"a");
        fprintf(write_pre_all_vccm,"KI \n");

        for (int k=0;k<=step;k++){
            for (int i=0;i<=numlayer;i++){
             fprintf(write_pre_all_vccm,"%d ",i);
                for (int j=0;j<=probsample;j++){
                    fprintf(write_pre_all_vccm,"%e ", KI[m][j][k][i]);
                    KI_total=KI_total+KI[m][j][k][i];
                 }
             fprintf(write_pre_all_vccm," %e\n",KI_total/(probsample+1));
             KI_total=0.0;
             }
        fprintf(write_pre_all_vccm,"step %d\n",k);
        }

        fprintf(write_pre_all_vccm,"KII \n");
        for (int k=0;k<=step;k++){
            for (int i=0;i<=numlayer;i++){
             fprintf(write_pre_all_vccm,"%d ",i);
                for (int j=0;j<=probsample;j++){
                    fprintf(write_pre_all_vccm,"%e ", KII[m][j][k][i]);
                    KII_total=KII_total+KII[m][j][k][i];
                 }
             fprintf(write_pre_all_vccm," %e\n",KII_total/(probsample+1));
             KII_total=0.0;
             }
        fprintf(write_pre_all_vccm,"step %d\n",k);
        }

        fprintf(write_pre_all_vccm,"KIII \n");
        for (int k=0;k<=step;k++){
            for (int i=0;i<=numlayer;i++){
             fprintf(write_pre_all_vccm,"%d ",i);
                for (int j=0;j<=probsample;j++){
                    fprintf(write_pre_all_vccm,"%e ", KIII[m][j][k][i]);
                    KIII_total=KIII_total+KIII[m][j][k][i];
                 }
             fprintf(write_pre_all_vccm," %e\n",KIII_total/(probsample+1));
             KIII_total=0.0;
             }
        fprintf(write_pre_all_vccm,"step %d\n",k);
        }
    }

    printf("completed rewrite_result..\n");

    return 0;
}
```

APPENDIX C

LIST OF PUBLICATIONS

Published Journal Papers with Ranking

1. **Akramin, M. R. M.**, Ariffin, A. K., Kikuchi, M., Abdullah, S., Beer, M. & Nikabdullah, N. 2016. Surface Crack Growth and Stress Intensity Factor under Cyclic Load Using S-version Finite Element Method and Embedded Latin Hypercube Sampling. *Journal of Zhejiang University: Science A* (In Press). (Journal Ranking: Q2)

2. **Akramin, M. R. M.**, Shaari, M. S., Ariffin, A. K., Kikuchi, M. & Abdullah, S. 2015. Surface Crack Analysis under Cyclic Loads Using Probabilistic S-Version Finite Element Model. *Journal of the Brazilian Society of Mechanical Sciences and Engineering* 37(6): (1851-1865). (Journal Ranking: Q4)

3. **Akramin, M. R. M.**, Ariffin, A. K., Kikuchi, M. & Abdullah, S. 2016. Sampling method in probabilistic S-version finite element analysis for initial flaw size. *Journal of the Brazilian Society of Mechanical Sciences and Engineering* (1-9). (Journal Ranking: Q4)

Published Journal Papers without Ranking

1. **Akramin, M. R. M**., Ariffin, A. K., Kikuchi, M., Abdullah, S. & Nikabdullah, N. 2014. Fatigue Crack Growth Analysis of Semielliptical Surface Crack. *Applied Mechanics and Materials* 471(293-298).

2. Zulkifli, A., Ariffin, A. K. & **Akramin, M. R. M**. 2014. Probabilistic Model of Surface Crack on the Lumbar Vertebra. *Applied Mechanics and Materials* 471(299-305).

Presented Papers in International and National Conference

1. **Akramin, M. R. M**., Ariffin, A. K., Kikuchi, M., Abdullah, S. & Shaari, M. S. 2015. Probabilistic Life Assessment of Semi-Elliptical Surface-Cracks under Cyclic Tension and Bending. *9th International Conference on Numerical Analysis in Engineering. Batam, Kepulauan Riau-Indonesia*, 27th - 29th August 2015.

2. **Akramin, M. R. M**., Ariffin, A. K., Kikuchi, M., Abdullah, S. & Nikabdullah, N. 2013. Coupled Reliability and S-Version Finite-Element Model for Probabilistic Distribution of Surface Crack Growth under Constant Amplitude Loading. *5th Asia Pacific Congress On Computational Mechanics & 4th International Symposium On Computational Mechanics, Singapore*.

3. **Akramin, M. R. M**., Ariffin, A. K., Kikuchi, M., Abdullah, S. & Nikabdullah, N. 2013. Probabilistic Distribution of Surface Crack Growth Analysis with Uncertain Parameters. *8th International Conference on Numerical Analysis in Engineering. Pekanbaru, Riau, Indonesia*, 13 - 14 May 2013.

4. **Akramin, M. R. M**., Ariffin, A. K., Kikuchi, M., Abdullah, S., Nikabdullah, N. & Shaari, M. 2012. Probabilistic Analysis Based on S-Version Finite Element Method of Surface Crack Growth. *10th International Probabilistic Workshop, Germany.*

5. **Akramin, M. R. M**., Ariffin, A. K., Kikuchi, M., Abdullah, S. & Nikabdullah, N. 2012. Fatigue Crack Growth Analysis of Semielliptical Surface Crack. *4th International Conference on Noise, Vibration and Comfort (NVC). Kuala Lumpur, Malaysia,* 26-29 November 2012.

Award

1. **Best Paper Award: Akramin, M. R. M**., Ariffin, A. K., Kikuchi, M., Abdullah, S. & Shaari, M. S. 2015. Probabilistic Life Assessment of Semi-Eliptical Surface-Cracks under Cyclic Tension and Bending. *9th International Conference on*

Numerical Analysis in Engineering. Batam, Kepulauan Riau-Indonesia, 27th - 29th August 2015.